AD-A157 239 BASIC EMC (ELECTROMAGNETIC COMPATIBILITY) TECHNOLOGY ADVANCEMENT FOR C3 (.. (U) SOUTHEASTERN CENTER FOR ELECTRICAL ENGINEERING EDUCATION INC S.. 1/2

UNCLASSIFIED D WEINER ET AL. APR 85 RADC-TR-82-286-VOL-6 F/G 17/2 NL

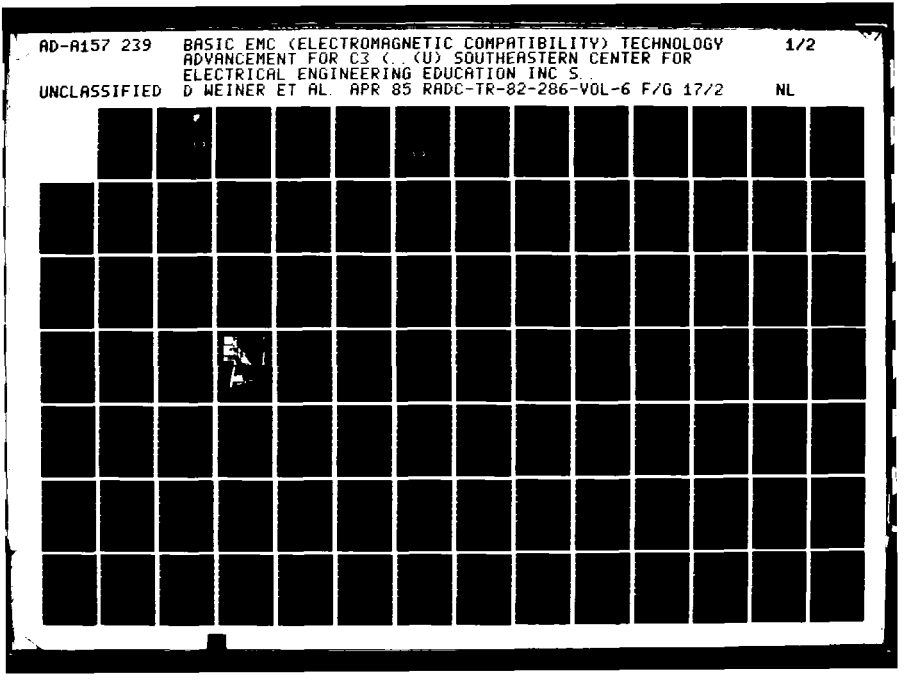

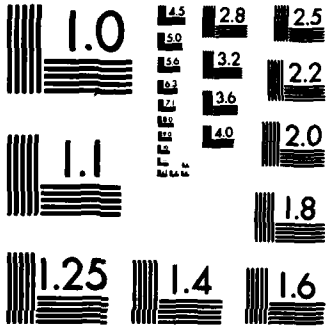

(2)

RADC-TR-82-286, Vol VI (of six)
Final Technical Report
April 1985

BASIC EMC TECHNOLOGY ADVANCEMENT FOR C^3 SYSTEMS

Southeastern Center for Electrical Engineering Education

Donald Weiner, Clayton Paul and James Whalen

APPROVED FOR PUBLIC RELEASE; DISTRIBUTION UNLIMITED

ROME AIR DEVELOPMENT CENTER
Air Force Systems Command
Griffiss Air Force Base, NY 13441-5700

This report has been reviewed by the RADC Public Affairs Office (PA) and is releasable to the National Technical Information Service (NTIS). At NTIS it will be releasable to the general public, including foreign nations.

RADC-TR-82-286, Volume VI (of six) has been reviewed and is approved for publication.

APPROVED: Roy F. Stratton

ROY F. STRATTON
Project Engineer

APPROVED: John J. Bart

JOHN J. BART
Acting Technical Director
Reliability & Compatibility Division

FOR THE COMMANDER: John A. Ritz

JOHN A. RITZ
Acting Chief, Plans Office

If your address has changed or if you wish to be removed from the RADC mailing list, or if the addressee is no longer employed by your organization, please notify RADC (RBCT) Griffiss AFB NY 13441-5700. This will assist us in maintaining a current mailing list.

Do not return copies of this report unless contractual obligations or notices on a specific document requires that it be returned.

UNCLASSIFIED
SECURITY CLASSIFICATION OF THIS PAGE

REPORT DOCUMENTATION PAGE

1a. REPORT SECURITY CLASSIFICATION UNCLASSIFIED	1b. RESTRICTIVE MARKINGS N/A
2a. SECURITY CLASSIFICATION AUTHORITY N/A	3. DISTRIBUTION/AVAILABILITY OF REPORT Approved for public release; distribution unlimited.
2b. DECLASSIFICATION/DOWNGRADING SCHEDULE N/A	
4. PERFORMING ORGANIZATION REPORT NUMBER(S) N/A	5. MONITORING ORGANIZATION REPORT NUMBER(S) RADC-TR-82-286, Vol VI (of six)
6a. NAME OF PERFORMING ORGANIZATION Southeastern Center for Electrical Engineering Education 6b. OFFICE SYMBOL (If applicable)	7a. NAME OF MONITORING ORGANIZATION Rome Air Development Center (RBCT)
6c. ADDRESS (City, State and ZIP Code) 1101 Massachusetts Ave. St. Cloud FL 32706	7b. ADDRESS (City, State and ZIP Code) Griffiss AFB NY 13441-5700
8a. NAME OF FUNDING/SPONSORING ORGANIZATION Rome Air Development Center 8b. OFFICE SYMBOL (If applicable) RBCT	9. PROCUREMENT INSTRUMENT IDENTIFICATION NUMBER F30602-81-C-0062
8c. ADDRESS (City, State and ZIP Code) Griffiss AFB NY 13441-5700	10. SOURCE OF FUNDING NOS. PROGRAM ELEMENT NO. 62702F; PROJECT NO. 2338; TASK NO. 03; WORK UNIT NO. 35

11. TITLE (Include Security Classification)
BASIC EMC TECHNOLOGY ADVANCEMENT FOR C^3 SYSTEMS

12. PERSONAL AUTHOR(S)
Donald Weiner, Clayton R. Paul, James Whalen

13a. TYPE OF REPORT	13b. TIME COVERED	14. DATE OF REPORT (Yr., Mo., Day)	15. PAGE COUNT
Final	FROM Jun 82 TO Dec 83	April 1985	142

16. SUPPLEMENTARY NOTATION
Work was performed at Syracuse University, University of Kentucky, State University of New York, and University of South Florida. Project Engineers: Gerard Capraro, (Cont'd)

17. COSATI CODES		
FIELD	GROUP	SUB. GR.
09	03	

18. SUBJECT TERMS (Continue on reverse if necessary and identify by block number)
Electromagnetic Effects; Electromagnetic Interface; Microelectronic Circuits; Electromagnetic Coupling and testing; Crosstalk (Cont'd)

19. ABSTRACT (Continue on reverse if necessary and identify by block number)

This research effort was devoted to eliminating some of the basic technological gaps in the two important areas of 1) electromagnetic effects (EM) on microelectronic circuits and 2) EM coupling and testing. The results are presented in fourteen reports which have been organized into six volumes. The reports are briefly summarized in this volume.

In addition, an experiment is described which was performed to demonstrate the feasibility of applying several of the results to a problem involving electromagnetic interference. Specifically, experimental results are provided for the randomness associated with 1) crosstalk in cable harnesses and 2) demodulation of amplitude modulated (AM) signals in operational amplifiers. These results are combined to predict candidate probability density functions (pdf's) for the amplitude of an AM interfering signal required to turn on a light emitting diode. The candidate pdf's are shown to be statistically consistent with measured data.

20. DISTRIBUTION/AVAILABILITY OF ABSTRACT	21. ABSTRACT SECURITY CLASSIFICATION
UNCLASSIFIED/UNLIMITED ☒ SAME AS RPT. ☐ DTIC USERS ☐	UNCLASSIFIED

22a. NAME OF RESPONSIBLE INDIVIDUAL	22b. TELEPHONE NUMBER (Include Area Code)	22c. OFFICE SYMBOL
ROY F. STRATTON	(315) 330-2563	RADC (RBCT)

DD FORM 1473, 83 APR EDITION OF 1 JAN 73 IS OBSOLETE.

UNCLASSIFIED
SECURITY CLASSIFICATION OF THIS PAGE

Block 16 (Cont'd)

Roy F. Stratton

Block 18 (Cont'd)

Cable Harnesses
Probabilistic Approach
Nonlinear Behavior
Operational Amplifiers

TABLE OF CONTENTS

LIST OF FIGURES

LIST OF FIGURES (continued)

LIST OF FIGURES (continued)

I. Introduction

The work performed in this effort is directed towards the design, analysis, and prediction of electromagnetic compatibility (EMC) in command, control, and communications (C^3) systems. This was accomplished by closing some basic technological gaps in two important areas. The first area dealt with electromagnetic (EM) effects on microelectronic circuits while the second was concerned with EM coupling and testing.

To obtain insight into the response of microelectronic circuits to electromagnetic interference (EMI), EMI effects were studied in several types of operational amplifiers and in a differential line receiver. Laboratory measurements were performed on the operational amplifiers whereas a computer simulation was made of the differential line receiver.

Attention was also devoted to the problem of analyzing and predicting EMI in microelectronic circuits. It was shown that the task of modeling complicated digital circuits for EMI effects can be greatly simplified through the use of macromodels. In particular, macromodels were developed for operational amplifiers, a NAND gate, and a four bit comparator. In addition, the probabilistic approach to EMI was investigated. This included an experimental study of the statistical variations of EMI in operational amplifiers, a probabilistic analysis of EMI induced propagation delays in combinational digital circuits, and the analysis of EMI in an experimental system containing both a random coupling mechanism and a random second-order rectification effect.

To eliminate gaps in the area of EM coupling and testing, studies were carried out in 1) coupling of EM fields into transmission lines,

2) crosstalk between shielded cables, 3) crosstalk in twisted wire circuits, 4) crosstalk in balanced twisted pairs, and 5) modeling of transmission lines. Finally, recommendations were made for revisions to the wire-to-wire coupling subroutine in IEMCAP.

Results of these efforts are reported in six volumes whose contents are briefly summarized below.

Volume IA: "Nonlinear Macromodel of the Bipolar Integrated Circuit Operational Amplifier for Electromagnetic Interference Analysis" by Gordon Chen and Dr. James Whalen [1].

This report describes a small-signal nonlinear macromodel for the bipolar IC Op Amp which can be used successfully for RFI analysis. Two BJT's are adequate to characterize the complete IC. The effectiveness of the small-signal nonlinear macromodel is verified by the agreement between the NCAP computer program predictions and experimental results for the second order transfer function of the 741 Op Amp unity gain buffer amplifier. Good agreement is also obtained between NCAP calculations based on the macromodel and the full model. By using the Op Amp macromodel, a saving of nearly an order of magnitude in computer costs is achieved. Not only does the macromodel conserve computer resources, it makes it possible for the EMC engineer to analyze electronic systems involving many Op Amps.

Another important aspect of the small-signal nonlinear macromodel is that it is a global model which can be used for all Op Amp types.

The two macromodel transistors should be the same type as those at the input of the IC Op Amp being modeled. The need for laboratory characterization of the individual transistors in each new bipolar Op Amp appear not to be required. A combination of manufacturer's specifications and previous IC BJT results can be used. This was demonstrated by the successful application of the nonlinear macromodel to the new LM10 IC Op Amp for RFI analysis by NCAP, without resorting to full model analysis, nor experimental device characterization.

However, the accuracy of the nonlinear macromodel relies on the inclusion of capacitors to represent the effects of substrate parasitic capacitances. The proper selection of substrate capacitors does not necessarily follow the structural IC parasitic capacitances. The effects caused by these capacitances are simulated by four capacitors in the macromodel. The best values for these capacitors were found by comparing NCAP predicted values with experimental values for a second order transfer function of the Op Amp in an unity gain buffer amplifier. Thus a parametric fitting is involved when a new Op Amp is modeled.

That the combined nonlinearities of tens of BJTs in a linear IC Op Amp can be represented quite well by a pair of BJTs in a macromodel is explained by the cascading theory of nonlinear transfer functions. The essential point appears to be that the second stage (gain-stage) contribution to the Op Amp second order transfer function is reduced greatly by the internal feedback capacitor of the second stage. Also it was argued that the input stage which consists of two cascode stages

in a differential pair arrangement can be represented by two common emitter stages in a differential pair configuration used in the Op Amp macromodel. The validity of the nonlinear macromodel is therefore supported both by experimental verification and by network theory.

Volume IB: "Radio Frequency Interference Demodulation Effects in Operational Amplifier Circuits" by Yue-Hong Sutu and Dr. James Whalen [2].

Since monolithic integrated operational amplifiers (op amps) are important building blocks in today's control and communication systems, a series of investigations are carried out to determine RFI effects in analog circuits using op amps as active devices. The specific RFI effect investigated is how amplitude-modulated (AM) RF signals are demodulated in op amp circuits to produce undesired low frequency responses at the AM-modulation frequency. Subsequently, the undesired demodulation responses may be processed in a manner similar to a desired low frequency signal by the low frequency components that follow the op amp. The undesired demodulation responses are shown to be characterized by second-order nonlinear transfer functions.

Four representative op amp types investigated are the 741 bipolar op amp with its conventional npn input transistors, the LM10 bipolar op amp with its less conventional pnp input transistors, the LF355 JFET-Bipolar op amp with its JFET input transistors, and the CA081 MOS-Bipolar op amp with its MOSFET input transistors.

Two op amp circuits are investigated. The first op amp circuit configuration is the unity voltage gain buffer circuit known as a voltage follower. The circuit configuration is also called noninverting because both the intended signal and the RFI signal are injected into the noninverting input. The second circuit is an inverting op amp configuration. The intended signal voltage gain is determined by the ratio of the feedback resistor R2 and the input resistor R1. The investigation includes several combinations of R1 and R2 and also the effects of an RFI suppression capacitor in the feedback path.

Approximately 30 units of each op amp type are tested to determine the statistical variations of RFI demodulation effects in the two op amp circuits. Statistical parameters such as means and standard deviations provide quantitative measures on variations in op amp RFI susceptibility.

The Nonlinear Circuit Analysis Program NCAP is used to simulate the demodulation RFI response. In the circuit simulation, the op amp is replaced by its incremental macromodel. Values of macromodel parameters are obtained from previous investigations and from manufacturer's data sheets. Sensitivity analysis of the effects of variations of model parameters upon RFI susceptibility is performed for the unity gain buffer circuit in which critical parameters were identified. The effects of the RFI suppression capacitor in the inverting op amp circuit is also simulated. The simulated results are compared to measurements and satisfactory agreement is achieved.

Volume IIA: "Macromodels of Op Amps for CADA Applications" by Dr. James Bowers [3].

Due to the large number of active elements in IC operational amplfiers, a device-level computer simulation would be quite expensive and time consuming. Simulation of circuits containing several op amps would not be a reasonable endeavor using a model of this order of complexity.

A macromodel is therefore desired which, while accurately predicting the performance of the op amp under all circuit conditions, will have a minimum level of complexity, so that larger circuits containing several op amps may be efficiently simulated in reasonable amounts of computer time.

This model should contain all of these common op amp characteristics:

1. Input impedance, bias current, offset current and voltage.
2. Output impedance (DC and AC), voltage and current limiting.
3. Differential and common mode gain and rolloff versus frequency.
4. Non-symmetrical slew rate and step response feedthrough.

The model should be applicable to both standard bipolar input op amps as well as devices employing field effect transistors in their input stages, and should accept external compensation if required.

In this report, a model is developed by simplifying a previously suggested slewing model to a two-diode equivalent circuit. This circuit is then modified to include the desired input, output, and differential features. The device parameters (frequency response, etc.) is derived

for this general model, then the model parameters are solved for in terms of the device parameters. Finally, models are developed for four real op amps and extensively tested.

Volume II B: "Macromodeling of Digital Circuits," by Ronald Vogelsong and Dr. James Bowers [4].

A NAND gate macro-model is developed using SPICE which allows for the complete simulation of the operation of the logic gate. The model derivation requires only external DC voltage and current measurements and logic delay times, but the model developed is shown to fully simulate the high-frequency response of the device as well, including the response of the device to interference in the 1-100MHz range.

In addition to the fully-qualified model developed for SPICE, a simpler model is constructed for use in the SUPER*SCEPTRE simulation program which effectively models the device from DC up to normal switching speed limits.

Finally, a look is taken at developing a SPICE model of a device constructed from a large number of logic elements fabricated on a single chip, a TTL 5485 four bit comparator. In this case, the overall complexity is such that a modeling procedure is developed based on minimizing the complexity and hence computer (CPU) time of the circuit while still maintaining the logical, input, output, and propagation delay characteristics.

Volume III A: "Probabilistic Analysis of Combinational Circuits with Random Delays" by Abner Ephrath and Dr. Donald Weiner [5].

Random propagation delays are encountered in digital integrated circuits due to fluctuations in the fabrication process. These delays can be further increased due to the presence of electromagnetic interference. System performance can be evaluated from the expected values of the output signals. Analytical methods for determining the output expected values of combinational circuits with random delays are developed in this report.

Given the input expectations, the network logic functions, and p.d.f.'s of the delays associated with the gates in the network, it is shown how to obtain the output expected values. Two types of delay elements are considered: 1) the pure delay element, whose output is a delayed, but undistorted, replica of the input and 2) the discriminating delay element, where input rise and fall transitions experience different delays. Two degrees of network complexity are dealt with: 1) tree-like networks, in which there is only one path from every network input to any network output and 2) networks with reconvergent fanouts, where more than one path exists from some inputs to some outputs.

To simplify analysis of very large circuits, an approximate model is proposed where the circuits are subdivided into large logic blocks. The analytical techniques previously derived for individual gates are then applicable. Various strategies for characterizing the delays of the large logic blocks are considered and examined by means of computer simulations.

Volume III B: "Computer Simulation of EMI Effects in a Differential Line Receiver" by Zino Chair, Tushar Dave, Hamza Ouibrahim, and Dr. Donald D. Weiner [6].

It is frequently necessary to transmit baseband digital data over long transmission lines such as system interconnect cables. When the cables are located in a high EMI environment, ordinary integrated logic circuits cannot be used to synthesize the line driver and receiver because such circuits are unable to discriminate between a valid signal and the externally induced interference. One solution for combating the interference is to convert the ground referenced digital data at the driver into a differential signal which is transmitted over a pair of wires such as a twisted-pair line. A differential line receiver is used at the other end. Interference which appears equally on each wire is referred to as common-mode interference. Ideally, the line receiver responds only to the differential signal transmitted over the line and rejects the common-mode interference.

This report describes some preliminary results dealing with the computer simulation of EMI effects due to sinusoidal interference in a DS 55115 differential line receiver. Attention is focused on the receiver, as opposed to the line driver, because the receiver is significantly more susceptible. Consequently, the susceptibility of the driver-receiver pair, in most cases, is determined by that of the receiver.

The computer program selected for the investigation was SPICE (Simulation Program with Integrated Circuit Emphasis) which was exercised in its transient mode. Thus, a time-domain analysis was performed and

time waveforms were generated at all nodes of interest. Parameter values of the semiconductor devices embedded in the integrated circuit for the receiver are not published in the interface handbooks. Reasonable values were determined by adjusting nominal values until the computer simulated characteristics closely agreed with typical performance characteristics supplied by the manufacturer. These included curves of 1) input current vs. input voltage, 2) output voltage vs. common-mode input voltage, 3) high level output voltage vs. high level output current, 4) low level output voltage vs. low level output current, 5) output voltage vs. differential input voltage, 6) output voltage vs. strobe input voltage, and 7) power supply current vs. power supply voltage.

The sinusoidal interference was impressed at the two data inputs, the strobe terminal, and the response-time control input. Waveform distortion in the output signal was noted for suitably strong interferers. Waveform parameters for describing the distortion are defined and plotted as a function of the frequency and/or amplitude of the sinusoidal interferer.

Particular attention is devoted to dc offsets caused by rectification in the base-to-emitter and base-to-collector transistor junctions. The input voltage at which the output changes state is defined as the input threshold voltage. The rectification of RF energy causes the input threshold voltage to change. The concept of using this change to define receiver susceptibility is examined.

In addition to decreasing the noise margin, a change in the input threshold voltage can cause time variations in the receiver output (i.e., pulses may appear shifted in time and some pulses may appear longer or shorter). The resulting jitter constrains the minimum pulse width and, therefore, the maximum data rate which can be used. This effect is examined as a function of the amplitude and/or frequency of the sinusoidal interference.

Volume IV A: "Coupling of Electromagnetic Fields into Transmission Lines: A comparison of the Transmission Line Model and the Method of Moments" by Robert Abraham and Dr. Clayton Paul [7].

The coupling of electromagnetic fields onto transmission lines is investigated. The transmission line model with distributed sources is employed as a computationally efficient method of predicting currents induced on transmission wires by an incident field. Results obtained from the transmission line model solution are compared with predictions made by the more rigorous, but much less efficient, method of moments technique. Two user-oriented computer codes, using different expansion and testing functions, were selected to provide the method of moments solution. Both the prediction accuracy and limitations of the transmission line model are explored in depth using a carefully selected transmission line structure. The structure is modified slightly to illustrate several important characteristics of the transmission line

model solution. Low frequency limitations of the method of moments solution are investigated. In addition, the differences between the two method of moments formulations are found to have a significant effect on the integrity of their individual solutions. These differences are illustrated. Finally, the practical use of the transmission line model as an effective method for predicting the coupling of an electromagnetic field into terminal devices is discussed.

Volume IV B: "Shield, A Digital Computer Program for Computing Crosstalk Between Shielded Cables" by Dr. Clayton Paul [8].

This report contains the description and verification of a digital computer program, SHIELD, to be used in the prediction of crosstalk in transmission lines consisting of unshielded wires and/or shielded cables. The line may be above a ground plane (Type 1) or within an overall, circular, cylindrical shield which may be solid or braided and a wire (the shielded wire) located concentrically on the axis of the shield. All wires may be stranded and all conductors are treated as imperfect conductors; that is, their per-unit-length impedances are nonzero. Through-braid coupling for braided shields as well as diffusion for both types are included in the model. The shielded cables may have exposed sections at either end (pigtail sections) in which the shielded wire is not covered by the shield. Over these pigtail sections, a pigtail wire, parallel to the shielded wire, connects the shield to the reference conductor at that end via either a short circuit or an open circuit. These pigtail sections are included in the representation to

simulate the common practice of terminating a shielded cable in a connector via these pigtail wires. The pigtail sections may be of different lengths. The program is written in FORTRAN IV and should be implementable on a wide range of digital computers.

Volume IV C: "Crosstalk in Twisted Wire Circuits" by Marty Jolly and Dr. Clayton Paul [9].

An investigation of wire-to-wire crosstalk is presented in an attempt to accurately predict the magnitude of the voltage coupled to a twisted wire pair. A sensitivity analysis of the twisted wire pair is conducted to determine the effect that line twist has on the coupled differential mode voltage when the twisted pair is connected in an unbalanced configuration. An improved computer model is developed to aid in the prediction of the voltage coupled to the twisted wire pair when it is terminated in low impedance loads. Another circuit configuration which is investigated consists of a differential line driver connected to a differential line receiver by a twisted wire pair. Predictions of the common mode voltage coupled to the twisted pair are computed with a single wire model and a comparison is made with experimental results.

Volume IV D: "Modeling Crosstalk in Balanced Twisted Pairs" by Dawn Koopman and Dr. Clayton Paul [10]

The coupling of electromagnetic fields to twisted wire pair transmission lines is investigated. A simple low-frequency model to predict the crosstalk of a three-conductor line is described. This low-frequency

model is used to demonstrate how the twisted pair reduces crosstalk. The sensitivity of the crosstalk from the single wire to unbalanced twisted pair is examined. The crosstalk from the unbalanced twisted pair to unbalanced twisted pair is measured and explained. Finally, the crosstalk in the single wire to balanced twisted pair is measured to illustrate that balancing the terminal configurations of the twisted pair can further reduce crosstalk.

Volume IV E: "Modeling of Transmission Lines: A Comparison of Lumped-Circuit Iterative Models and the Transmission Line Model" by Woodrow Everett III and Dr. Clayton Paul [11].

A comparison between the predictions of various lumped-circuit iterative models of transmission lines and that of the transmission line model is given for both the two and three-conductor cases. For frequencies such that the line length is approximately 1/10 of a wavelength, or less in one section, the lumped-circuit models yield predictions which are within ±3dB of the transmission line model predictions, and which are essentially independent of the value of load impedance. For frequencies where the line length is greater than approximately 1/10 of a wavelength, more than one section of the lumped models must be used to yield accurate predictions, but the prediction accuracy may be significantly affected by the load impedance value. The range of accurate predictions (in terms of electrical length) may be increased by adding more sections of a lumped-circuit model, but this range increases in a nonlinear fashion. Because of this nonlinear relationship, it is difficult to find a satisfactory method for

estimating the number of sections of a particular lumped-circuit model that must be used in order to obtain a desired range of accurate predictions.

Volume IVF: "Prediction of Crosstalk in Flatpack Coaxial Cables" by Wayne Beech and Dr. Clayton Paul [11A].

The electromagnetic crosstalk present in a class of cables known as flatpack, coaxial cables is investigated. The multiconductor transmission line equations are used to derive a model of a general flatpack, coaxial cable consisting of n cables. This model is then implemented as a digital computer program to allow simulation of the crosstalk levels present in the cable. This simulation is compared to experimental results to prove that the model is valid and can accurately predict the crosstalk levels. Also the effect of common impedance coupling, the presence of drain wires to allow for connection to the shields of the cable, and the presence of pigtail sections (exposed sections of wire) is examined to determine their effect on the overall electromagnetic crosstalk present in the cable.

Volume V: "Model Revision for the IEMCAP" by Dr. Clayton Paul [12].

This report contains recommendations for changes in the wire-to-wire coupling subroutine (WTWTFR) in the Intrasystem Electromagnetic Compatibility Analysis Program (IEMCAP). The changes are intended to accomplish four objectives: (1) to modularize that subroutine, (2) to speed up computation, (3) to provide models which have more sound theoretical basis than those presently included in IEMCAP, and (4) to correct certain errors

presently in the current models in IEMCAP. The first objective - to modularize the subroutine - is important from the standpoint of future maintenance of the code. The other three objectives concern relatively accurate and speedy predictions. It is important that the models have a sound theoretical basis rather than have the ability to predict only certain limited, empirical data. One then has some confidence that the models will predict some, as yet, uninvestigated situation.

The subroutine which was initially delivered by the contractor contained numerous theoretical inconsistencies and model prediction errors. These were thought to have been corrected via a completely rewritten subroutine. The models in that revised subroutine were based on the modeling efforts to that date. Shielded wires and twisted pairs had not been extensively investigated from the standpoint of models for predicting crosstalk. Thus models for those portions of the subroutine were based on limited modeling data which existed at the time.

Since that initial revision, several modifications were made to correct coding errors and to add features. The original revision was designed to handle pigtails on shielded wires which were three inches (3") in length. No provision was made for peripherally bonded shields (zero-length pigtails) or variable lengths of pigtails from shield to shield. Recently a revision was made to WTWTFR to allow for variable length pigtails. It has been determined that this revision did not correctly handle pigtails for inductive coupling. In the original revision, the restriction of 3" pigtails on all shield terminations allowed an optimization of the code which would not have been possible with variable length pigtails. Since that code structure and the models relied heavily on the restriction that all shield pigtail terminations be the same, it is not a simple matter to change that code to now handle

variable length pigtails. Moreover, adding the capability of variable length pigtails by modifying the original code would not take advantage of the optimization which the assumption of 3" pigtails allowed. It would seem, therefore, that one should rewrite and optimize the structure of the code for the variable length pigtail case rather than patching up the original revision.

Much additional work has been done on the modeling of crosstalk involving shielded wires and twisted pairs since that original code revision. This additional work has shown that some of the models for these cases contained in the original revision are not correct and some models were unnecessarily complicated for the prediction accuracies which one would reasonably expect on practical systems. In addition, some long-held, fundamental notions concerning the superposition of inductive and capacitive coupling (which were fundamental to the original revision) were shown to be incorrect.

Thus because of the additional modeling experience and the discovery of the error of certain fundamental model premises, the WTWTFR models need modification. Because of the extensiveness of these modifications as well as the other reasons alluded to above, it seems advisable to completely rewrite the WTWTFR subroutine. In doing so it is also advisable that it be modularized and optimized. Modularization is critically important from the standpoint of future maintenance. It is possible, but very difficult, for anyone who is not intimately (and currently) familiar with the present code to make changes to it much less track the effects of those changes through the code. Modularization would remedy this problem to a large degree.

Volume VI: "Basic EMC Technology Advancements for C^3 Systems" by Drs. Clayton Paul, Donald Weiner, and James Whalen.

This research effort was devoted to eliminating some of the basic technological gaps in the two important areas of 1) electromagentic effects (EM) on microelectronic circuits and 2) EM coupling and testing. The results are presented in fourteen reports which have been organized into six volumes. The reports are briefly summarized in this volume.

In addition, an experiment is described which was performed to demonstrate the feasibility of applying several of the results to a problem involving electromagnetic interference. Specifically, experimental results are provided for the randomness associated with 1) crosstalk in cable harnesses and 2) demodulation of amplitude modulated (AM) signals in operational amplifiers. These results are combined to predict candidate probability density functions (pdf's) for the amplitude of an AM interfering signal required to turn on a light emitting diode. The candidate pdf's are shown to be statistically consistent with measured data.

II. Theoretical Discussion of Feasibility Experiment

Since research was conducted on a number of different topics, it was decided to perform an experiment that demonstrated the feasibility of applying several of the results to a problem involving electromagnetic interference (EMI). The research areas encompassed by the experiment were:

1) EMC modeling and analysis using a probabilistic approach,

2) crosstalk in cable harnesses,

and

3) weakly nonlinear behavior of operational amplifiers.

This chapter discusses theoretical considerations associated with the experiment.

2.1 Probabilistic Model for a Typical EMI Problem

A typical EMI problem is illustrated in Fig. 2.1-1.

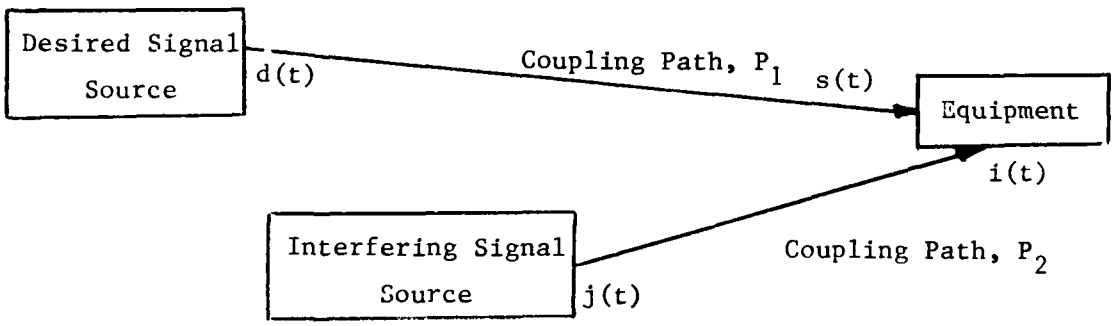

Fig. 2.1-1. A typical EMI problem

The desired signal for the equipment is denoted by d(t). It is transmitted to the equipment via coupling path, P_1, and is received as the signal, s(t). On the other hand, the interfering signal, j(t), is coupled to the equipment via path, P_2 and arrives as the signal, i(t). Uncertainties and/or randomness in

d(t), j(t), P_1 and P_2 result in a random behavior for both s(t) and i(t). Also, variability in such things as electrical components and the positioning of wires and cables result in a variation of performance from one piece of "identical" equipment to the next.

In the probabilistic approach [14,15,16], s(t) and i(t) are both treated as sample functions from random processes. In addition, the equipment is viewed as a sample from an ensemble of randomly distributed "identical" equipments whose EMI performance is characterized in terms of a random susceptibility level. The problem is then analyzed by determining the probability of EMI [16].

2.2 Description of the Experiment

A block diagram of the experiment is shown in Fig. 2.2-1. With respect to the discussion of section 2.1, the equipment interfered with is the printed circuit board (PCB). The network in the PCB was designed such that the light emitting diode (LED) turned on when the input voltage, V_2, exceeded the specified threshold, V_{2T}. The three stages of amplification served to amplify the input signal so that the output voltage, V_3, was just large enough to light the LED when $V_2 = V_{2T}$.

Normally, the LED was intended to be off. During the experiment an interfering signal was coupled to the PCB through a 25-wire random cable bundle. EMI occurred when, for large enough amplitudes of the interfering signal, the LED was turned on. Since the LED was normally off during the experiment, the desired signal in Fig. 2.1-1 was identically zero. Specifically,

$$d(t) = s(t) = 0. \qquad (2.2\text{-}1)$$

The interfering signal was selected to be the amplitude modulated (AM) signal

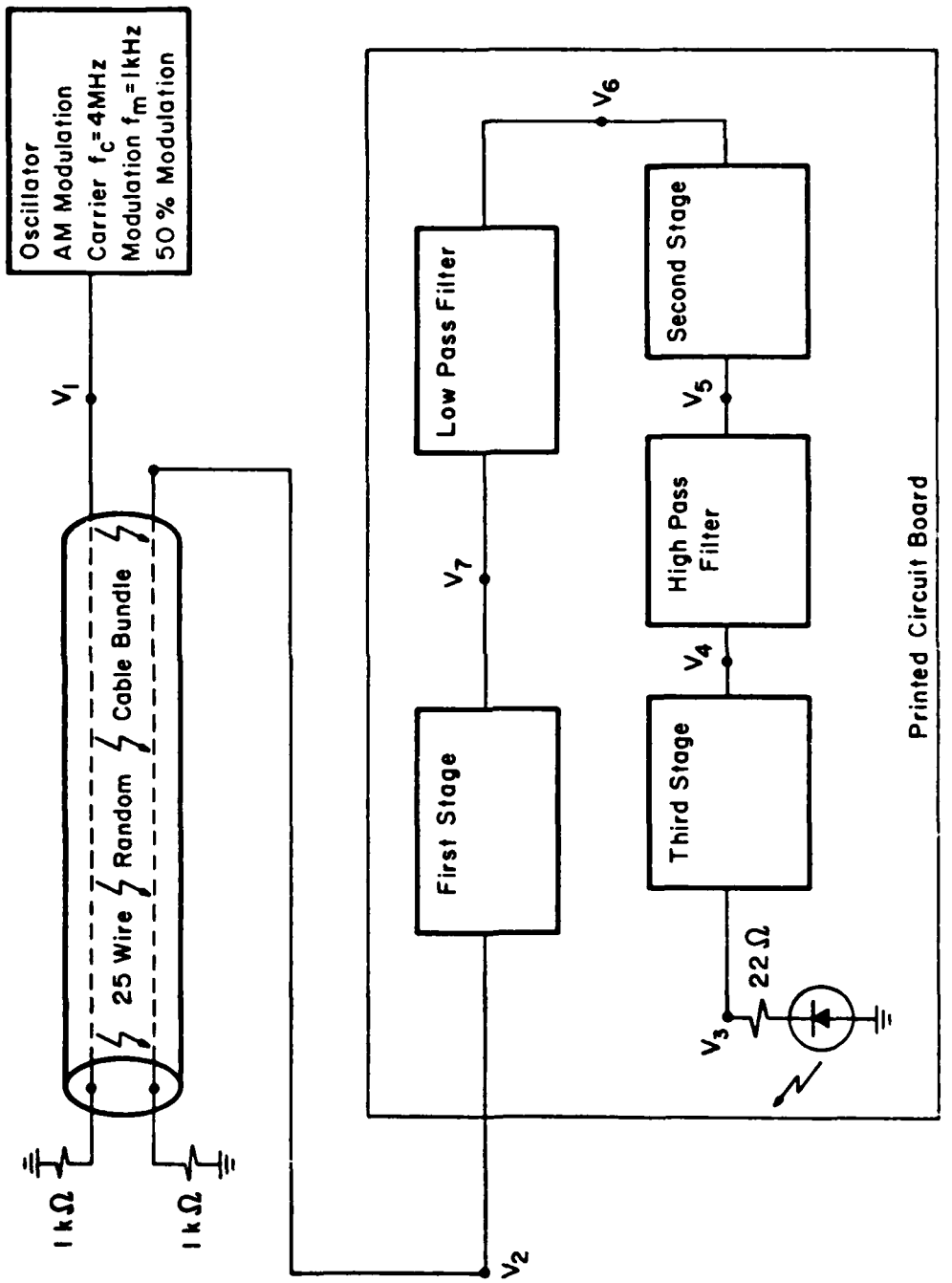

Fig. 2.2-1. Block diagram of experiment

with sinusoidal modulation given by

$$j(t) = A_1[1 + m \cos (2\pi f_m t)] \cos 2\pi f_c t. \qquad (2.2\text{-}2)$$

The numerical values of the parameters in Eq. (2.2-2) used in the experiment were $m = 0.5$, f_m = 1kHz, and f_c = 4MHz and 15 MHz.

The circuit schematic of the PCB is shown in Fig. 2.2-2. All three stages employ operational amplifiers. The first two stages are inverting amplifiers with DC gains of approximately 10 and 100, respectively. The third stage is a noninverting buffer with a DC gain of approximately 10. As a result, the overall DC voltage gain from the input voltage V_2 to the output voltage V_3 is approximately 10,000.

The AM interfering signal contains frequency components at $f_c - f_m$, f_c, and $f_c + f_m$. Since $f_m << f_c$, all of these frequencies are either at or very close to the carrier frequency. The low pass filter following the first stage, which consists of R_3 and C_2, has a 3-dB cut-off frequency of approximately 1700 Hz. Therefore, if the circuit behaved in a linear fashion, the interfering signal would be severely attenuated at the output of the PCB. As a result, the interference would not light the LED.

However, operational amplifiers are weakly nonlinear in the amplification region. Therefore, during the experiment, the first stage served to demodulate the interfering AM signal. The DC component of the modulation was prevented from appearing at the output by the blocking capacitor, C_3. On the other hand, the circuit amplified the 1kHz sinusoidal component of the modulation which fell well within the passband of the three stages. The LED was observed to light for large enough amplitudes of the interfering signal.

Lighting of the LED depended on two distinct phenomena:

1) the interfering signal was coupled to the PCB by means of crosstalk which

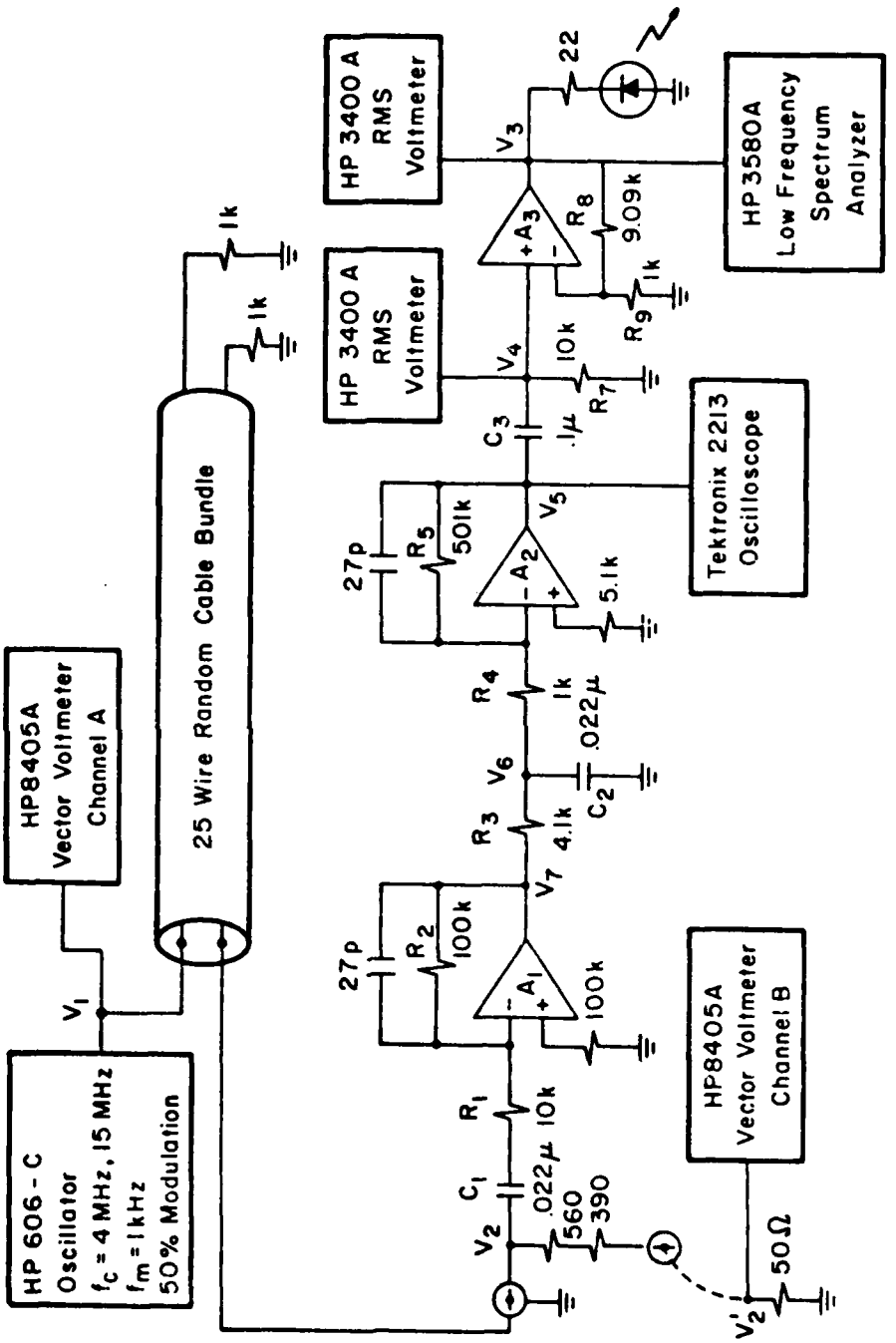

Fig. 2.2-2. Circuit schematic of PCB

occurred within the cable bundle and 2) a 1 kHz sinusoidal component was generated due to the weakly nonlinear behavior of the operational amplifier in the first stage. In chapter III it is shown that changing the wrapping of the cable bundle changes the strength of the interfering signal coupled to the PCB. In Chapter IV it is shown that changing the operational amplifier changes the amplitude of the generated sinusoidal component at 1 kHz. The two changes together result in various fluctuations in the amplitude of the interfering signal at V_1 needed to light the LED.

Separate experiments were carried out to determine the probability density functions of the quantities that characterize 1) crosstalk within the cable bundle and 2) demodulation of the interfering signal. These density functions were then combined analytically to determine the probability density function of the voltage at V_1 which results in a specified threshold voltage at V_3.

Another separate experiment was conducted in which the cable wrappings and operational amplifier in the first stage were changed many times. Cable wrappings and operational amplifiers from the previous experiments were not used. The voltages at V_1 required to produce a specified threshold voltage at V_3 were recorded. Finally, a statistical test was employed to determine whether the data for V_1 were statistically consistent with the analytically obtained probability density function for V_1.

2.3 Analysis of Weakly Nonlinear Effects in the Operational Amplifier

The interfering signal at the input to the cable bundle is an AM waveform of the form

$$j(t) = A_1[1+m \cos (2\pi f_m t)] \cos 2\pi f_c t \qquad (2.3\text{-}1)$$

Expansion of Eq.(2.3-1) and application of a well-known trigonometric identity results in

$$j(t) = A_1 \cos(2\pi f_c t) + \frac{mA_1}{2} \cos[2\pi(f_c - f_m)t] + \frac{mA_1}{2} \cos[2\pi(f_c + f_m)t]. \quad (2.3\text{-}2)$$

Let the cross talk within the cable bundle, from V_1 to V_2, be characterized by the linear voltage transfer function, G(f). Since f_m = 1kHz while f_c = 4mHz or 15 mHz,

$$f_c - f_m \cong f_c + f_m \cong f_c. \quad (2.3\text{-}3)$$

Therefore, it is reasonable to assume

$$G(f_c - f_m) \cong G(f_c + f_m) \cong G(f_c) = |G(f_c)| e^{j\sigma_c}. \quad (2.3\text{-}4)$$

Let the amplitude of the sinusoidal carrier at the output of the cable bundle be denoted by A_2. It follows that

$$A_2 = |G(f_c)| A_1. \quad (2.3\text{-}5)$$

Because the three components of Eq.(2.3-2) experience approximately the same gain and phase shift, it follows that the output of the cable bundle is a sinusoidally modulated AM signal given by

$$\begin{aligned} i(t) &= A_2[1 + m\cos(2\pi f_m t)]\cos(2\pi f_c t + \sigma_c) \\ &= A_2\cos(2\pi f_c t + \sigma_c) + \frac{mA_2}{2}\cos[2\pi(f_c - f_m)t + \sigma_c] \\ &\quad + \frac{mA_2}{2}\cos[2\pi(f_c + f_m)t + \sigma_c]. \end{aligned} \quad (2.3\text{-}6)$$

To simplify Eq.(2.3-6), it is convenient to define

$$f_1 = f_c - f_m \quad , \quad E_1 = |E_1| e^{j\sigma_c} = \frac{mA_2}{2} e^{j\sigma_c}$$

$$f_2 = f_c \quad , \quad E_2 = |E_2| e^{j\sigma_c} = A_2 e^{j\sigma_c} \tag{2.3-7}$$

$$f_3 = f_c + f_m \quad , \quad E_3 = |E_3| e^{j\sigma_c} = \frac{mA_2}{2} e^{j\sigma_c} \quad .$$

Eq. (2.3-6) may then be expressed as

$$i(t) = \sum_{q=1}^{3} |E_q| \cos(2\pi f_q t + \sigma_c)$$

$$= \frac{1}{2} \sum_{\substack{q=-3 \\ q \neq 0}}^{3} E_q e^{j2\pi f q t} \tag{2.3-8}$$

where

$$E_{-q} = |E_q| e^{-j\sigma_c} \quad \text{and} \quad f_{-q} = - f_q . \tag{2.3-9}$$

The operational amplifiers in the second and third stages of the PCB are assumed to behave linearly. However, the weakly nonlinear operational amplifier in the first stage is assumed to possess a second-order nonlinearity (i.e., the input signal driving the first stage is assumed to be small enough such that higher-order nonlinearities may be considered to be negligible.) In the experiment it is the second-order component at frequency, f_m, which is of interest.

From Eq.(2.3-8) it is obvious that i(t) contains the six input frequencies $f_{-3} = -f_3$, $f_{-2} = -f_2$, $f_{-1} = -f_1$, f_1, f_2, f_3. Let m_k denote the number of times the frequency f_k appears in a particular n^{th} -order frequency mix.

All possible n^{th} -order frequency mixes are then represented by the frequency mix vector

$$\underline{m} = (m_{-3}, m_{-2}, m_{-1}, m_1, m_2, m_3) \tag{2.3-10}$$

where

$$\sum_{k=-3}^{3} m_k = n. \tag{2.3-11}$$

The intermodulation frequency corresponding to $\underline{m}$ is

$$f_{\underline{m}} = \sum_{\substack{k=-3 \\ k\neq 0}}^{3} m_k f_k = (m_1 - m_{-1})f_1 + (m_2 - m_{-2})f_2 + (m_3 - m_{-3})f_3. \tag{2.3-12}$$

In terms of the nonlinear transfer function approach [17], the n^{th} - order response associated with $\underline{m}$ to the input given by Eq. (2.3-8) is

$$y_n(t;\underline{m}) = \frac{(n;\underline{m})}{2^{n-1}} |E_1|^{(m_1+m_{-1})} |E_2|^{(m_2+m_{-2})} |E_3|^{(m_3+m_{-3})} \tag{2.3-13}$$

$$|H_n(\underline{m})| \cos[2\pi f_{\underline{m}} t + \sigma_{\underline{m}} + \psi_{\underline{n}}(\underline{m})]$$

where $(n;\underline{m})$ is the multinomial coefficient defined by

$$(n;\underline{m}) = \frac{(n!)}{(m_{-3}!)(m_{-2}!)(m_{-1}!)(m_1!)(m_2!)(m_3!)} \tag{2.3-14}$$

$H_n(\underline{m})$ is the n^{th} -order nonlinear transfer function given by

$$H_n(\underline{m}) = |H_n(\underline{m})| \, e^{j\psi_n(\underline{m})} \tag{2.3-15}$$

$$= H_n(\underbrace{f_{-3},\ldots,f_{-3}}_{m_{-3}},\ldots,\underbrace{f_{-1},\ldots,f_{-1}}_{m_{-1}},\ldots,\underbrace{f_1,\ldots,f_1}_{m_1},\ldots\underbrace{f_3,\ldots,f_3}_{m_3})$$

and

$$\sigma_{\underline{m}} = \sum_{\substack{k=-3 \\ k\neq 0}}^{3} m_k \sigma_c = [(m_1 - m_{-1}) + (m_2 - m_{-2}) + (m_3 - m_{-3})]\sigma_c. \tag{2.3-16}$$

Eqs. (2.3-13) through (2.3-16) are now specialized to the second-order response at frequency, f_m.

With respect to the frequencies defined in Eq. (2.3-7), the frequency mixes which result in a second-order reponse at f_m are:

a) $(f_2 - f_1)$

b) $(f_3 - f_2)$.

The frequency mix vector corresponding to the mix $(f_2 - f_1)$ is

$$\underline{m}_1 = (0,0,1,0,1,0) \tag{2.3-17}$$

while that corresponding to the mix $(f_3 - f_2)$ is

$$\underline{m}_2 = (0,1,0,0,0,1). \tag{2.3-18}$$

The associated multinomial coefficients are

$$(2;\underline{m}_1) = (2;\underline{m}_2) = 2. \tag{2.3-19}$$

In addition,

$$\begin{aligned} \sigma_{\underline{m}_1} &= (m_2 - m_{-1})\,\sigma_c = 0 \\ \sigma_{\underline{m}_2} &= (m_3 - m_{-2})\sigma_c = 0. \end{aligned} \tag{2.3-20}$$

It follows that the total second-order response at f_m is

$$\begin{aligned} y_2(t;f_m) &= y_2(t;\underline{m}_1) + y_2(t;\underline{m}_2) \\ &= |E_1||E_2||H_2(-f_1,f_2)| \cos[2\pi(f_2 - f_1)t + \psi_2(\underline{m}_1)] \\ &+ |E_2||E_3||H_2(-f_2,f_3)| \cos[2\pi(f_3 - f_2)t + \psi_2(\underline{m}_2)] \end{aligned} \tag{2.3-21}$$

Finally, use of Eqs. (2.3-7) in Eq.(2.3-21) yields

$$y_2(t;f_m) = \frac{mA_2^2}{2} |H_2(-f_1,f_2)| \cos (2\pi f_m t + \psi_2(\underline{m}_1)) + \frac{mA_2^2}{2} |H_2(-f_2,f_3)| \cos (2\pi f_m t + \psi_2(\underline{m}_2)). \quad (2.3\text{-}22)$$

The above result can be simplified even further.

Because of Eq. (2.3-3),

$$f_1 \cong f_3 \cong f_2 = f_c. \quad (2.3\text{-}23)$$

Consequently,

$$H_2(-f_1,f_2) \cong H_2(-f_2,f_3) \cong H_2(-f_c,f_c). \quad (2.3\text{-}24)$$

$H_2(-f_c,f_c)$ is associated with the frequency mix, (f_c-f_c), which yields a DC component. Therefore, $H_2(-f_c,f_c)$ is a purely real quantity. Since $H_2(-f_1,f_2)$ and $H_2(-f_2,f_3)$ are both approximately real,

$$\psi_2(\underline{m}_1) \cong \psi_2(\underline{m}_2) \cong 0. \quad (2.3\text{-}25)$$

Therefore, Eq.(2.3-22) simplifies to

$$y_2(t;f_m) \cong mA_2^2 |H_2(-f_c,f_c)| \cos 2\pi f_m t. \quad (2.3\text{-}26)$$

Utilizing Eq.(2.3-5), the amplitude of the sinusoidal component at f_m is given by

$$mA_2^2 |H_2(-f_c,f_c)| = m|G(f_c)|^2 A_1^2 |H_2(-f_c,f_c)|. \quad (2.3\text{-}27)$$

2.4 Probabilistic Analysis of Experiment

Instead of analyzing the circuit in Fig. 2.2-2 stage by stage, it is convenient to treat the entire PCB as a single system having input V_2 and

output V_3. This is readily accomplished by defining the second-order nonlinear transfer function of the previous section such that it relates the AM interference at V_2 to the 1kHz tone at V_3. In this way, $H_2(-f_c,f_c)$ accounts for the linear amplification provided by the second and third stages in addition to the weakly nonlinear behavior of the first stage. With this definition, $y_2(t;f_m)$ of the previous section corresponds to $V_3(t)$. Let A_3 denote the amplitude of the 1kHz tone at V_3. Then Eq. (2.3-26) can be written as

$$V_3(t) = A_3 \cos 2\pi f_m t \tag{2.4-1}$$

where

$$\begin{aligned} A_3 &= mA_2^2 |H_2(-f_c,f_c)| \\ &= m|G(f_c)|^2 A_1^2 |H_2(-f_c,f_c)|. \end{aligned} \tag{2.4-2}$$

During the experiment V_1 was increased until the LED was lit. Denote the values of A_1 and A_3 at which the LED switched on by A_{1T} and A_{3T}, respectively. From Eq. (2.4-2), A_{3T} and A_{1T} are related by

$$A_{3T} = m|G(f_c)|^2 A_{1T}^2 |H_2(-f_c,f_c)|. \tag{2.4-3}$$

The experiment was repeated many times. For each run, the cable was rewrapped and a different operational amplifier was placed in the first stage. The rewrappings resulted in random values for $|G(f_c)|$. Similarly, changing the operational amplifier yielded random values for $|H_2(-f_c,f_c)|$. In this section the probability density function for A_{1T} is derived given a specified value for A_{3T} and the probability density functions for $|G(f_c)|$ and $|H_2(-f_c,f_c)|$.

From Eq. (2.4-3), A_{1T} is given by

$$A_{1T} = \left[\frac{A_{3T}}{m}\right]^{\frac{1}{2}} \frac{1}{|G(f_c)|[|H_2(-f_c,f_c)|]^{\frac{1}{2}}} \quad . \tag{2.4-4}$$

For ease of analysis, let the random variables associated with $|G(f_c)|$ and $|H_2(-f_c,f_c)|$ be denoted by G and H, respectively. Also, let values assumed by the random variables A_{1T}, G, and H be denoted by a_{1T}, g, and h, respectively. The probability density function of A_{1T} is obtained by considering the following two functions of two variables

$$A_{1T} = k(G,H) = \left[\frac{A_{3T}}{m}\right]^{\frac{1}{2}} \frac{1}{G[H]^{\frac{1}{2}}}$$

$$W = \ell(G,H) = H. \tag{2.4.5}$$

In terms of the values assumed by the random variables,

$$a_{1T} = k(g,h) = \left[\frac{A_{3T}}{m}\right]^{\frac{1}{2}} \frac{1}{g[h]^{\frac{1}{2}}}$$

$$w = \ell(g,h) = k \tag{2.4-6}$$

The Jacobian of the transformation in Eq. (2.4-6) is

$$J(g,h) = \begin{vmatrix} \frac{\partial k(g,h)}{\partial g} & \frac{\partial k(g,h)}{\partial k} \\ \frac{\partial \ell(g,h)}{\partial g} & \frac{\partial \ell(g,h)}{\partial h} \end{vmatrix}$$

$$= \begin{vmatrix} -\left[\frac{A_{3T}}{m}\right]^{\frac{1}{2}} \frac{1}{g^2[h]^{\frac{1}{2}}} & -\frac{1}{2}\left[\frac{A_{3T}}{m}\right]^{\frac{1}{2}} \frac{1}{g[h]^{3/2}} \\ 0 & 1 \end{vmatrix}$$

$$= -\left[\frac{A_{3T}}{m}\right]^{\frac{1}{2}} \frac{1}{g^2[h]^{\frac{1}{2}}} \quad . \tag{2.4-7}$$

Let the probability density functions for G and H be denoted by $f_G(g)$ and $f_H(h)$, respectively. Also, let the joint probability density function for the random variables A_{1T} and W be denoted by $f_{A_{1T}W}(a_{1T},w)$. Solution of Eqs. (2.4-6) for g and h in terms of a_{1T} and w yields

$$g = \left[\frac{A_{3T}}{m}\right]^{\frac{1}{2}} \frac{1}{a_{1T}[w]^{\frac{1}{2}}}, \qquad h = w. \tag{2.4-8}$$

Assuming G and H to be statistically independent, it can be shown that [18]

$$f_{A_{1T}W}(a_{1T},w) = \frac{1}{|J(g,h)|} f_G(g) f_H(h) \Bigg|_{\substack{g = \left[\frac{A_{3T}}{m}\right]^{\frac{1}{2}} \frac{1}{a_{1T}[w]^{\frac{1}{2}}} \\ h = w}} \tag{2.4-9}$$

$$= \left[\frac{A_{3T}}{m}\right]^{\frac{1}{2}} \frac{1}{a_{1T}^2[w]^{\frac{1}{2}}} f_G\left(\left[\frac{A_{3T}}{m}\right]^{\frac{1}{2}} \frac{1}{a_{1T}[w]^{\frac{1}{2}}}\right) f_H(w)$$

Finally, $f_{A_{1T}}(a_{1T})$ is obtained by integrating $f_{A_{1T}W}(a_{1T},w)$ over all possible values of w. This results in

$$f_{A_{1T}}(a_{1T}) = \left[\frac{A_{3T}}{m}\right]^{\frac{1}{2}} \frac{1}{a_{1T}^2} \int_{-\infty}^{\infty} \frac{1}{[w]^{\frac{1}{2}}} f_G\left(\left[\frac{A_{3T}}{m}\right]^{\frac{1}{2}} \frac{1}{a_{1T}[w]^{\frac{1}{2}}}\right) f_H(w)\,dw. \tag{2.4-10}$$

Because w = h, a more convenient form of Eq.(2.4-10) is

$$f_{A_{1T}}(a_{1T}) = \left[\frac{A_{3T}}{m}\right]^{\frac{1}{2}} \frac{1}{a_{1T}^2} \int_{-\infty}^{\infty} \frac{1}{[h]^{\frac{1}{2}}} f_G\left(\left[\frac{A_{3T}}{m}\right]^{\frac{1}{2}} \frac{1}{a_{1T}[h]^{\frac{1}{2}}}\right) f_H(h)\,dh. \tag{2.4-11}$$

It is seen that knowledge of A_{3T} and the probability density functions for G and H is sufficient to determine the probability density function for A_{1T}.

III. Crosstalk Variations in Cable Harnesses

Inadvertent electromagnetic coupling between wires in cable bundles (crosstalk) is recognized as a potentially serious cause of degradation in the performance of an electronic system. Numerous methods of combatting crosstalk have been utilized in the past [19]. Those methods involve the use of shielded and/or twisted wires as well as filters. In many cases a simple rerouting of the wires into other cable harnesses can bring about crosstalk reduction. Of course, the degree to which rerouting wires reduces the crosstalk depends on the spectral content of the signals on adjacent wires in the harness as well as the degree of coupling between those wires.

In recent years, methods of mathematically modeling this crosstalk to determine its degree of severity have been developed and studied. All of these modeling techniques rely on the theory of the distributed parameter, multiconductor transmission line model. For frequencies such that the cable length is sufficiently short, electrically, lumped parameter approximations to this basic model are sufficient. For controlled configurations wherein the relative wire spacings are known and controlled along the cable bundle, this model has been shown to yield accurate predictions of the crosstalk [19].

Although current harness technology is making more frequent use of the controlled characteristic flatpack types, there exist a large proportion of the cable harnesses which may be classified as random cable bundles. In these traditional types of cable harnesses, the wires are held in close proximity by lacing cord, cable ties, etc. The exact, relative positions of the wires are unknown and moreover vary along the cable bundle. Two supposedly identical harnesses in two supposedly identical systems will, in reality exhibit quite different crosstalk properties.

Also, these crosstalk properties depend quite strongly on the terminal loads attached to the ends of the wires. In a recent study [20], this effect was shown to be significant. A 25-wire random cable bundle shown in Fig. 3-1 was constructed of #22 gauge stranded wires suspended 2.4 cm above a ground plane. The cable length was 4 m and the wires were inserted into connectors at each end as shown in Fig. 3-2. These connectors were attached to circuits which were mounted on a 2 foot x 16 foot, 1/8 inch thick aluminum ground plane to provide the terminal loads shown in Fig. 3-1. The wires were held together with nylon lacing cord. Wire 25 was driven at the left end by a sinusoidal oscillator whose frequency was varied from 1 kHz to 100 MHz in discrete steps. The other end of the wire was terminated to the ground plane with a resistor R. Wire 14 was also terminated at both ends with a resistor R. The received voltage (crosstalk) at the left end of this wire was measured. The voltage transfer ratio is then the ratio of this received voltage to the voltage applied to wire 25. Two values of R were used: R = 50 Ω and R = 1 kΩ. Those values were chosen so that the two coupling mechanisms - capacitive and inductive coupling - could be accentuated. The characteristic impedance, Z_C, of one #22 gauge wire 2.4 cm above ground is on the order of 300 Ω. Thus when R = 50 Ω, $R < Z_C$ and capacitive coupling will predominate. When R = 1 kΩ, $R > Z_C$ and inductive coupling will predominate.

In order to investigate the sensitivity of the crosstalk to variations in relative wire position as well as load impedance, the following experiment was conducted. The bundle was initially wrapped and suspended 2.4 cm above the ground plane by styrofoam supports. Next, the R = 50 Ω loads were attached and the crosstalk measured for frequencies from 1 kHz to 100 MHz. Then the R = 1 kΩ loads were attached and the frequency response remeasured. These data constitute the results for cable #1.

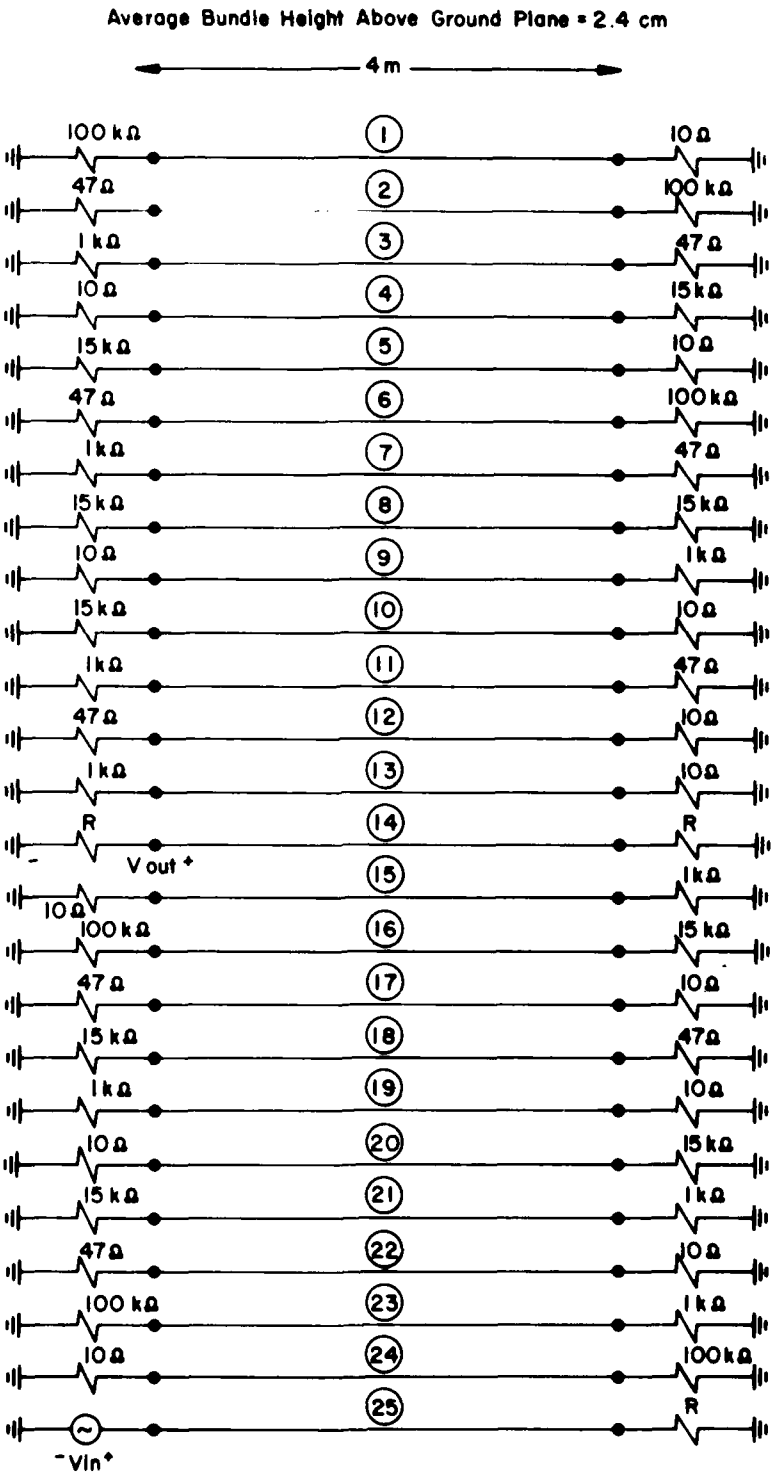

Fig. 3-1. The 25-wire random cable bundle.

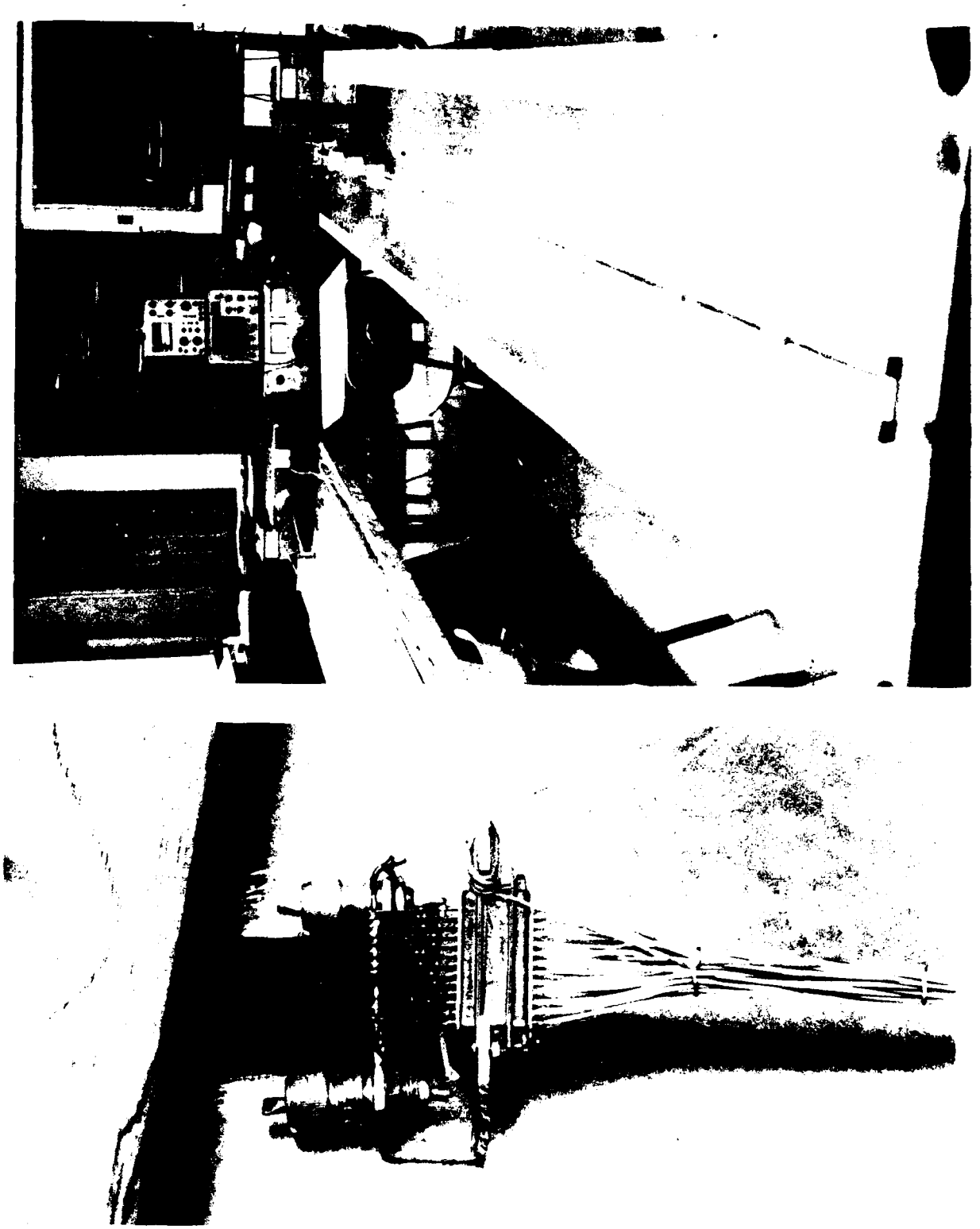

Fig. 3-2. The experimental configuration.

The lacing cord was then removed, the cable rewrapped and the above data were taken again. This constitutes the data for cable #2. This was repeated 8 times to give data for a total of 10 cables. Note that the R = 50 Ω and R = 1 kΩ data for each cable were for the exact same cable. Thus any differences in sensitivity which are found for these two different loads would clearly indicate the dependence on load impedance of that sensitivity.

The results are plotted in Fig. 3-3 for R = 50 Ω and in Fig. 3-4 for R = 1 kΩ. Note in Fig. 3-3 that for R = 50 Ω, there is virtually no sensitivity to variations in relative wire position caused by rewrapping the cable bundle. On the other hand, note in Fig. 3-4 for R = 1 kΩ that a change in crosstalk of as much as 20 dB occurs when the cable bundle is rewrapped. Note also that this occurs even for frequencies where the cable is electrically very short. Thus for R = 1 kΩ, these 10, supposedly identical cable bundles in fact exhibit quite different crosstalk characteristics.

Also plotted on these data are the predictions of a typical computer program, the Intrasystem Electromagnetic Compatibility Analysis Program, IEMCAP [21]. This is representative of similar "worst case" models which attempt to bound this variability. In addition, upper and lower bounds obtained with tolerance intervals based on the statistics of the data are shown [20].

The crosstalk data may represent an important part of some overall transfer function for interference. Even though the remainder of the transfer function is characterized by little or no variability, variability of the crosstalk may render any deterministic predictions meaningless unless they are upper bounds. Even then, these upper bounds may be severely pessimistic resulting in considerable overdesign. A more appropriate method of characteriz-

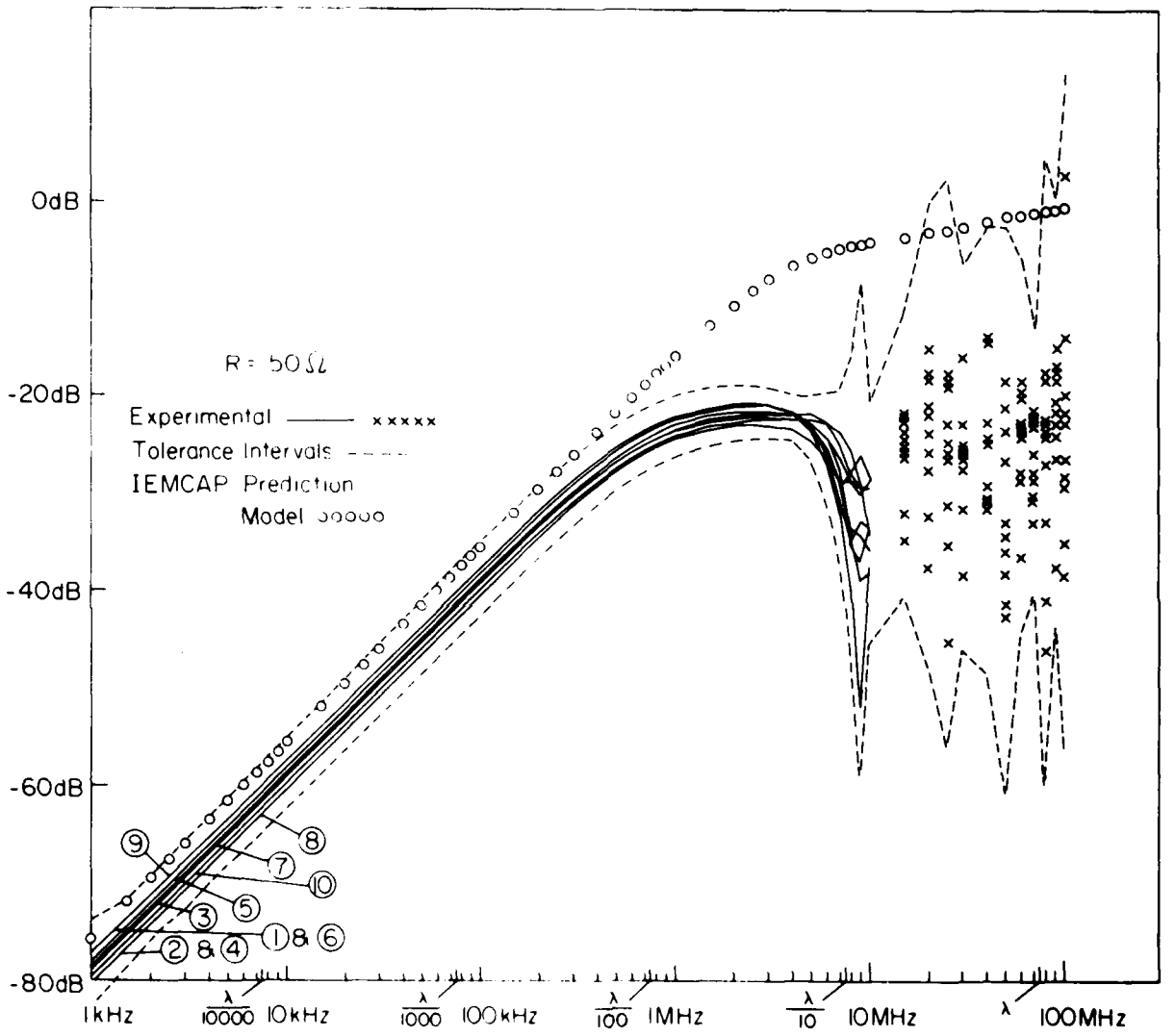

Crosstalk (dB) vs. Frequency

Fig. 3-3. Data for R = 50Ω loads.

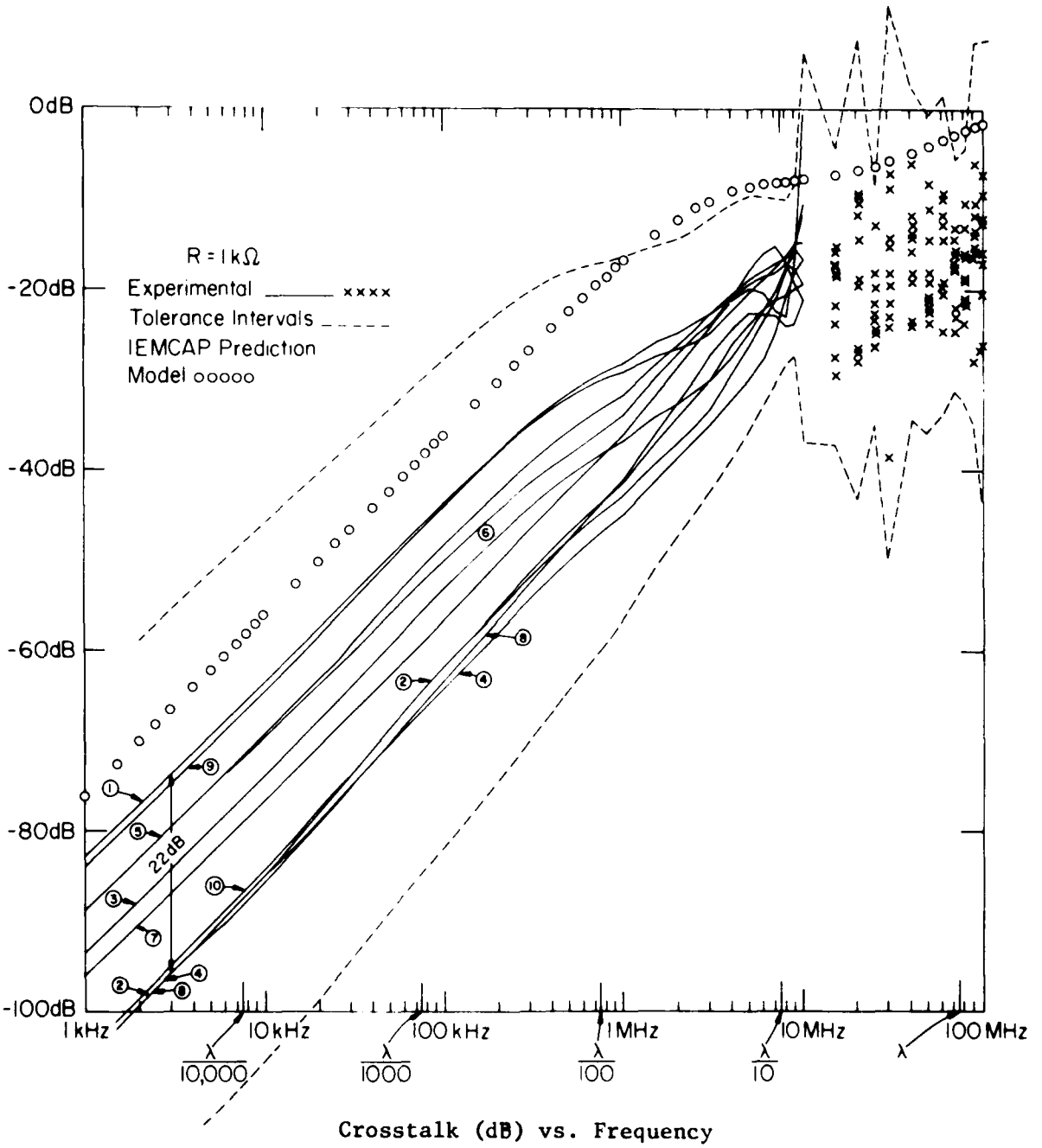

Crosstalk (dB) vs. Frequency

Fig. 3-4. Data for R = 1kΩ loads.

ing this crosstalk for the purposes of estimating potential problems would seem to be the statistical approach alluded to in the previous chapter.

Other portions of an overall transfer function may exhibit similar variabilities. A specific example of this is discussed in the next chapter with regard to variability in the nonlinear transfer functions of Op Amps. In chapter 5, an experiment is detailed which contains both aspects of this variability. The purpose will be to investigate the feasibility of combining separate sets of statistics on various portions of a transfer function to determine the overall statistics of the transfer function.

IV. Statistics of Measured Demodulation RFI responses in Operational Amplifier Circuits.

The specific RFI effect investigated was demodulation of amplitude-modulated (AM) RF signals in operational amplifiers (op amps) to produce undesired low frequency responses at the AM-modulation frequency. The undesired demodulated response may then be processed as a desired low frequency signal by the low frequency components that follow the op amp. In this chapter, the investigation of an op amp unity gain buffer amplifier configuration and a 3-stage [2] op amp configuration will be discussed. The op amp types chosen are the widely used 741 bipolar op amps which have conventional npn input transistors, the newer LM10 bipolar op amps which have less conventional pnp input transistors, the LF355 JFET-bipolar op amps which have junction field-effect-transistor (JFET) input transistors, and the CA081 MOS-bipolar op amps which have metal-oxide-semiconductor field-effect transistor (MOSFET) input transistors. Information on the units tested is summarized in Table 4-1 and Table 4-2. The second-order transfer function $H_2(-f_c,f_c)$, which characterizes the RFI demodulation response, was determined from the measured data. The scatter plot and statistics such as mean and standard deviation of $H_2(-f_c,f_c)$ for 25 to 30 units of each op amp type tested will be presented.

TABLE 4-1

OPERATIONAL AMPLIFIERS TESTED

Desig.	741	LM10	CA081	LF355
Type	Bipolar	Bipolar	Bi-MOS	Bi-FET
Input	npn	pnp	MOSFET	JFET
Interior	bipolar	bipolar	bipolar	bipolar
Units	30	25	30	30
Codes	5	4	2	4
Manu.	2	1	1	1

TABLE 4-2

MAKER AND PRODUCTION DATA INFORMATION OF THE 30 741 OP AMPS

Group	Units	Maker	Year	Week
1	5	RCA	1981	27
2	5	Fairchild	1976	36
3	10	Fairchild[a]	1981	38
4	5	Fairchild[a]	1981	35
5	5	Fairchild[b]	1982	49

[a] Manufactured in Hong Kong.

[b] Manufactured in Korea.

4.1 The Unity Gain Buffer Amplifier and Its Linear Response

The linear response of an amplifier is also called its first-order transfer function. Before starting measurements of the second-order transfer function of a nonlinear circuit, measurement of the linear response is usually performed to check the normal operation of the amplifier circuit. Figure 4-1 shows the experimental set-up for measuring the linear response of an op amp unity gain buffer. In this measurement, the input voltage amplitude V_i was held constant at 50 mV while the output voltages V_{01} and V_{02} were measured corresponding to $R_x = 0$ and $R_x = 50\ \Omega$, respectively. Then the linear response V_o/V_i corresponding to $R_x = \infty$ can be derived from the expression

$$\frac{V_o}{V_i} = \left(\frac{100}{V_{02}(mV)} - \frac{50}{V_{01}(mV)}\right)^{-1}, \quad R_x = \infty \qquad (4\text{-}1)$$

The reason for using this scheme is that the linear response of an op amp unity gain buffer is a function of load resistance at RF frequencies where the loop-gain is small. The coaxial cable which connects the output node V_o to the input of RF voltmeter has to be terminated by a 50 Ω resistor, which loads the amplifier output. Therefore the linear response corresponding to $R_x = \infty$ which corresponds to not connecting the RF voltmeter, has to be derived indirectly from Eq. (4-1). Figures 4-2 to 4-5 show the linear responses of the unity gain configuration of the 741, LM10, CA081, and LF355 op amps, respectively.

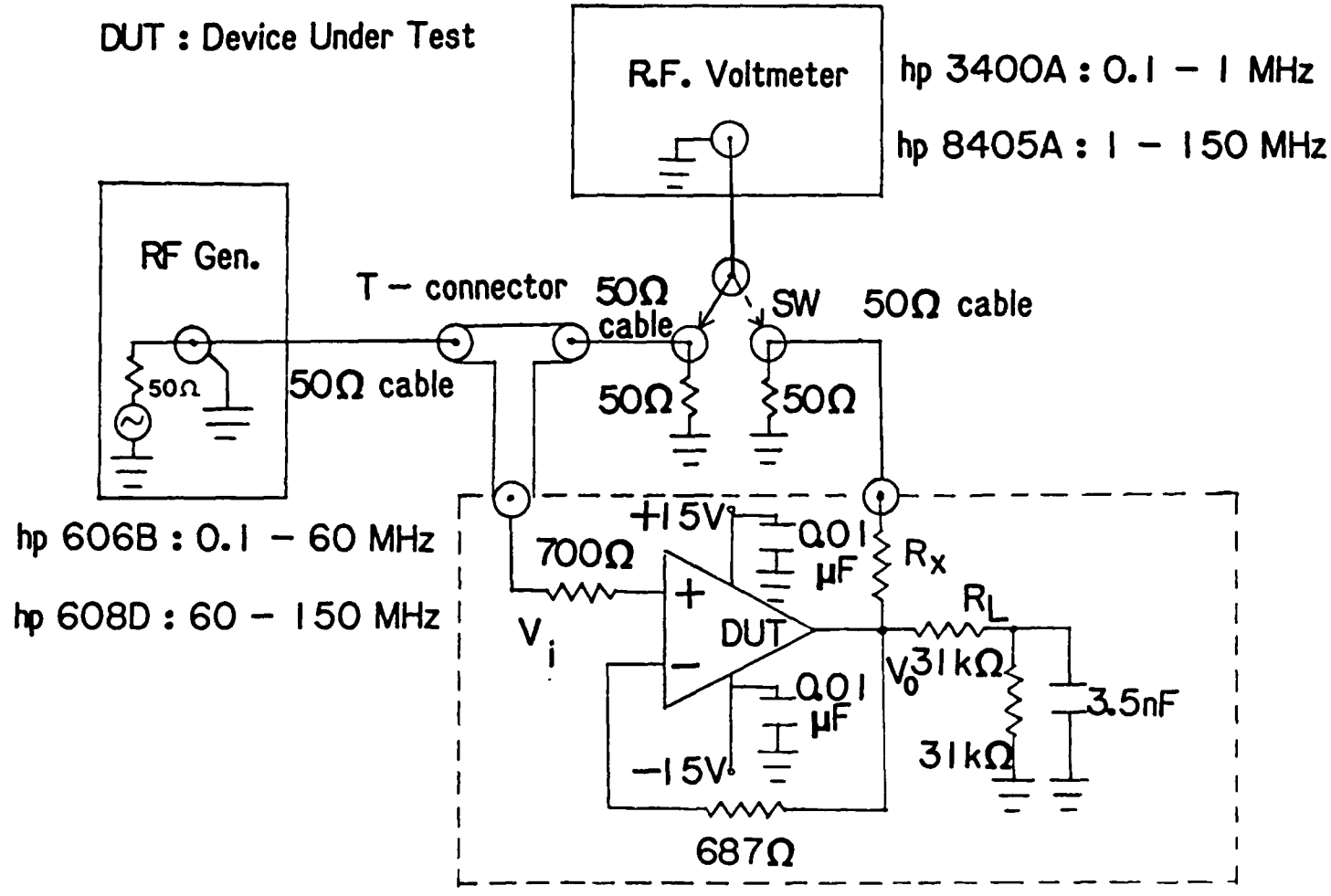

Fig. 4-1. Experimental set-up for linear response measurement V_o/V_i for the 10 kHz to 200 MHz frequency range. Data are taken with $R_x = 0$ and $R_x = 50$ ohm in order to calculate the response with $R_x = \infty$. With $R_x = \infty$, the op amp is loaded only by $R_L = 31$ kohm because the 3.5 nF capacitor is an ac short-circuit above 1.5 kHz.

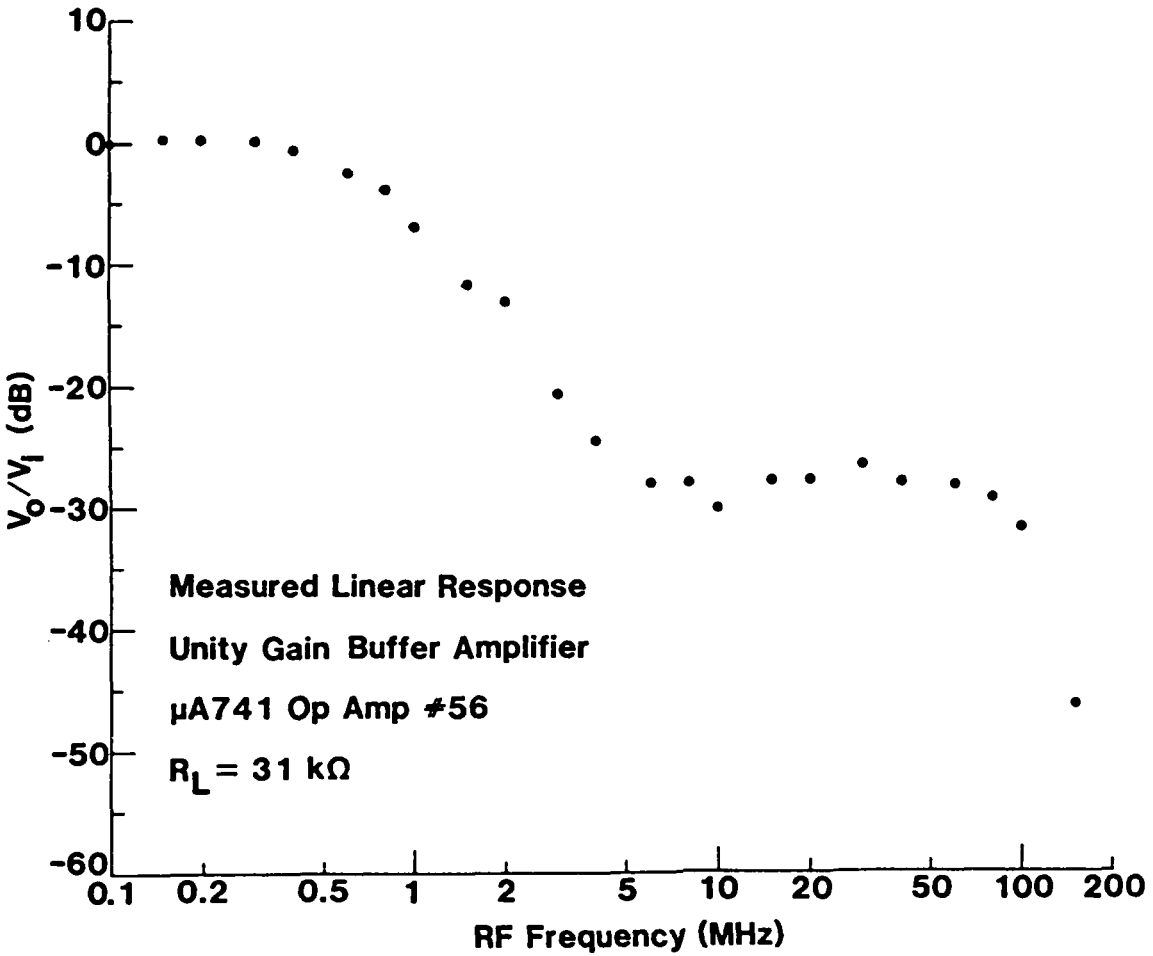

Fig. 4-2. Linear response V_o/V_i vs frequency for μA741 op amp #56 in unity gain buffer amplifier circuit.

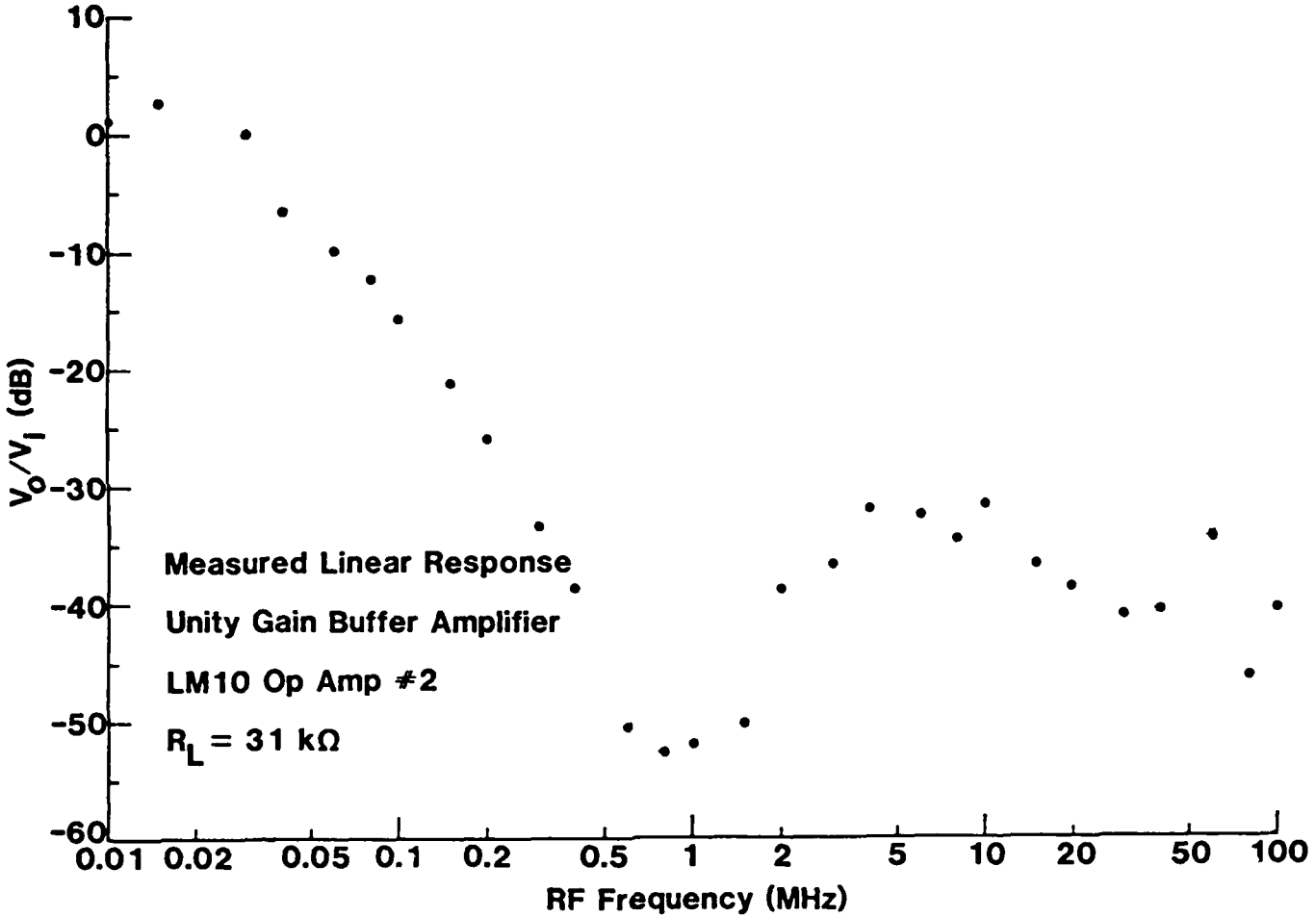

Fig. 4-3. Linear response V_o/V_i vs frequency for LM10 op amp #2 in unity gain buffer amplifier circuit.

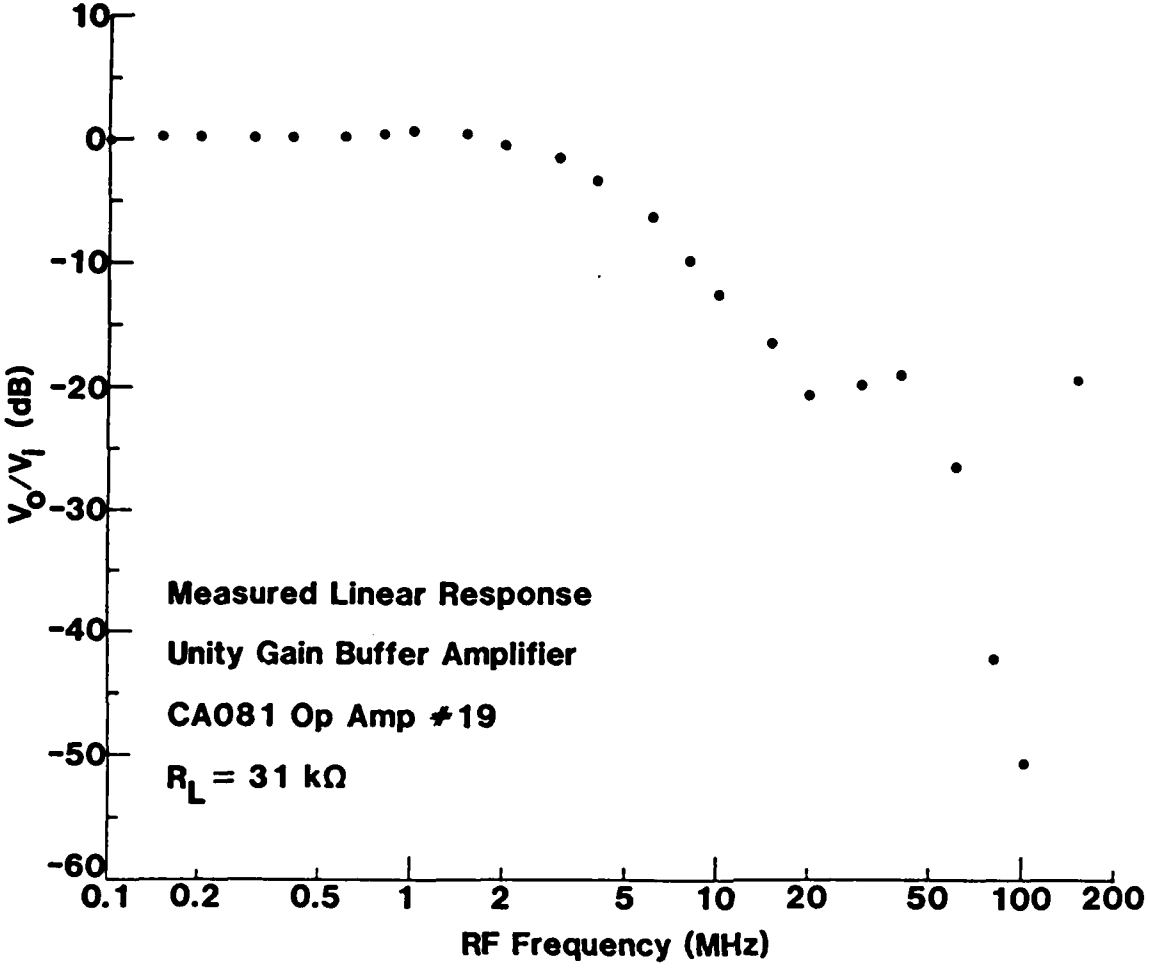

Fig. 4-4. Linear response V_o/V_i vs frequency for CA081 op amp #19 in unity gain buffer amplifier circuit.

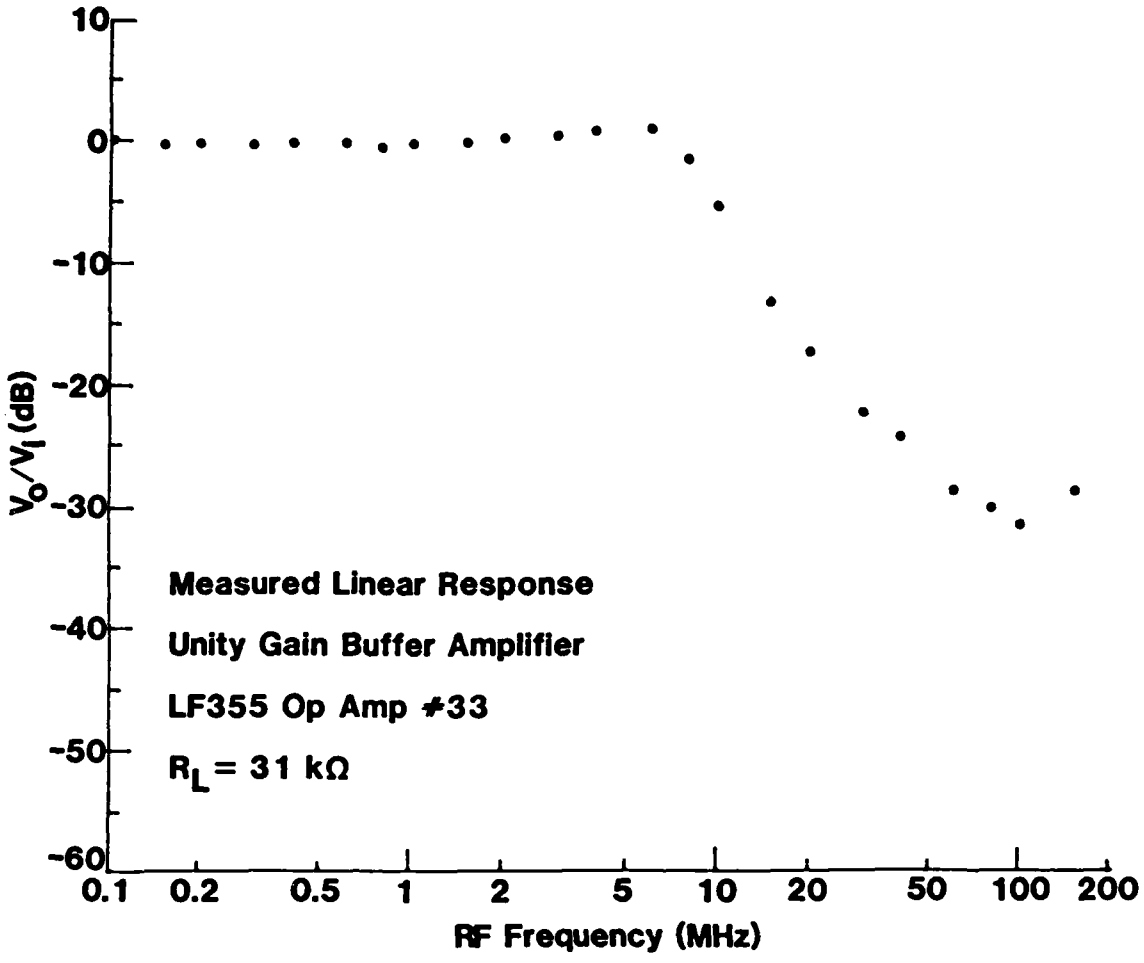

Fig. 4-5. Linear response V_o/V_i vs frequency for LF355 op amp #33 in unity gain buffer amplifier circuit.

Examining the data shown in Figures 4-2 to 4-5, we observe that the unity gain buffer stage linear frequency response is down 3 dB at 0.03 MHz for the LM10, is down 3 dB at 0.7 MHz for the 741, is down 3 dB at 4 MHz for the CA081, and is down 3 dB at 7 MHz for the LF355. These results indicate that the gain-bandwidth product for the unity gain buffer amplifier configuration is lowest for the LM10 and highest for the LF355. However, we should note that the linear responses were measured for only one unit of each op amp type. Our results are consistent with the typical data for these op amps provided by manufacturers except that for the order of the CA081 and LF355. See Ref. [2] for a plot of manufacturer's typical data.

4.2 Measurement of Demodulation RFI Response of Unity Gain Buffer

From the previous section, we have just shown that all four op amps are best operated at frequencies less than 10 MHz in the unity gain buffer configuration. Now, we are going to demonstrate how amplitude-modulated (AM) RF signals are demodulated to produce undesired audio frequency signals which fall into the normal frequency range of the op amp circuit [22].

The block diagram of the experimental system for measuring the demodulation RFI response is shown in Figure 4-6. The RF signal generator injects into the non-inverting input of the op amp circuit an amplitude-modulated RF signal, V_g, which may be expressed as

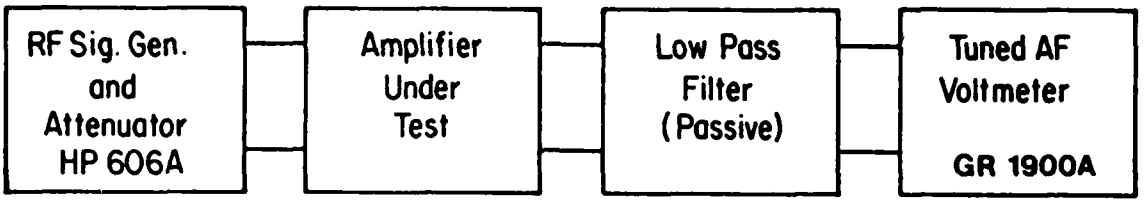

Fig. 4-6. Block diagram of system used to measure RFI.

$$V_g(t) = A(1 + m\cos 2\pi f_m t)\cos 2\pi f_c t \qquad (4\text{-}2)$$

where A is the amplitude of the RF signal without modulation ($m = 0$), m is the modulation index, f_m is the frequency of modulation, and f_c is the RF signal frequency. The low pass filter is inserted between the amplifier output and the tuned AF voltmeter in order to reduce the RF signals entering the AF voltmeter input. This is done to eliminate the possibility that an amplitude-modulated RF signal entering the AF voltmeter would generate audio frequency responses in the tuned AF voltmeter. Figure 4-7 shows a more detailed circuit diagram for the measurement system. Notice that the 50 Ω coaxial cable from the RF source to the circuit has been terminated with a 50 Ω resistor to eliminate the reflection of the RF signal at the receiving end of the cable.

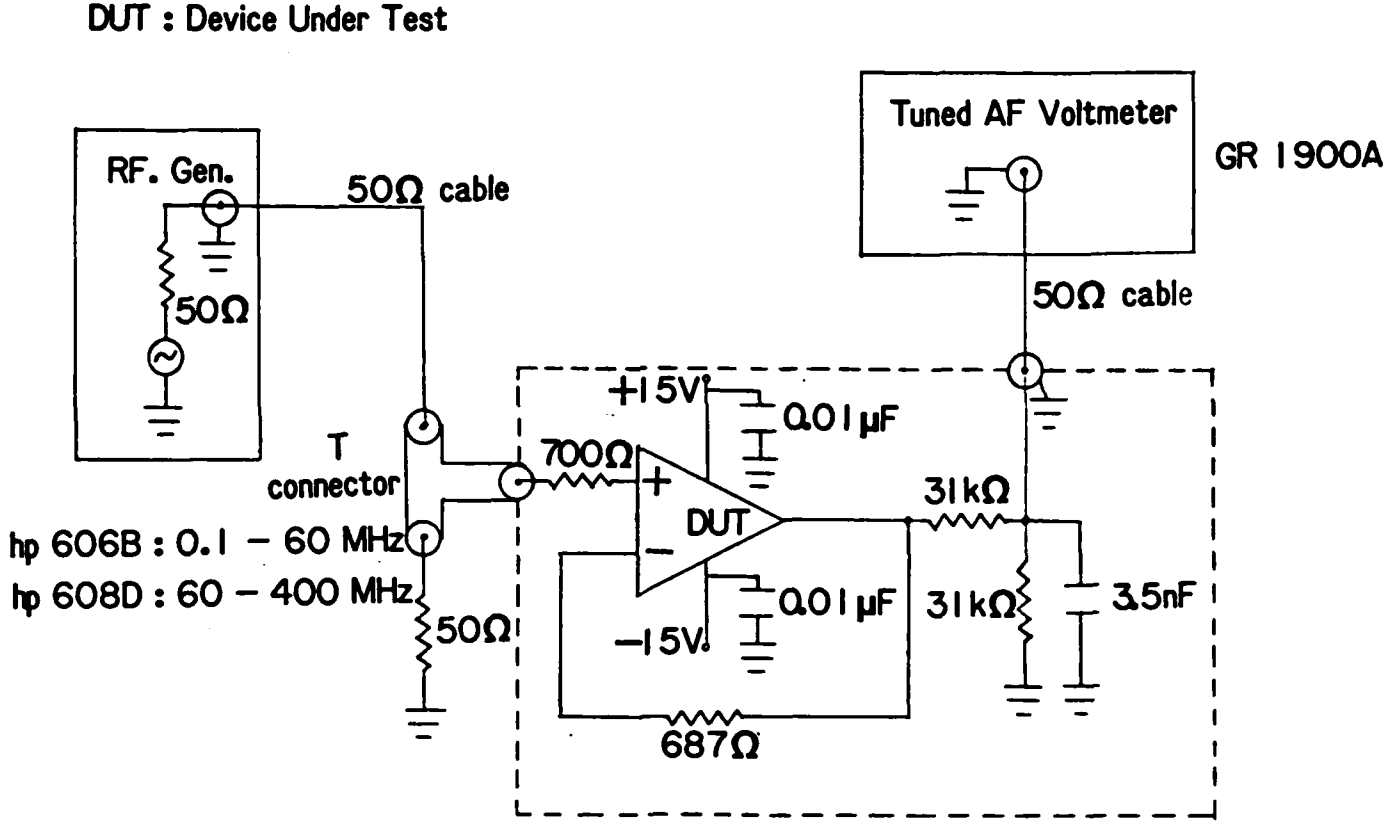

Fig. 4-7. Experimental set-up for demodulation RFI response measurement (after Fang). The 687 ohm resistor is often replaced by a short-circuit in voltage follower circuits of this type.

The voltage reading at the tuned AF voltmeter is a direct measure of the demodulation RFI response which can be characterized by the second-order-transfer function $H_2(-f_c,f_c)$ of the circuit under consideration. An expression from which $H_2(-f_c,f_c)$ values can be determined from the tuned AF voltmeter readings has been derived in Chapter 2. Using Eq. (2.3-36), the amplitude of the intermodulation signal at frequency f_m is given by

$$V_m = mA^2 \quad |H_2(-f_c,f_c)| \tag{4-3}$$

The AF voltmeter indicates the rms voltage of the AF signal. If we denote this rms voltage by V_M, then

$$V_M = 0.707mA^2 \quad |H_2(-f_c,f_c)| \tag{4-4}$$

Equation (4-4) can be expressed in dB with respect to a 1 mV reference level.

$$\begin{aligned} 20\cdot\log_{10}|V_M/1mV| &= 20\cdot\log_{10}[0.707mA^2|H_2(-f_c,f_c)|] - 20\cdot\log_{10}(10^{-3}) \\ &= 57 + 20\cdot\log_{10}(m) + 40\cdot\log_{10}(A) \\ &\quad + 20\cdot\log_{10}|H_2(-f_c,f_c)| \end{aligned} \tag{4-5}$$

The amplitude of the RF carrier voltage A can be given in terms of the generator available power P_{gen} which by definition is the power the generator would deliver to a load $R_i = R_g$ where R_g is the generator internal impedance. Using the equivalent circuit of Figure 4-8 with $R_i = R_g$, we obtain the relationship

$$P_{gen} = \frac{V_i^2}{R_i} = \frac{A^2}{8R_g} \tag{4-6}$$

Note that V_i is an rms voltage, but that A is an amplitude. If $R_i = R_g = 50\ \Omega$, Equation (4-5) can be expressed in terms of dBm as

$$P_{gen}(dBm) = 10 \cdot \log_{10}((A^2/400)/10^{-3}) = 4 + 20 \cdot \log_{10}(A) \tag{4-7}$$

With m = 0.5, Equation (4-4) can be written as

$$20 \cdot \log_{10}|V_M/1mV| = 2P_{gen}(dBm) + 43 + 20 \cdot \log_{10}|H_2(-f_c, f_c)| \tag{4-8}$$

Thus, we have an expression relating $H_2(-f_c, f_c)$ values and the tuned AF voltmeter readings. Besides, Equation (4-8) also suggests a convenient way of checking whether the AF voltmeter reading are caused by the second-order nonlinearities of the amplifier circuit under test. For every 1 dBm variation in P_{gen}, a corresponding 2 dB variation should be observed in the measured V_M value. We assume this condition when we use Equation (4-8) to calculate $H_2(-f_c, f_c)$. Figure 4-9 shows values of the measured AF voltmeter reading V_M in dBV versus the generator available power

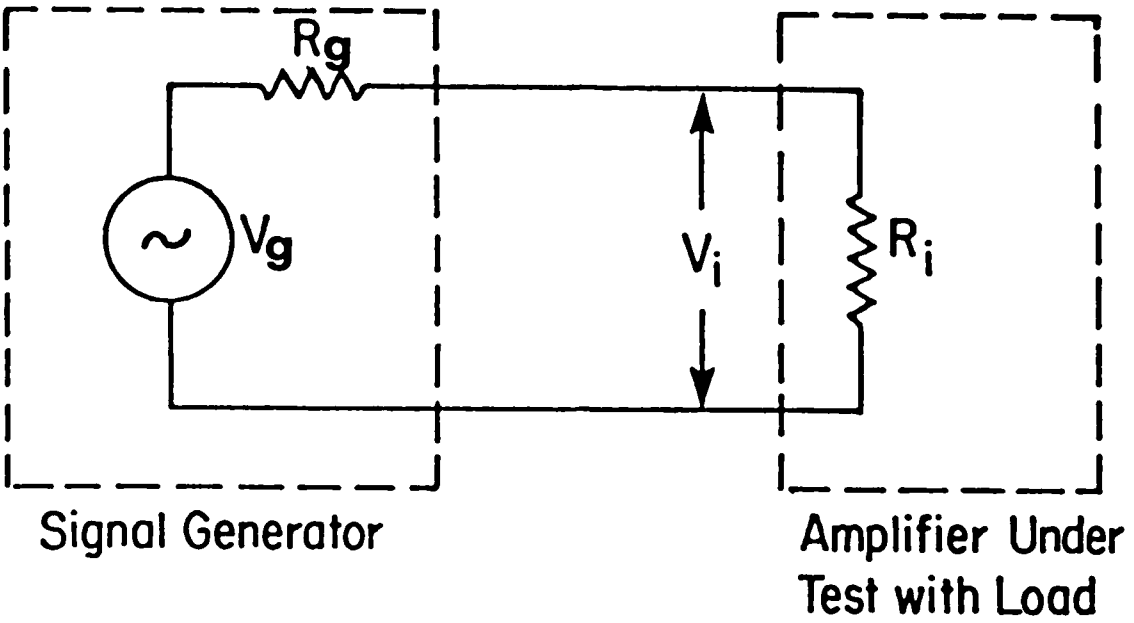

Fig. 4-8. Circuit used to relate the available power P_{gen} that the signal generator can deliver to a matched load $R_i = R_g$ to the signal generator voltage amplitude V_g.

P_{gen} for four types of op amps at f_c = 10 MHz. It is seen that for P_{gen} < 0 dBm, all four op amps have data plots that are straight lines with slopes equal to two in agreement with Equation (4-8). The region in which this behavior is observed is often called the square-law response region. For P_{gen} > 0 dBm, the slopes of the data curves start to deviate from two because of nonlinear terms of order higher than two. Whereas we cannot

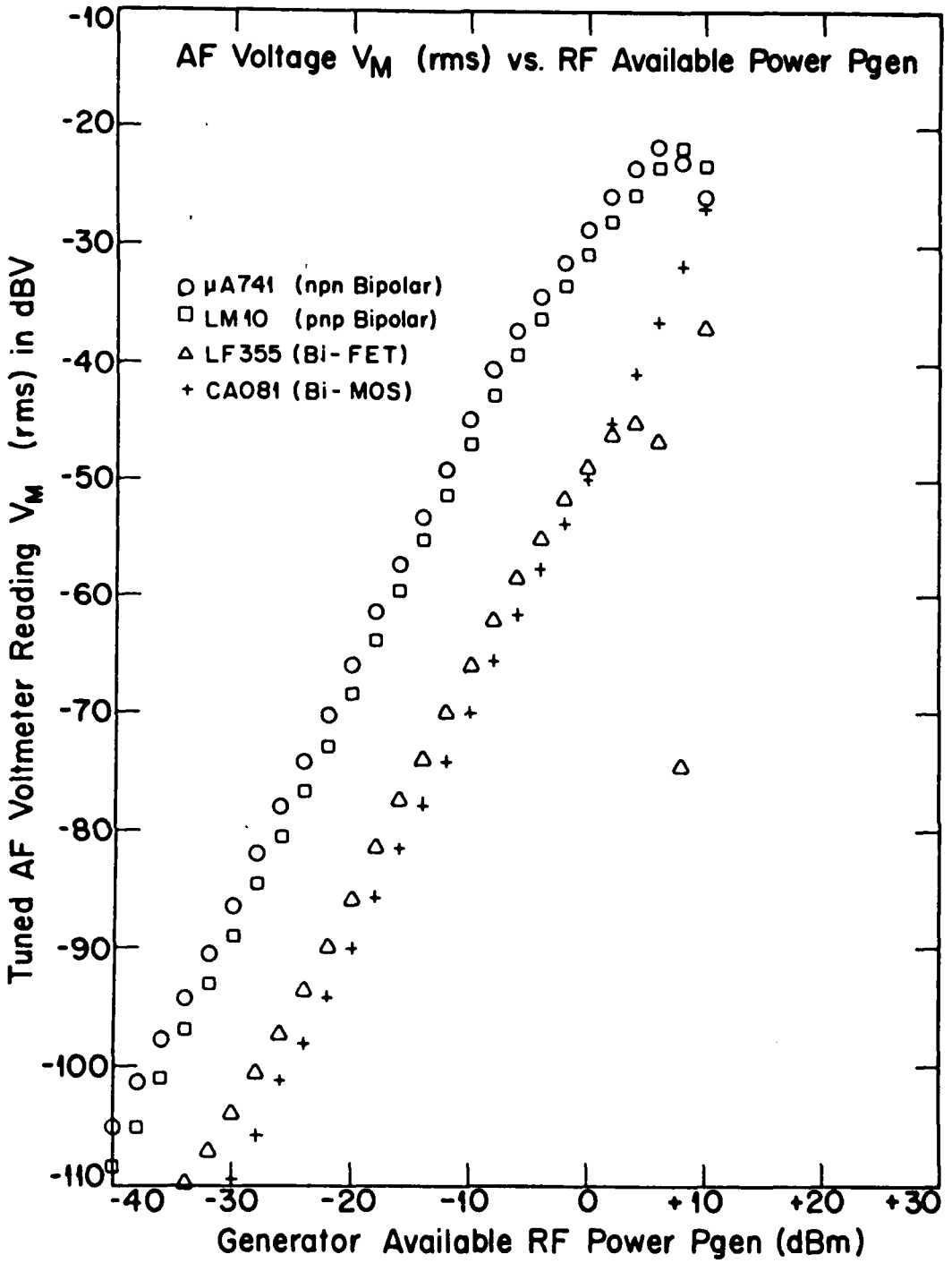

Fig. 4-9. Measured values of AF voltage V_M(rms) at the tuned AF voltmeter vs the generator available power P_{gen} for the unity gain buffer circuit for four types of op amps at one RF frequency:

$$f_m = 1kHZ,\ f_c = 10MHz,\ m = 0.5$$

set P_{gen} to values too large, it is also not appropriate to set it to values too low. We must not let the AF signal produced by second-order nonlinearities of the amplifier fall below the ambient noise level and become difficult to measure. Each curve shown in Figure 4-9 is used to obtain a $H_2(-f_c,f_c)$ value at one RF frequency. Values of $H_2(-f_c,f_c)$ at other RF frequencies may be obtained from plots similar to that shown in Figure 4-9. It is not necessary to measure as many data points as shown in Figure 4-9. Often, measurements were made at two values of P_{gen} such as -10 dBm and -20 dBm to verify the square-law response. Then the value of V_M(rms) at P_{gen} = -10 dBm was used to determine $H_2(-f_c,f_c)$.

4.3 Statistical Results for Unity Gain Buffer

As discussed in the previous section, the demodulation RFI in the square law response region can be characterized by the one parameter $H_2(-f_c,f_c)$. Shown in Figures 4-10 to 4-13 are values of $H_2(-f_c,f_c)$ for RF frequencies ranging from 0.1 to 400 MHz for the 115 op amps tested. In Figure 4-10 data for 30 741 op amps are presented. Among these 741 op amps, five were made by RCA in 1981 and the others were made by Fairchild during 1976 to 1982. The detailed information is listed in Table 4-2. The $H_2(-f_c,f_c)$ values at a specific RF frequency vary $\pm$ 1.5 to $\pm$ 11.5 dB. In Figure 4-11

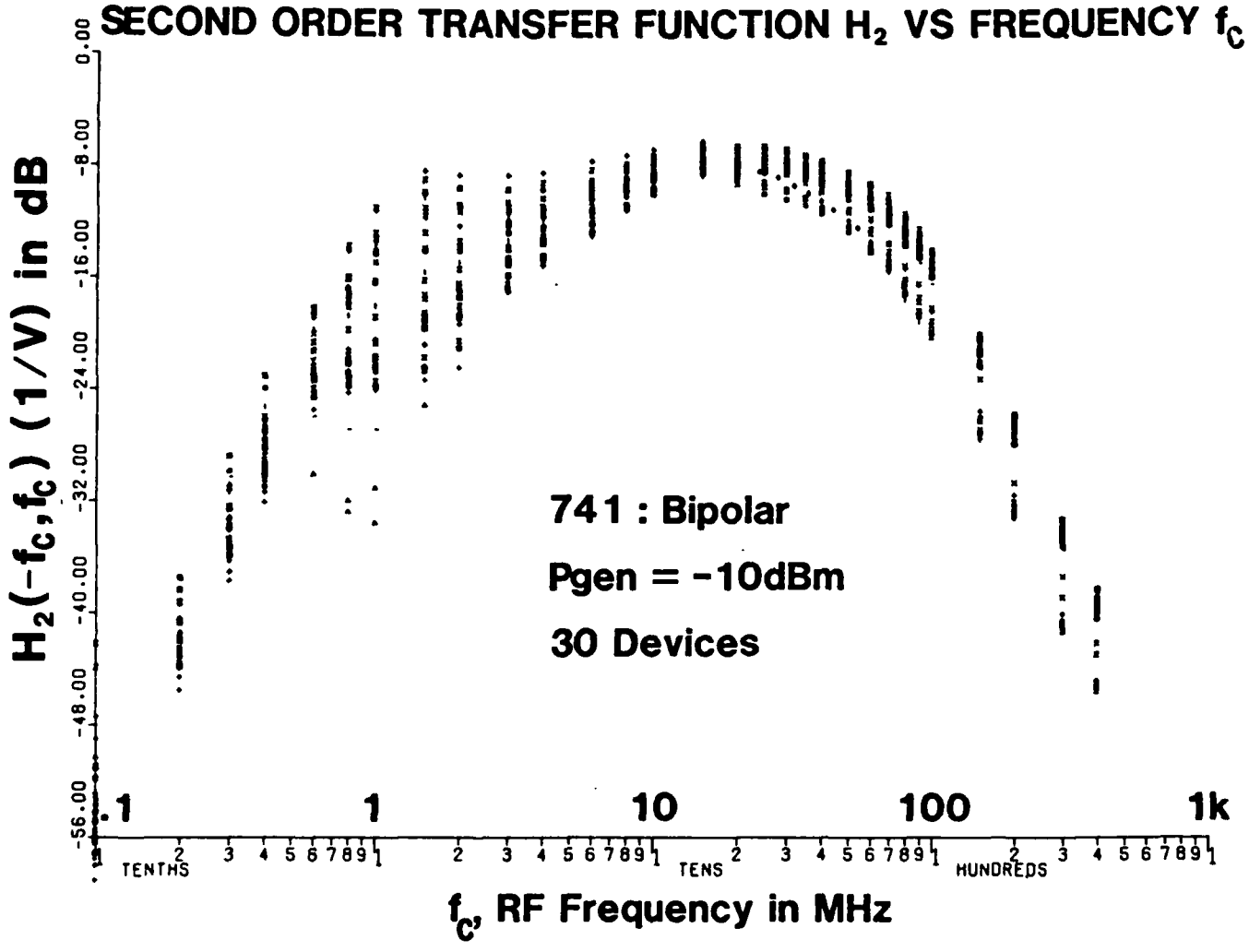

Fig. 4-10. Measured values of the second-order transfer function $H_2(-f_c,f_c)$ of the unity gain buffer circuit vs RF frequency for thirty 741 (bipolar) op amps.

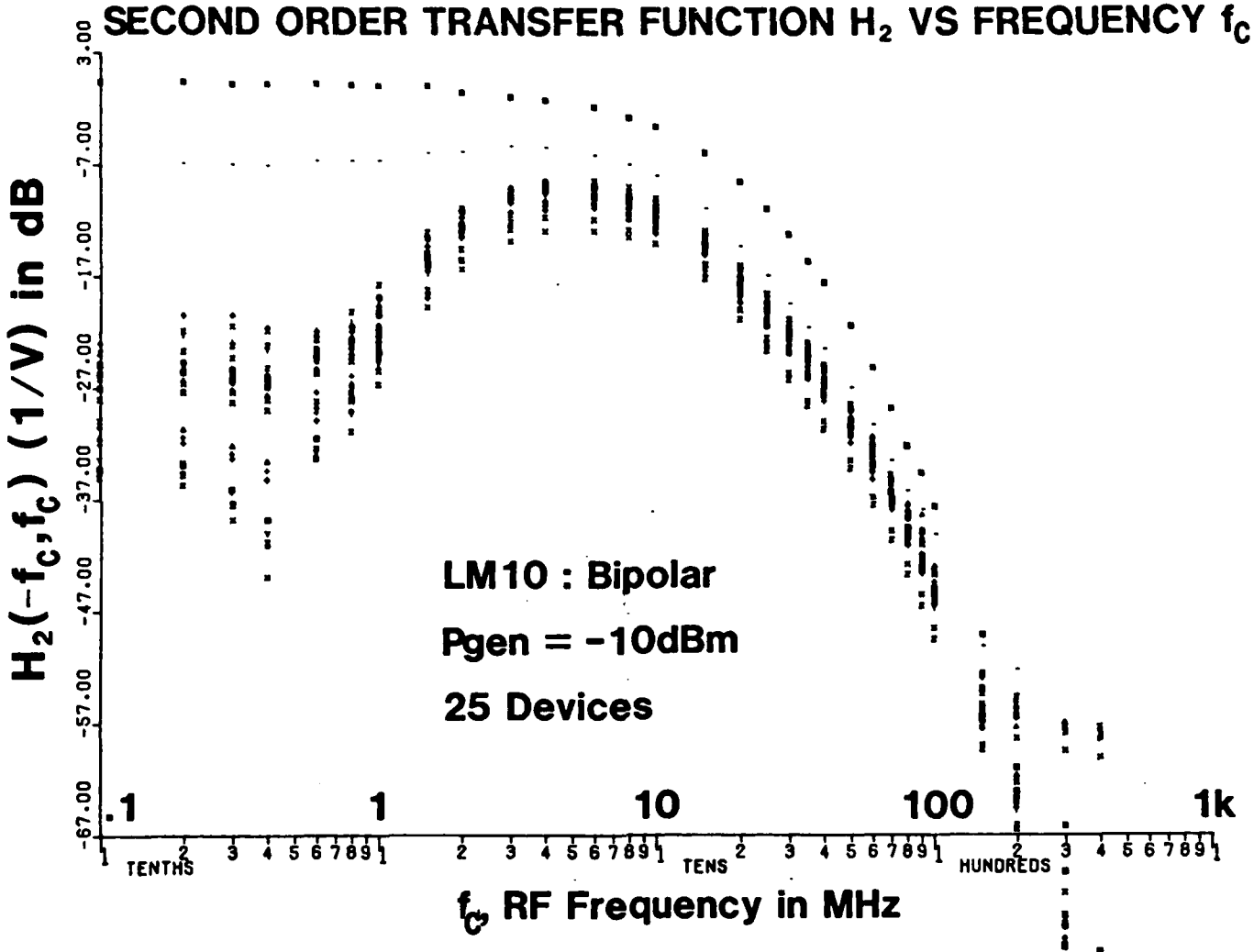

Fig. 4-11. Measured values of the second-order transfer function $H_2(-f_c,f_c)$ of the unity gain buffer circuit vs RF frequency for twenty-five LM10 (bipolar) op amps.

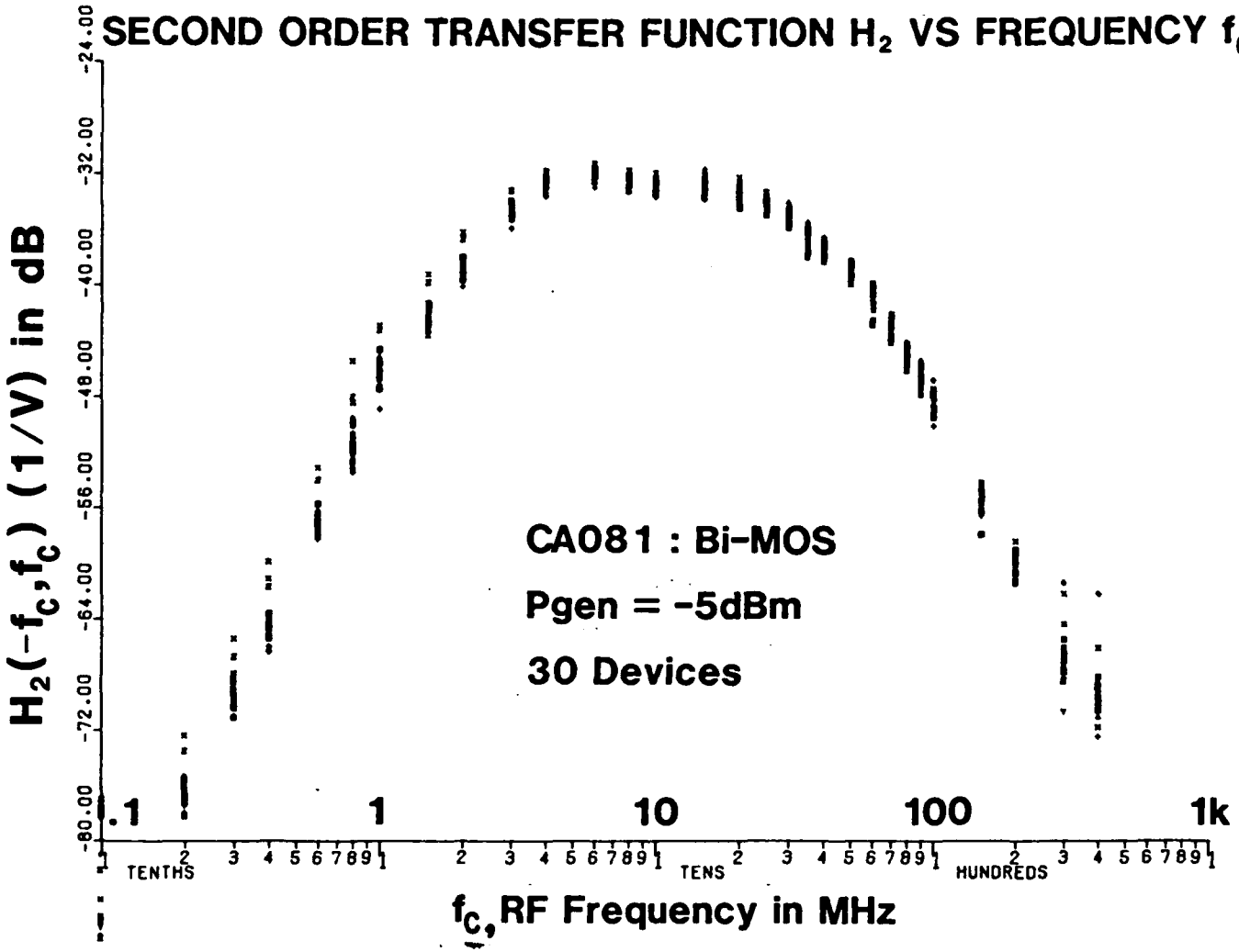

Fig. 4-12. Measured values of the second-order transfer function $H_2(-f_c,f_c)$ of the unity gain buffer circuit vs RF frequency for thirty CA081 (Bi-MOS) op amps.

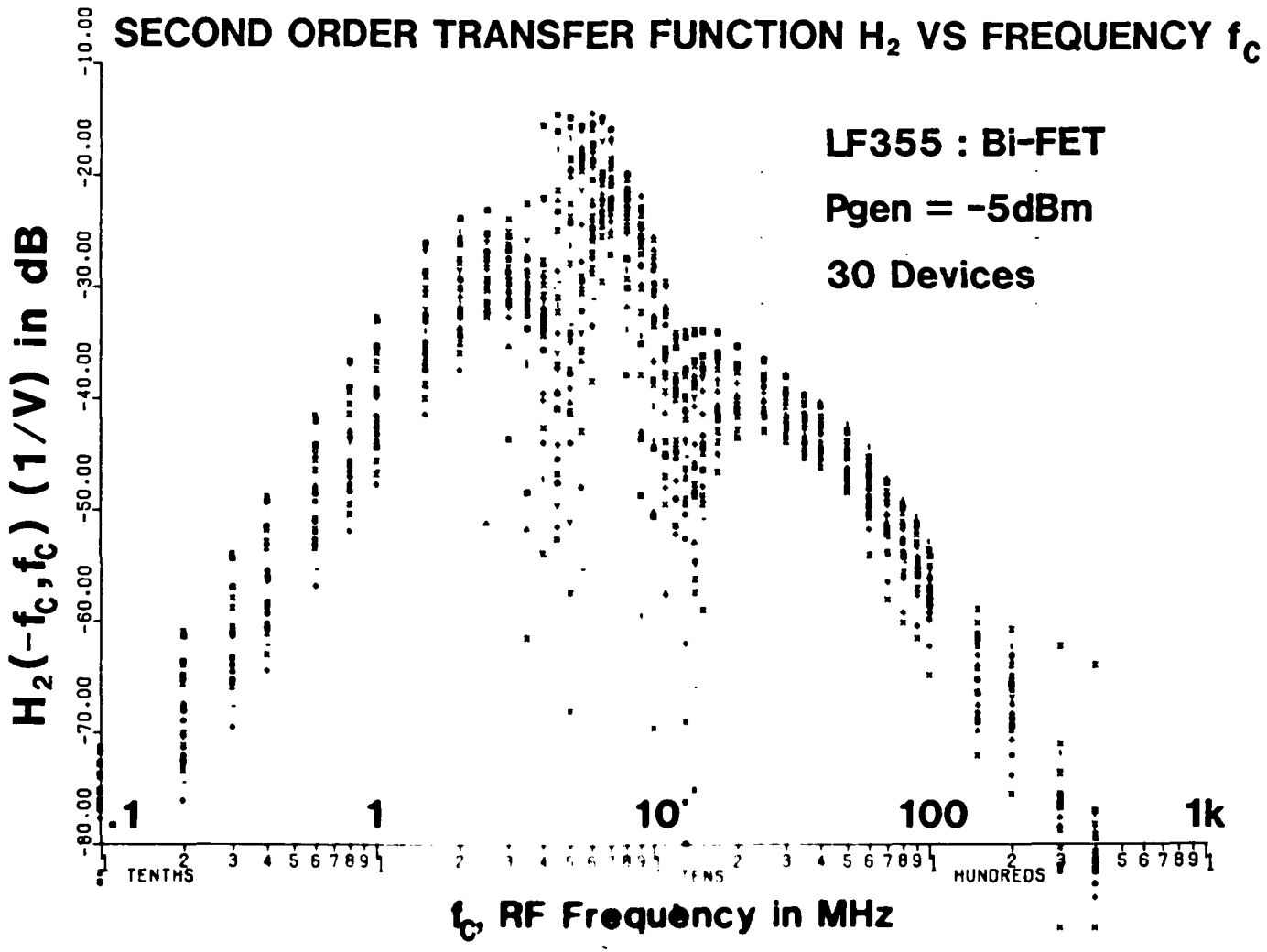

Fig. 4-13. Measured values of the second-order transfer function $H_2(-f_c,f_c)$ of the unity gain buffer circuit vs RF frequency for [illegible] op amps.

data for 25 LM10 op amps are presented. All 25 op amps were made during 1981 and 1982 by National Semiconductor. The most interesting aspect of the LM10 data is that two LM10 units (called mavericks) have $H_2(-f_c,f_c)$ values very different from the other LM10 units. It should be noted that one maverick LM10 op amp has a normal linear response as shown in Figure 4-18 of Ref. [2]. Its voltage gain vs frequency response appeared to be similar to the other 23 LM10 op amps. Since the maverick LM10 might perform as expected in some circuits, its data can not really be excluded from our statistical calculations. The 23 similar LM10 op amps have $H_2(-f_c,f_c)$ values varying $\pm$ 3 to $\pm$ 12 dB at any one RF frequency. In Figure 4-12 data for 30 CA081 op amps are presented. All 30 units were made by RCA during 1980. The $H_2(-f_c,f_c)$ values vary $\pm$ 1 to $\pm$ 5 dB at any one RF frequency. In Figure 4-13 data for 30 LF355 op amps are presented. All 30 units were made by National Semiconductor during 1980 to 1982. The most interesting aspects of the LF355 data are the resonances near 4.5 MHz and 12 MHz where the $H_2(-f_c,f_c)$ values decrease as much as 25 dB and 15 dB, respectively. The cause of the resonances has been investigated by computer-aided analysis of the circuit with the LF355 op amp replaced by its macromodel as described in Ref. [2]. The $H_2(-f_c,f_c)$ values outside the resonance regions vary from $\pm$ 3 dB to $\pm$ 8 dB at any one RF frequency.

Shown in Figures 4-14 and 4-15 are the mean values for $H_2(-f_c, f_c)$ which are denoted by $\overline{H}_2$ and the standard deviation σ for the four types of op amps tested. Values for $\overline{H}_2$ and σ were calculated using the data for all the op amps given in Figures 4-10 to 4-13.

The mean values for $H_2(-f_c, f_c)$ indicate clearly that demodulation RFI effects are greater in op amps with bipolar input transistors (741 and LM10) than they are in op amps with FET input transistors (CA081 and LF355). This is a most important observation. At RF frequencies above 10 MHz, demodulation RFI effects in the 741 op amp are significantly greater than in the LM10 op amp. It is believed that this is a result of the cutoff frequency of the npn bipolar input transistors in the 741 op amp being higher than the cutoff frequency of the pnp bipolar input transistors in the LM10 op amp. It is also noted that the mean value $\overline{H}_2$ for the LF355 op amp shows much less resonant excursion than do individual units. This is a result of the spread in values for the resonant frequencies which causes a smoothing effect for $\overline{H}_2$. For RF frequencies less than 10 MHz, the mean value $\overline{H}_2$ is lowest for the CA081 op amps (MOSFET input transistors). For RF frequencies greater than 10 MHz, the mean value $\overline{H}_2$ is lowest for the LF355 op amps (JFET input transistors).

The values for the standard deviation σ vs RF frequency are shown in Figure 4-15. It is noted that for the CA081 op amps, the σ values are less than 2 dB except at 0.1 MHz where $\overline{H}_2$ is very small. For the LM10 op amps, the σ values were calculated both for all op amps and also for the normal op amps only.

$$\text{Standard Deviation} = \sigma = [(\Sigma(x - \mu)^2) \div n]^{.5}$$

where n = total number of items,

x = item value,

μ = mean value of all items.

Omitting the $H_2(-f_c, f_c)$ values for the two maverick LM10 op amps decreased σ by approximately 2 to 4 dB below 2 MHz and by approximately 1 dB or less above 2 MHz. The σ values shown in Figure 4-15 are the values calculated for all 25 op amps. For the LF355 op amps, the σ values are large especially in resonant regions near 4.5 MHz and 12 MHz. The σ values are also large above 200 MHz where the $H_2(-f_c, f_c)$ values are small.

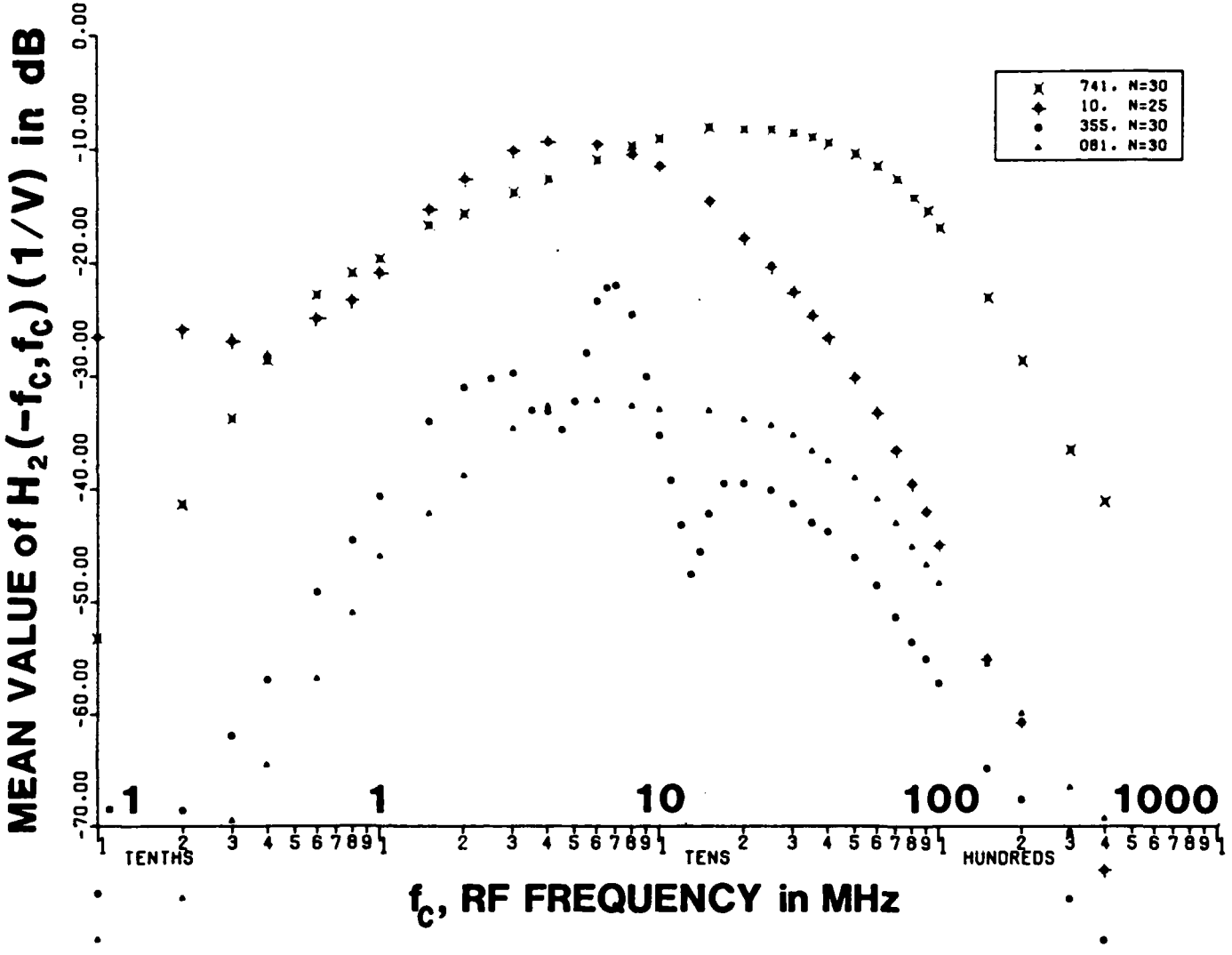

Fig. 4-14. Experimental mean value of the second-order transfer function $H_2(-f_c,f_c)$ of the unity gain buffer circuit vs RF frequency for four types of op amps.

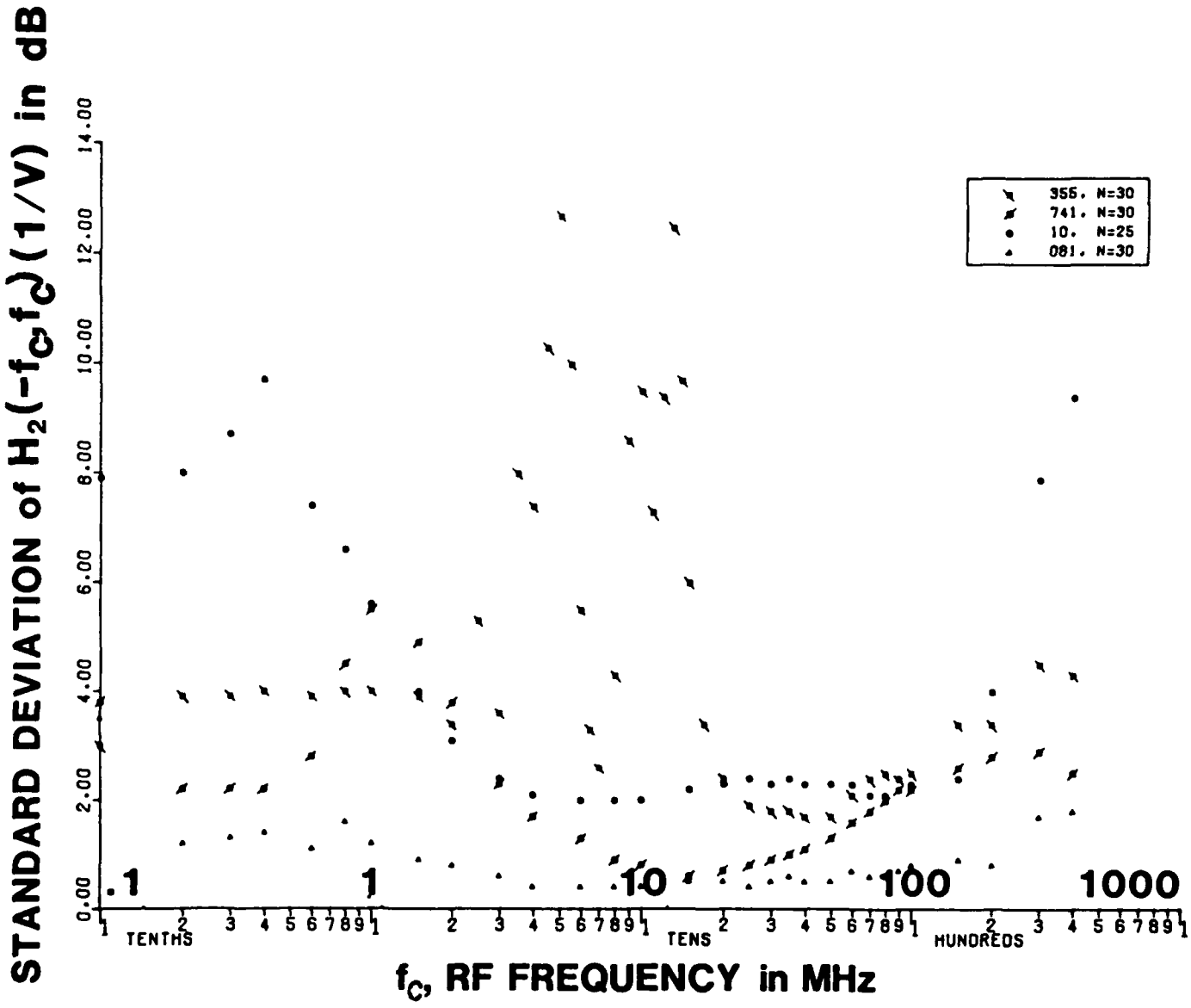

Fig. 4-15. Experimental standard deviation, σ, of the second-order transfer function $H_2(-f_c, f_c)$ of the unity gain buffer circuit vs RF frequency for four types of op amps.

4.4 The 3-Stage Op Amp LED Circuit and Its Linear Response

We have presented results for the unity voltage gain buffer amplifier circuit which is often called a voltage follower. That circuit configuration is noninverting because the intended signal is injected into the noninverting input denoted by (+). The RFI signal was also injected into the noninverting input. In this section, we report the results of an investigation of the inverting op amp configuration shown in Figure 4-16. The intended signal voltage gain is $A_v = V_{OUT}/V_{IN} = -R2/R1$ and the intended signal input impedance is R1. The capacitance C4 in the feedback path, when included, provides RFI suppression [23]. An experimental configuration similar to that shown in Figure 4-6 was used to measure demodulation RFI for RF frequqncies in the range 100 kHz to 400 MHz. Measurement results will be presented for R1 = 10 kΩ and R2 = 100 kΩ for C4 = 0 pF and C4 = 27 pF for 35 units of 741 op amps. Thirty units are identical to those listed in Table 4-2; the five additional 741 op amps were made by National Semiconductor in 1982.

The actual circuit used in the measurement of demodulation RFI effects in inverting op amp circuits is shown in Figure 4-17. This circuit will be referred to as the 3-stage op amp LED circuit hereafter. The 3-stage op amp LED circuit was designed to corre-

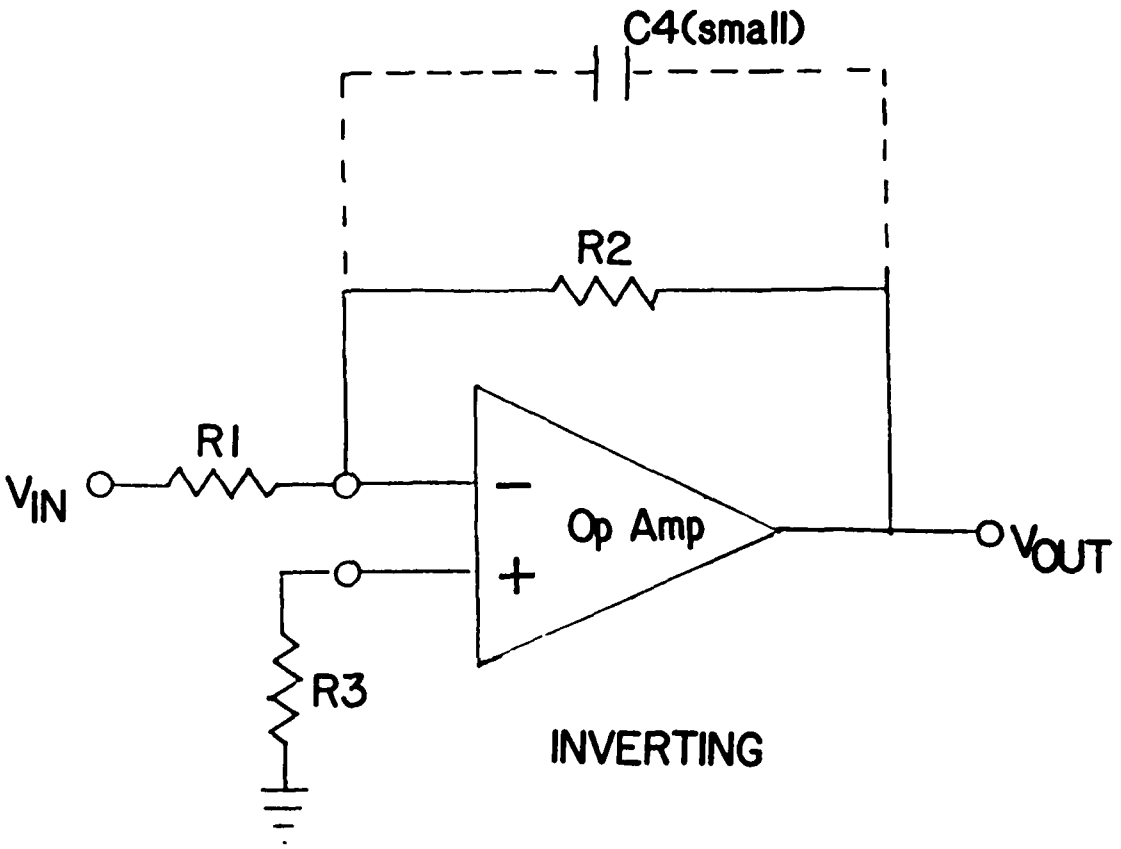

Fig. 4-16. Inverting op amp circuit with voltage gain A_v = -R2/R1. The capacitor C4, when included, provides RFI suppression.

spond to a circuit in a warning light system. In a warning light system, a tranducer generates a signal which must be amplified sufficiently in order to turn on a warning light such as an LED (Light Emitting Diode). The RFI signal is injected into the inverting input of the 1st stage. The RFI signal is an AM-modulated RF signal. Because of nonlinearities which exist in analog circuits called linear amplifiers, a demodulated RFI response at the AM modulation frequency is generated within the 1st op amp stage. The demodulated

RFI signal produced in the 1st stage is amplified by the 2nd stage and by the third stage which drives the Light-Emitting Diode. The amplified demodulated RFI signal can light the LED to produce a visual display of the existence of RFI. The EMI experiment was designed to demonstrate how two sets of statistics from two independent experiments can be combined to predict the statistics of a combined experiment. One experiment (See Chapter 3) provided statistics on cable coupling for wires terminated in resistive loads. The experiment described in this section and in the following section provided second-order transfer function statistics for the 3-stage op amp LED circuit. The goal was to combine the two sets of independent statistics and to compare to the statistics of the combined experiment. The second-order transfer function of the inverting op amp configuration of Figure 4-16 can be related to the second-order transfer function of the 3-stage op amp LED circuit by accounting for the linear voltage gains of the second and third stage and the attentuation of the circuit between the RF generator and input of the 1st stage.

This paragraph will describe the function of each element in the circuit of Figure 4-17. The RF signal generator produces an RF voltage with an RF carrier frequency f_c in the range 0.1 to 400 MHz. The RF voltage is AM-modulated with modulation index $m = 0.5$ and AM-modulation frequency $f_m = 1$ kHz. The capacitors

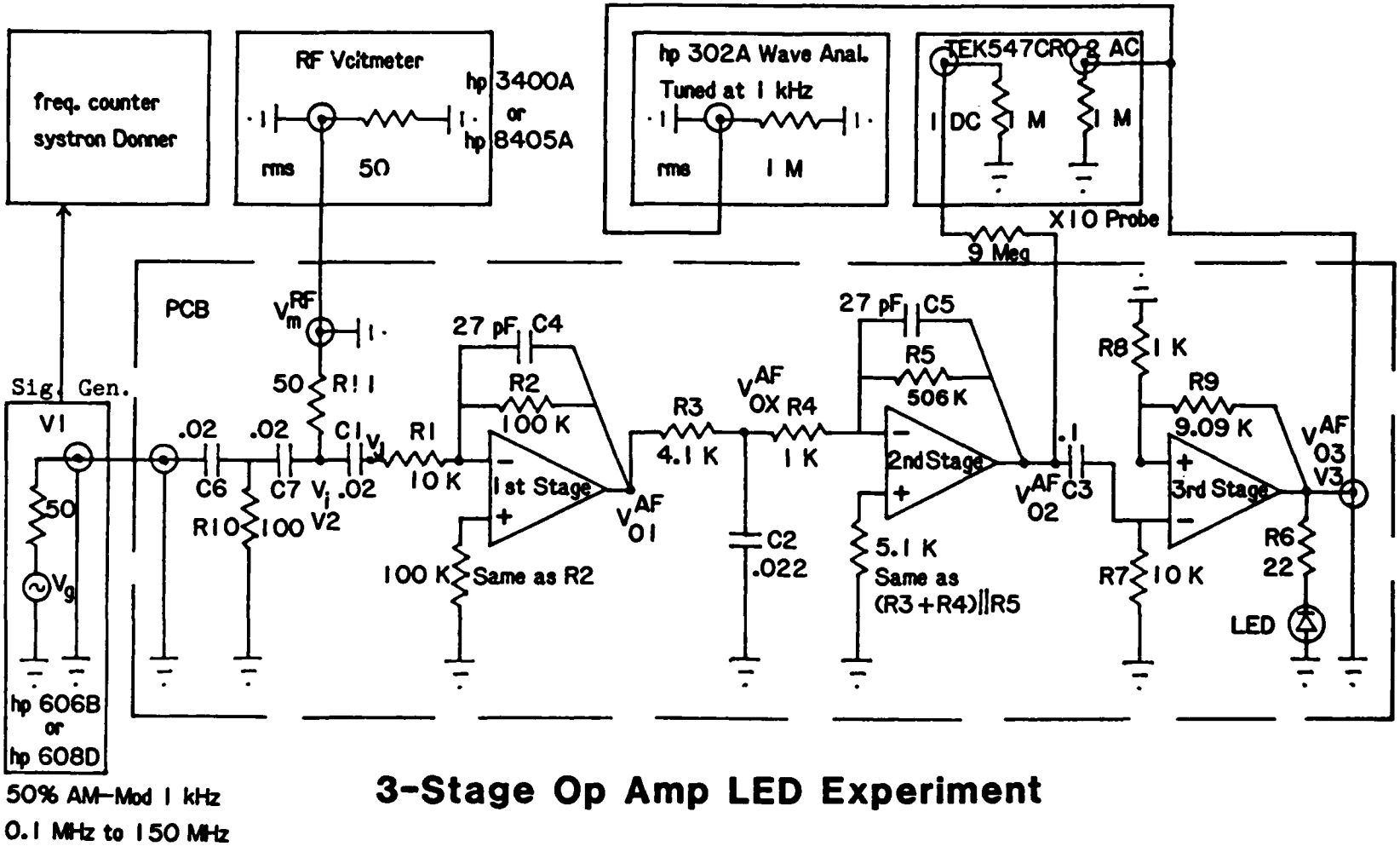

3-Stage Op Amp LED Experiment

Fig. 4-17. Three-stage op amp LED experiment. Resistor values are in Ω. Capacitor values are in μF unless otherwise specified.

C6, C7, and C1 and resistors R10, R11, and the 50 Ω input resistor of the RF voltmeter form a high-pass RC filter which blocks dc and any spurious 1 kHz components from the RF generator. The first stage is the op amp under test; it has an inverting configuration. Its second-order nonlinearities cause an undesired demodulation of the amplitude-modulated RF signal to produce an undesired audio modulation frequency component V_{01}^{AF} at the output of the first stage. The ratio of the feedback resistor R2 to the input resistor R1 provides the intended linear voltage gain A_{v1} of the first stage at low frequencies. The capacitor C4, when included, serves as an RFI suppression capacitor [23]. The RF voltmeter reads the rms RF voltage V_m^{RF} which is one-half the rms RF voltage V_i at the input of the first stage. Note that a 50 Ω resistor is used to terminate the 50 Ω coaxial cable connecting the circuit and the RF voltmeter. Furthermore, the resistor combination of R10 in parallel with the series combination R11 + the 50 Ω termination resistor at the RF voltmeter input provides at high frequencies a 50 Ω terminating resistance to the 50 Ω coaxial cable connecting the RF generator and the circuit. Between the first and second stages there is a low-pass filter formed by R3, R4, and C2. It attenuates any RF components from the first stage, but it allows the audio frequency component V_{01}^{AF} to pass through. The second and third stages provide linear voltage amplification of the audio-fre-

quency component V_{01}^{AF}. The second stage is an inverting amplifier with a voltage gain of 100 determined by the ratio R5/(R3 + R4). It is critical to include a resistor equal in value to the feedback resistor R2 from the noninverting input of the first stage to ground. That resistor reduces the dc offset voltage at the output of the first stage. The first stage dc offset voltage will be amplified in the second stage and can cause saturation at the output of the second stage. The resistor connecting the noninverting input of the second stage to ground serves a similar purpose, but it is less critical. The capacitor C3 and resistor R7 form a high-pass filter with a 160 Hz cutoff frequency to block any remaining dc offsets at the output of the second stage from entering the 3rd stage. The third stage is a noninverting amplifier with a voltage gain of 10 determined by the ratio (R8 + R9)/R8. The LED goes on when the rms voltage of the amplifier demodulated audio frequency components V_{03}^{AF} at the output of the 3rd stage exceeds a threshold value. The threshold value for a purely 1 kHz signal was typically 1.1 V (rms) which corresponds to a peak voltage of 1.5 V. There were occasions when the LED went on and the 1 kHz voltage component was much less than 1.1 V (rms). In these cases a strong 2 kHz voltage component was observed. A 2 kHz voltage component can also be a second-order demodulation RFI component. It results from a beating or mixing (intermodulation) of the upper and lower sidebands of the

AM-modulated RF input signal in the 1st op amp stage. Usually, the 2 kHz RFI component was in the range 0.15 ± 0.005 V (rms) when the 1 kHz RFI component was 1.0 V (rms). However, when a resonant effect was observed which caused the 1 kHz voltage component to be suppressed, the RF voltage has to be increased to an unusually high level in order to turn on the LED. Then a strong 2 kHz voltage component was observed. The 2 kHz voltage component might be as large as the 1 kHz voltage component. Occasionally, the 2 kHz voltage component exceeded the 1 kHz voltage component. We suspect that these circumstances indicated that a 4th-order nonlinear effect may have manifested itself.

A frequency counter was used to measure accurately the RF frequency. A cathode ray oscilloscope (CRO) was used to monitor the dc offset voltage and the AF voltage waveform at the output of the second stage.

Prior to the measurement of demodulation RFI responses, the linear voltage gain at audio frequency 1 kHz of the entire 3-stage op amp LED assembly and of each section was measured to verify the circuit connections. An Audio Frequency (AF) oscillator (hp651B) was connected in place of the RF voltmeter to apply an AF signal to the circuit while the RF generator was turned off. The AF voltages V_{03}^{AF}, V_{02}^{AF}, V_{0X}^{AF}, V_{01}^{AF}, V_{j}^{Af}, and V_{i}^{AF} which are shown in Figure 4-17 were read with a tuned AF wave analyzer (hp302A). The super-

script AF denotes Audio Frequency component. The AF voltage V_{03}^{AF} at the output of the 3rd stage was set at 1.0 V (rms) while readings of other AF voltages were taken. The results are given in Table 4-3. The V_{0X}^{AF} reading drew our attention. When the op amp used in the 2nd stage was a 741 op amp, the voltage V_{0X}^{AF} was 0.25 mV instead of the expected 0.2 mV. When the 741 op amp was replaced with a LF355 op amp, the voltage V_{0X}^{AF} was 0.2 mV in agreement with what we expected. We believe that the discrepancy in the V_{0X}^{AF} value when a 741 op amp was used in the second stage is related to the low input impedance of the 741 op amp. Other AF voltages in Table 4-3 have values in satisfactory agreement with calculated values.

4.5 Measurement of Demodulation RFI Response of 3-Stage Op Amp LED Circuit

In all measurements of demodulation RFI responses, the op amps for the 2nd and 3rd stage of the 3-stage op amp LED circuit were the same (741-#20 and 741-#12 respectively). The 1st stage op amp was changed. Each of the 30 units of 741 op amps listed in Table 4-2 and the five additional 741 op amps made by National Semiconductor was used in the 1st stage. The signal from the RF generator was a 50% amplitude-modulated (1 kHz) RF signal as before. The input RF signal at a specific RF frequency was adjusted so that the demodulated 1 kHz AF component at output V3 of the 3rd stage reached rms values of V_{03}^{AF} = 1.0 V and 0.4 V sequentially. At the same time, the meter readings of the RF generator and RF voltmeter were recorded. This

TABLE 4-3

LINEAR AF NODE VOLTAGES AT 1 KHZ OF THE 3-STAGE OP AMP LED CIRCUIT

AF Voltage	hp 302A Reading[a]	Expected Value
V_{03}^{AF} (V)	1.0	1.0
V_{02}^{AF} (mV)	102	100
V_{0X}^{AF} (mV)	0.25[b]	0.20
V_{01}^{AF} (mV)	0.98	1.0
V_{j}^{AF} (μV)	98	100
V_{i}^{AF} (μV)	115	$\geq$ 100

[a] All readings are in rms values. The 741 op amps were used in all 3 stages (1st: 741-#1, 2nd: 741-#20, 3rd: 741-#12).

[b] When a LF355 was used in 2nd stage, the reading was 0.2 mV.

procedure was used to verify the square law response region described in Section 4.2. To understand this, note that the two AF voltages (1.0 V and 0.4 V) at output V3 corresponds to a ratio of -8 dB. Therefore, the two corresponding meter readings of the RF voltmeter or RF generator should give a ratio of approximately -4 dB. If otherwise, the data taken do not reflect the characteristics of second-order nonlinearities and should be rejected for use in determining H_2. If the data correspond to the square law response region, the second-order transfer function can be determined from the data.

The 1 kHz AF rms voltage V_{03}^{AF} at the output is related to the RF rms voltage V_g^{RF} from the RF generator by the second-order transfer function $H_2(-f_c,f_c)$.

$$\sqrt{2}\,V_{03}^{AF} = m(\sqrt{2}\,V_g^{RF})^2 \cdot |H_2(-f_c,f_c)| \qquad (4\text{-}9)$$

where m is the modulation index. The factor $\sqrt{2}$ arises because amplitudes are used in nonlinear transfer function expressions. From Figure 4-17, we note the voltage relationship given by

$$V_g^{RF} = 4V_m^{RF} \qquad (4\text{-}10)$$

Substitute Eq. (4-9) into Eq. (4-10) and solve for $H_2(-f_c,f_c)$ with m = 0.5. The result is

$$|H_2(-f_c,f_c)| = \sqrt{2}\,V_{03}^{AF}/(4V_m^{RF})^2 \qquad (4\text{-}11)$$

where V_{03}^{AF} and V_m^{RF} are in rms volts. Equation (4-11) can be expressed in dB as

$$20\log_{10}|H_2(-f_c,f_c)| = 20\log_{10}V_{03}^{AF} - 40\log_{10}V_m^{RF} - 21.0 \qquad (4\text{-}12)$$

The second-order transfer function H_2' of the 1st stage alone, i.e., between the output node of the 1st stage and the node connecting C1 and R1, can be related to the second-order transfer function H_2 of the complete circuit. Accounting for the linear gains of the 2nd stage (100) and the 3rd stage (10) and the attenuation factor (0.5) of the input attenuator, we obtain the results

$$|H_2'(-f_c,f_c)| = |H_2(-f_c,f_c)|(2)^2/(100 \cdot 10) = |H_2(-f_c,f_c)|/250 \quad (4\text{-}13)$$

or $$20\log_{10}|H_2'(-f_c,f_c)| = 20\log_{10}|H_2(-f_c,f_c)| - 48.0 \quad (4\text{-}14)$$

4.6 Statistical Results for 3-Stage Op Amp LED Circuit

As discussed previously, the demodulation RFI at 1 kHz in the square law response region can be characterized by the one parameter $H_2(-f_c,f_c)$. Shown in Figures 4-18 and 4-19 are measured values of $H_2(-f_c,f_c)$ of the 3-stage op amp LED circuit for RF frequencies in the range of 0.1 to 150 MHz for 35 units of 741 op amps tested. In Figure 4-18, the resistor and capacitor combinations are R1 = 10 kΩ, R2 = 100 kΩ, and C4 = C5 = 0. The $H_2(-f_c,f_c)$ values at a specific RF frequency vary $\pm$ 3 to $\pm$ 11 dB. In Figure 4-19, the resistor and capacitor combinations are R1 = 10 kΩ, R2 = 100 kΩ, and C4 = C5 = 27 pF. The $H_2(-f_c,f_c)$ values at a specific RF frequency vary $\pm$ 4 to $\pm$ 15 dB. Whereas H_2 values in Figures 4-18 and 4-19 are for the complete 3-stage op amp LED circuit, the H_2' values for the 1st stage alone can be obtained easily by subtracting 48 dB from H_2 values for the complete circuit. See Eq. (4-14). The value of the ordinate in Figures 4-18 and 4-19 is reduced by 48 dB. The variations of H_2' values in dB at a specific frequency are identical to those of H_2 values.

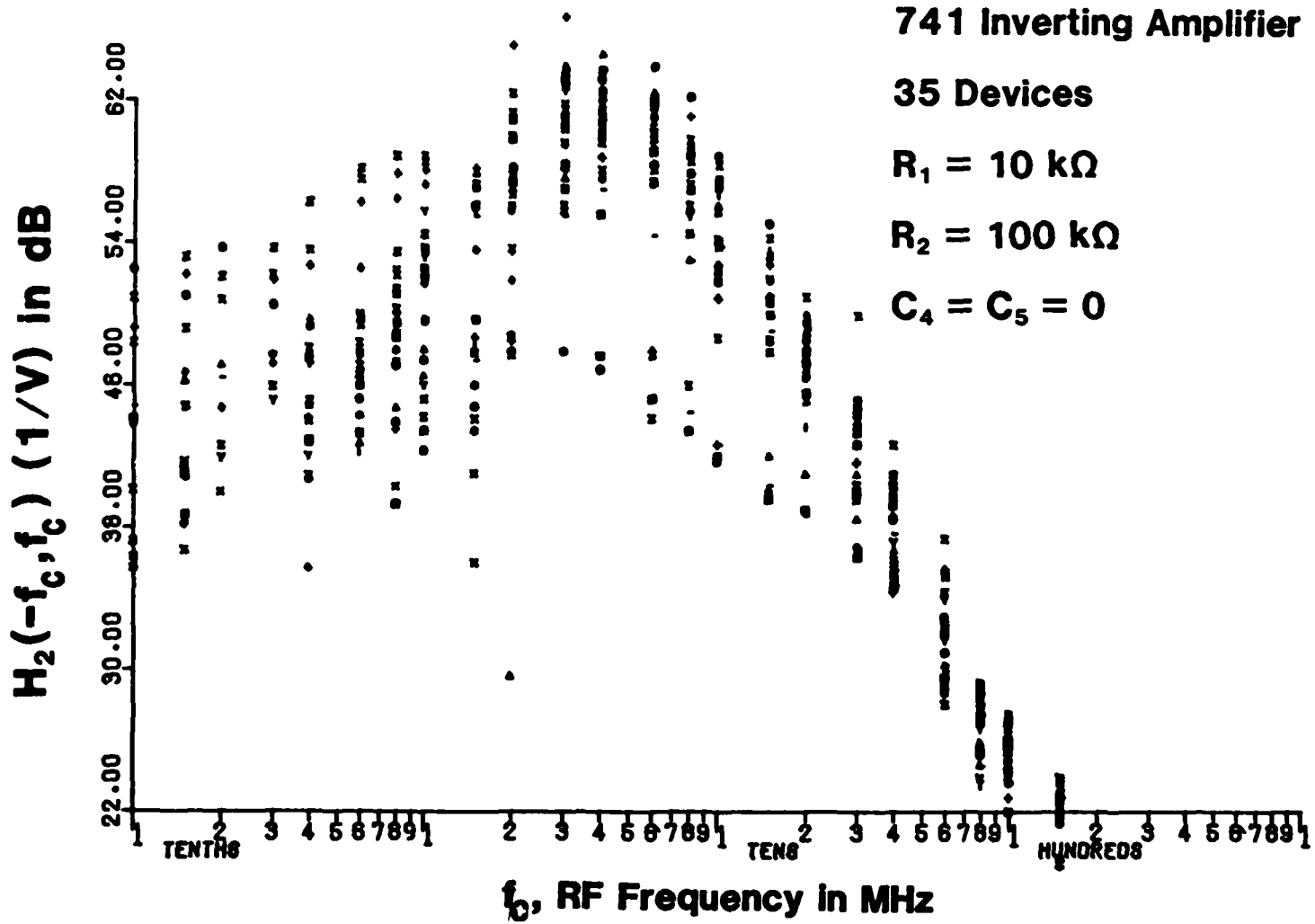

Fig. 4-18. Measured values of the second-order transfer function $H_2(-f_c, f_c)$ of the 3-stage op amp LED circuit vs RF frequency for 35 741 op amps. RFI suppression capacitor omitted.

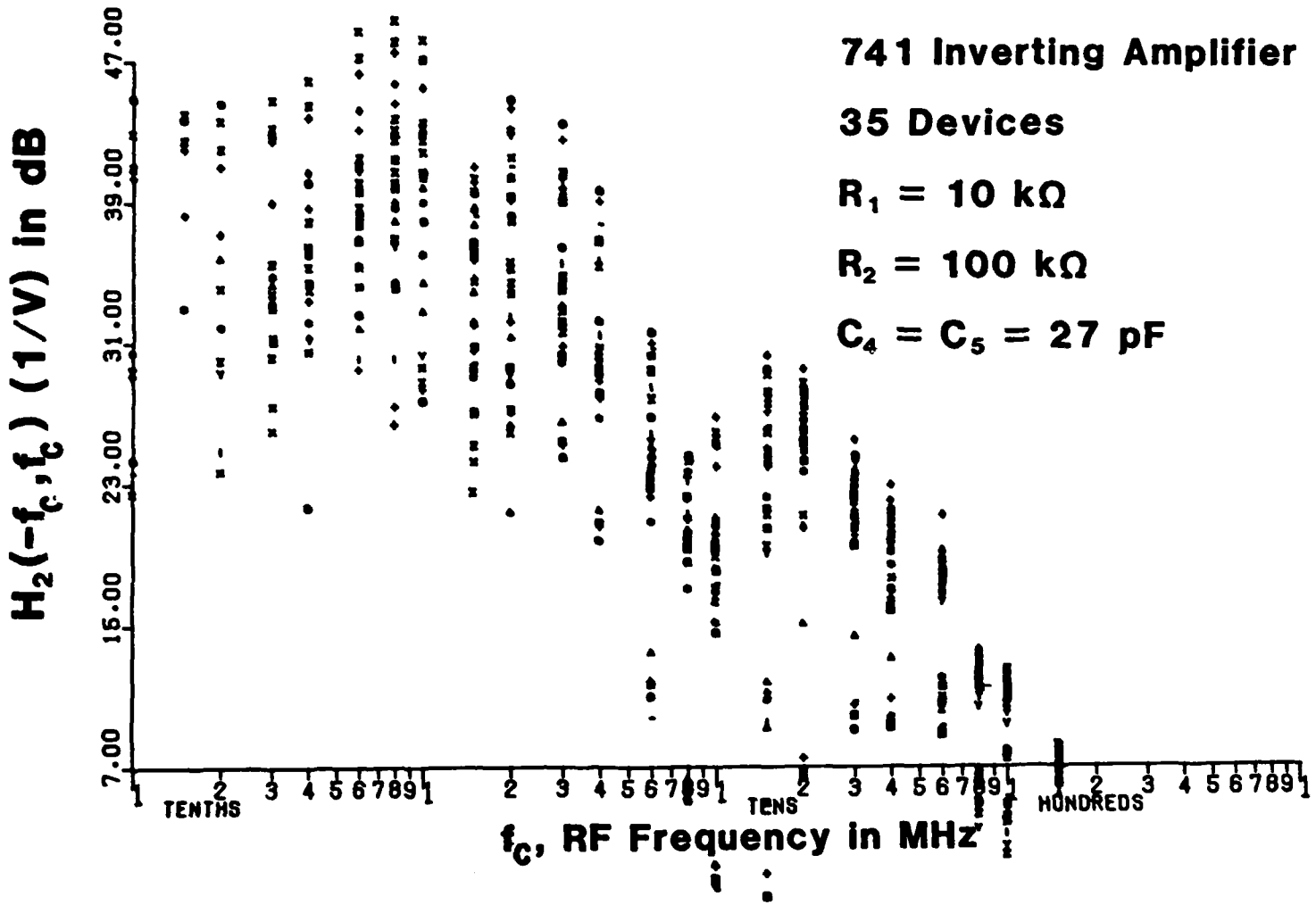

Fig. 4-19. Measured values of the second-order transfer function $H_2(-f_c, f_c)$ of the 3-stage op amp LED circuit vs RF frequency for 35 741 op amps. RFI suppression capacitor included.

Shown in Figures 4-20 and 4-21 are the mean values for $H_2(-f_c,f_c)$ which are denoted by $\bar{H}_2$ and the standard deviation σ for 35 units of 741 op amps tested in the 3-stage op amp LED circuit. One of the two sets of data in each figure corresponds to R1 = 10 kΩ, R2 = 100 kΩ, and C4 = C5 = 0. Another set corresponds to R1 = 10 kΩ, R2 = 100 kΩ, and C4 = C5 = 27 pF. The mean values for $H_2(-f_c,f_c)$ indicate clearly the effect of the RFI suppression capacitor C4 when it is connected in the feedback path of the 1st stage. The suppression of demodulation RFI effects caused by a 27 pF capacitor result in a reduction in $\bar{H}_2$ from 3.5 dB to as much as 36.5 dB at a specific RF frequency. Another effect of the RFI suppression capacitor C4 is indicated by the two sets of standard deviation data in Figure 4-21. That plot shows that the spreading of H_2 values is wider in general by including C4 = 27 pF. An increase as much as 5 dB in standard deviation is observed at certain RF frequencies.

In Figure 4-22, RFI demodulation responses in two 741 op amp circuits are shown. One set of data are mean values of measured H_2 for the 741 unity gain buffer. Another set of data are mean values of measured H_2 for the 741 inverting amplifier with a voltage gain of 10 and no RFI suppression capacitor (C4 = 0). For comparison purposes, the H_2 values for the 741 unity gain buffer from Figure 4-14 have to be adjusted. We want an H_2' for the unity gain buffer that relates the audio-frequency voltage at the op amp out-

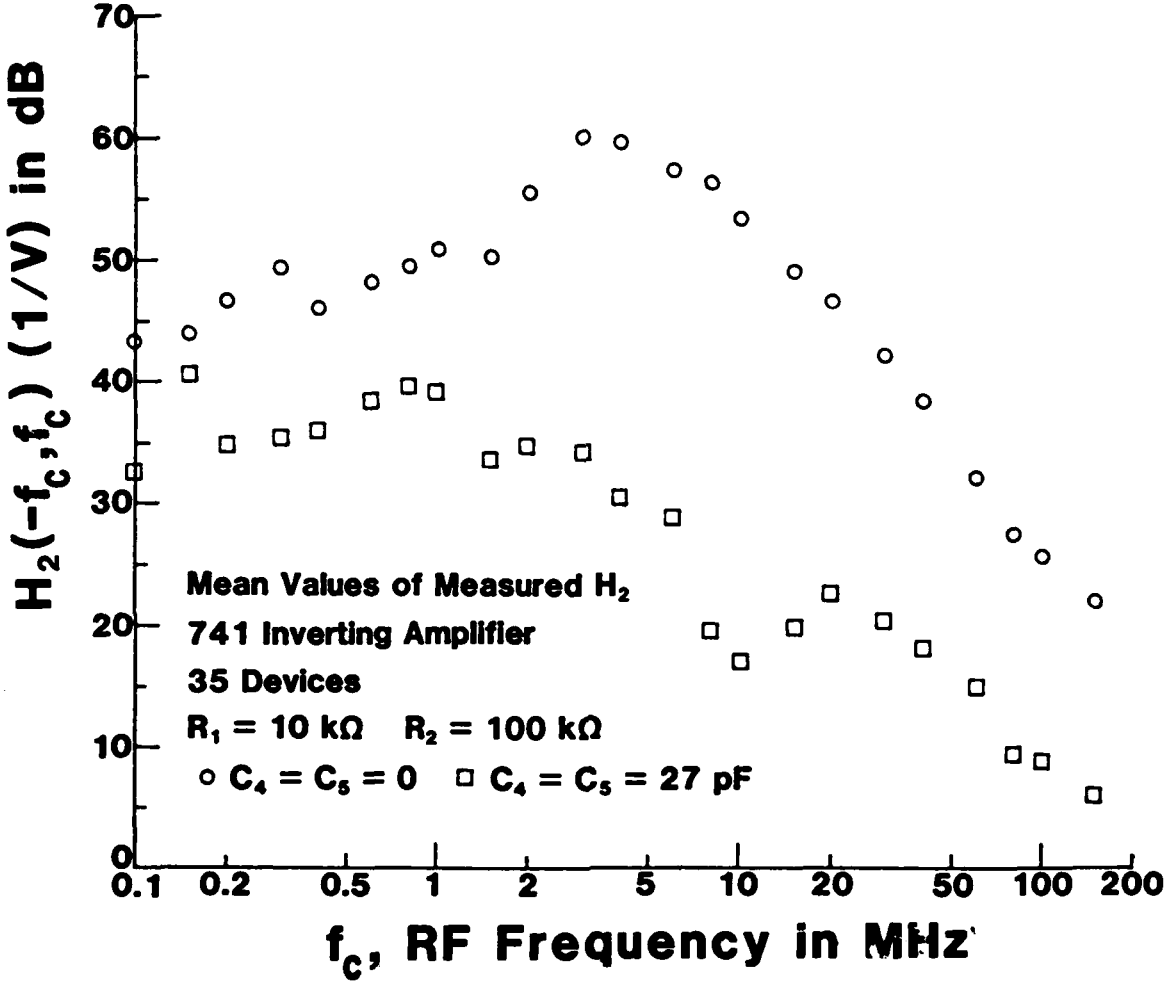

Fig.4-20 Mean values of measured H_2 $(-f_c,f_c)$ of the 3-stage op amp LED circuit for two feedback capacitor values, C4 = 0 and C4 = 27 pF. This plot shows the suppression of the demodulation RFI effects by the feedback capacitor.

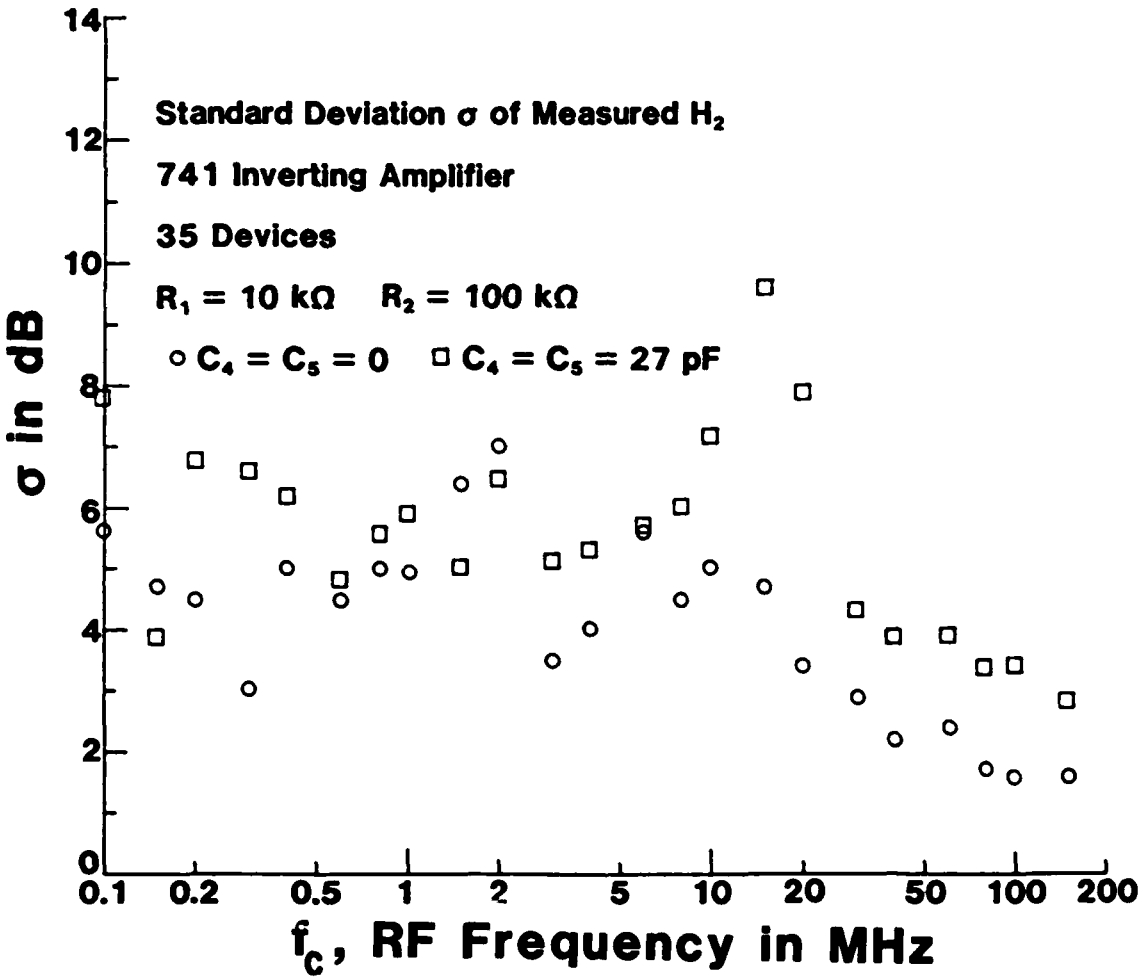

Fig. 4-21. Standard deviation, σ, of the measured $H_2(-f_c, f_c)$ of the 3-stage op amp LED circuit for two feedback capacitor values, C4 = 0 and C4 = 27 pF. This plot shows the spreading of H_2 values is wider in general for C4 = 27 pF than for C4 = 0.

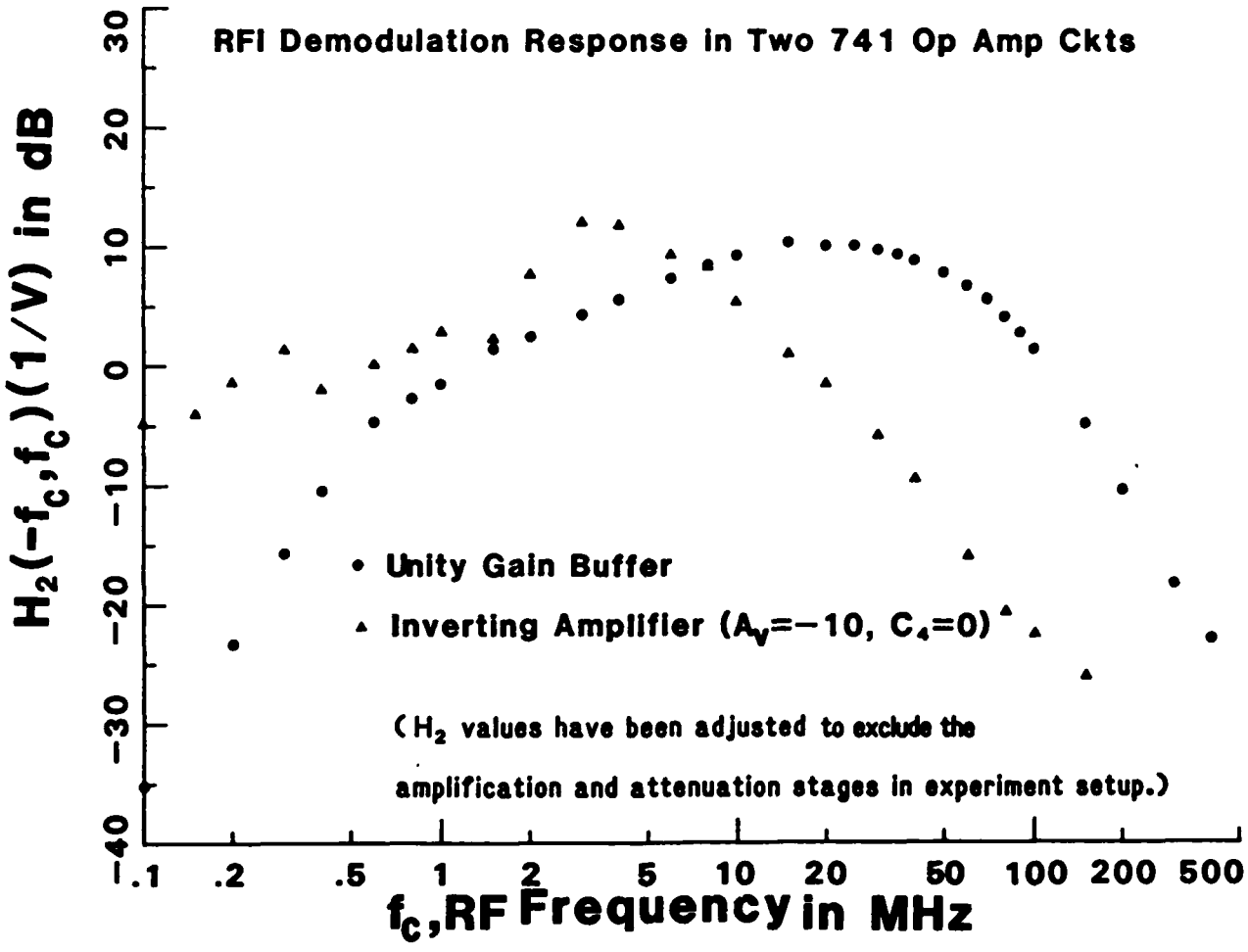

Fig. 4-22. Measured mean values of the second-order transfer function $H_2(-f_c,f_c)$ vs RF frequency for two 741 op amp circuits. The H_2 values for the unity gain buffer were obtained by adding 18 dB to the H_2 values shown in Fig. 4-14. The H_2 values for the inverting amplifier were obtained by subtracting 48 dB from the H_2 values shown in Fig. 4-20.

put to the RF voltage at the noninverting input terminal. We must account for the voltage division at the output which contributes a factor of (2) and the voltage division at the input which contributes a factor of $(2)^2$. See Figure 4-7. Therefore, the relationships between H_2' and H_2 are given by

$$|H_2'(-f_c,f_c)| = 8|H_2(-f_c,f_c)| \tag{4-15}$$

$$20\log_{10}|H_2'(-f_c,f_c)| = 20\log_{10}|H_2(-f_c,f_c)| + 18.1 \tag{4-16}$$

The result is an increase of 18 dB in the H_2 values plotted in Figure 4-14. Also H_2 values for the 741 inverting amplifier from Figure 4-20 have been adjusted using Eq. (4-14). The result is a decrease of 48 dB in the values plotted in Figure 4-20. The adjusted H_2' values in Figure 4-22, therefore, exclude the linear amplification and attenuation stages in the experimental setups. The adjusted mean values for H_2' are surprisingly similar in that both sets of data points have a peak value near 10 dB. The comparison shows that the 741 unity gain buffer has a lower average RFI response for RF frequencies below 8 MHz. Above 8 MHz, the average RFI demodulation response in the 741 inverting amplifier is lower.

V. The Experiment

In the previous two chapters, examples of significant variations in coupling characteristics of a transfer function were shown. The purpose of this chapter is to review an experiment which combined these two transfer functions. The object of the experiment is to investigate the feasibility and adequacy of combining individual statistics on separate parts of the overall transfer function.

5.1 Cable Coupling Variability

In Chapter 3, the sensitivity of cable coupling (crosstalk) to variations in relative wire position was examined. It was found that the sensitivity of crosstalk to variations in relative wire position was a strong function of the values of the load impedances. It was found that for "high impedance" loads, R = 1 kΩ, that the sensitivity to changes in wire position could be extraordinarily large. Changes in crosstalk caused by rewrapping the 25-wire cable bundle caused variations of as much as 20 dB even for frequencies where the line was electrically very short.

The 25 wire cable bundle described in Chapter 3 was reconstructed. Additional data were taken in the manner described in Chapter 3 for R = 50 Ω and R = 1 kΩ loads. The bundle was rewrapped, loads of R = 50 Ω were attached and the crosstalk was measured for frequencies of 4 MHz, 5 MHz, 10 MHz and 15 MHz. Then loads of R = 1 kΩ were attached and the crosstalk data retaken. This constituted the data for bundle 11. (The 10 data points obtained previously constitute cables 1 through 10.) The bundle was rewrapped and the above data retaken. This constitutes cable 12.

This process was repeated to yield data for a total of 60 cables. The results at frequencies of 4 MHz, 5 MHz, 10 MHz and 15 MHz are shown in Fig.

5.1-1 for R = 50 Ω and for R = 1 kΩ. Note that a similar sensitivity uncovered previously is found for these additional data. For R = 50 Ω, we observe virtually no sensitivity to changes in relative wire position caused by rewrapping the bundle. There is more sensitivity at 15 MHz than at 4 MHz, 5 MHz and 10 MHz. This is because the cable is becoming electrically long. At 15 MHz, the cable is approaching 1/4 λ in electrical length. Thus sensitivity to variations in wire position can be expected to become more severe at this frequency than at 4 MHz, 5 MHz and 10 MHz. However, note that the variability of the crosstalk caused by rewrapping the cable bundle with R = 1 kΩ is significant at all frequencies. The difference in the maximum and minimum crosstalk for the 60 bundles is on the order of 15 dB at 4 MHz.

These data will be used in a combined experiment which is discussed at the end of this chapter. In the next section we will investigate the variability in the nonlinear transfer functions of Op Amps.

RANDOM BUNDLE,4M(1V INPUT,OUTPUT IN MV)

RESISTANCE=	1K OHM			50 OHM			
FREQ= 4.0E6	5.0E6	1.0E7	1.5E7	4.0E6	5.0E6	1.0E7	1.5E7
66.5	81.1	143.	167.	87.0	74.0	14.4	70.3
74.0	98.5	55.8	25.4	82.5	76.0	23.8	69.8
88.1	126.	218.	62.9	113.	115.	29.8	50.1
120.	149.	235.	275.	88.1	75.0	42.2	139.
105.	141.	85.0	128.	91.3	83.8	15.4	67.1
86.0	127.	113.	51.8	88.8	86.0	30.0	43.5
109.	146.	411.	89.0	95.8	90.1	50.2	25.4
46.5	69.4	173.	79.5	64.5	65.9	32.5	46.3
55.8	79.1	217.	138.	75.1	73.5	35.0	87.0
55.3	73.2	59.6	64.9	70.4	66.0	12.5	40.8
77.6	97.0	161.	71.5	97.4	87.9	13.0	11.7
66.5	91.9	93.0	42.8	84.3	84.5	21.1	44.8
80.2	113.	182.	290.	85.0	81.3	28.3	79.8
55.1	79.1	27.6	17.5	87.9	87.2	13.2	52.0
49.4	69.7	135.	151.	70.2	66.0	18.7	54.0
90.2	123.	145.	67.9	85.3	79.2	50.1	129.
46.2	64.5	102.	98.0	76.4	75.4	14.0	72.3
56.0	64.9	162.	67.1	74.8	69.8	45.5	42.0
59.9	74.9	168.	154.	84.0	76.0	11.4	56.8
108.	133.	347.	165.	114.	100.	44.6	11.8
134.	172.	285.	236.	119.	109.	46.2	60.0
49.8	70.1	60.4	73.0	70.1	68.3	21.5	78.2
83.1	117.	164.	65.9	90.4	87.2	25.6	50.9
127.	155.	600.	299.	116.	99.0	67.9	95.8
68.1	80.9	159.	190.	93.2	82.0	14.8	62.5
121.	151.	346.	189.	99.1	87.0	38.7	54.8
58.9	83.2	73.0	53.2	80.3	79.2	37.1	54.4
70.3	94.0	65.1	51.7	88.0	83.9	23.6	18.7
61.2	88.8	203.	184.	82.0	79.2	26.9	95.2
55.4	72.0	66.4	127.	80.8	72.5	33.3	104.
62.3	78.6	87.8	74.6	90.1	73.9	25.6	48.2
52.3	73.2	147.	25.3	85.5	82.5	35.0	65.1
85.8	122.	81.0	64.4	98.5	94.8	9.8	31.4
84.9	114.	42.9	84.0	96.1	90.9	14.2	46.5
59.5	78.2	110.	13.5	95.0	91.1	27.9	61.2
47.0	54.8	83.7	97.9	78.2	67.1	17.6	71.5
74.2	88.0	103.	53.8	90.6	88.9	27.8	48.7
54.3	69.5	68.0	49.2	87.1	80.0	8.5	57.1
51.1	68.5	114.	79.0	91.2	92.1	34.0	45.3
52.1	80.0	101.	78.3	82.1	78.5	30.1	51.7
66.2	96.0	174.	91.3	83.0	83.3	37.0	40.8
63.9	90.0	52.0	73.2	81.1	74.7	20.5	48.0
63.1	81.8	24.2	97.2	80.5	74.5	10.7	90.1
57.0	79.8	184.	6.8	70.9	62.1	26.5	32.2
51.0	69.9	144.	150.	79.2	73.0	46.1	86.9
63.8	77.0	237.	92.8	78.8	67.5	16.1	60.9
54.3	71.2	120.	70.2	77.9	73.0	43.3	81.0
48.3	64.3	105.	95.4	86.5	89.8	20.3	48.9
47.5	62.9	24.7	50.0	80.8	72.2	33.2	32.5
85.0	115.	143.	81.0	86.1	78.2	16.4	20.7
75.0	96.0	184.	125.	84.0	68.0	13.8	82.0
34.0	49.0	260.	132.	78.0	77.2	19.5	56.2
42.0	57.0	980.	120.	78.5	73.3	36.8	60.0
24.4	31.7	148.	42.5	69.0	60.0	34.8	51.0
94.0	114.	146.	65.0	85.0	73.0	12.6	18.2
89.0	100.	295.	178.	83.2	70.0	21.2	76.0
93.8	130.	87.0	83.0	82.0	75.0	16.8	25.4
62.5	73.5	91.0	132.	70.0	60.0	22.0	50.0
89.0	106.	107.	159.	81.2	66.5	38.8	80.0
50.0	64.0	107.	34.0	86.5	84.0	35.0	67.0

Fig. 5.1-1. Random cable sensitivity data for R = 50Ω and R = 1kΩ loads.

5.3 The Combined Experiment

The data of the previous two sections have shown the rather extreme variability which can occur in certain transfer functions which are important contributors to electromagnetic interference. In this section we will combine those variabilities in a single experiment. Our interest will be to obtain statistics on some overall transfer function which has these two individual parts as contributors.

A block diagram of the experiment which was performed was shown in Chapter II and is repeated in Fig. 5.3-1. The 25-wire cable bundle described in Chapter 3 is driven by an HP606-C oscillator. This carrier frequency was set at 4 MHz and 15 MHz. A 1 kHz modulation was applied to this carrier, and the level of modulation was set at 50%. This composite signal is applied to the right end of wire 25. The signal is coupled via crosstalk to the right end of wire 14. A printed circuit board is attached to the end of this wire. The detailed schematic of the board layout is shown in Fig. 5.3-2. Photographs of the board attached to the end of the cable bundle are shown in Fig. 5.3-3. The first stage is an inverting stage with a DC gain of

$$\frac{R_2}{R_1} = 10$$

This is followed by a low pass filter consisting of R_3 and C_2 with a 3dB cutoff frequency of 1764 Hz. This is followed by another inverting amplifier having a DC gain of

$$\frac{R_5}{R_3 + R_4} = 98$$

This second stage is followed by a highpass filter having a 3dB cutoff frequency of 159 Hz. A noninverting buffer stage with a DC gain of

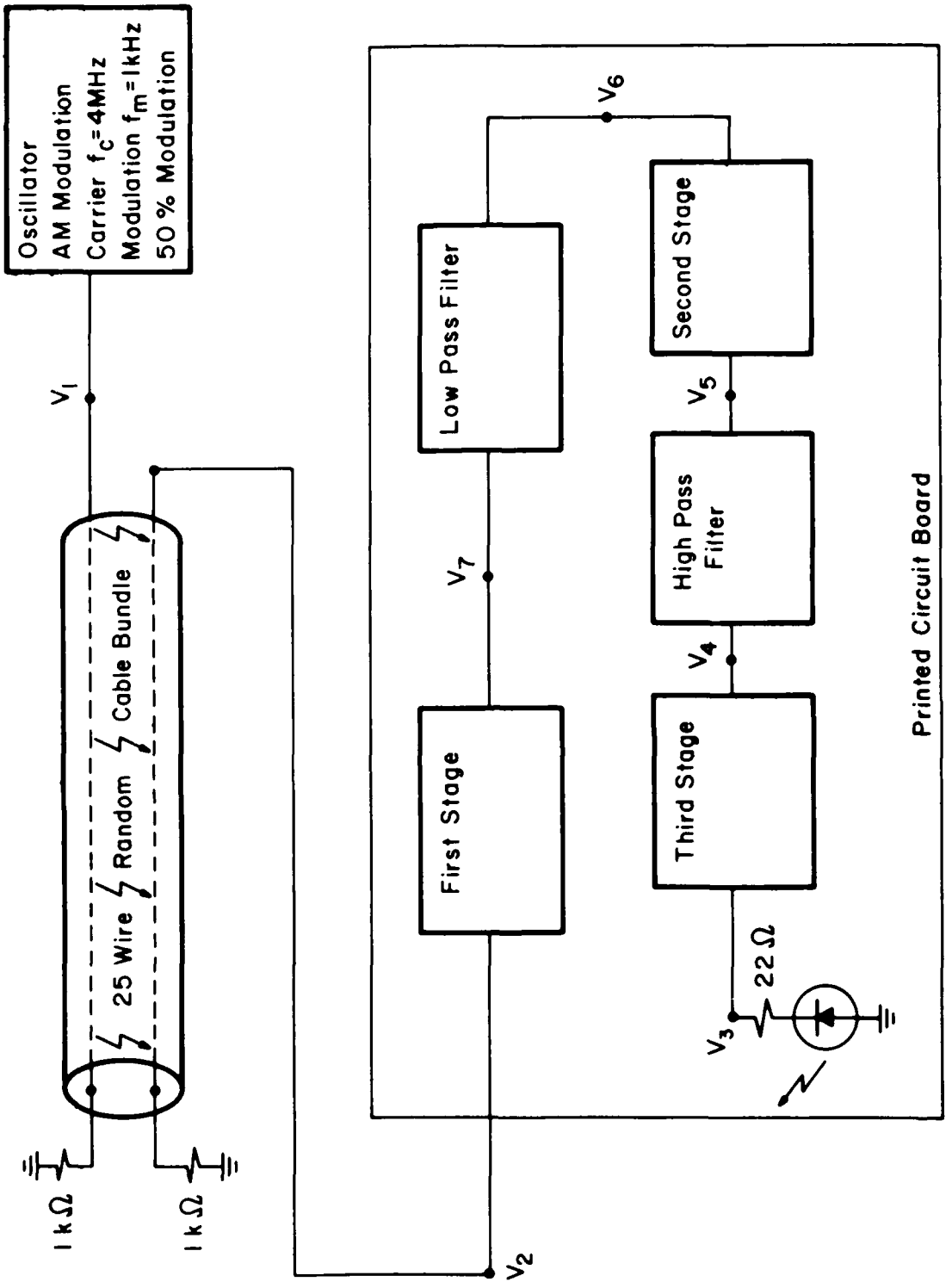

Fig. 5.3-1. Block diagram of experiment.

AD-A157 239 BASIC EMC (ELECTROMAGNETIC COMPATIBILITY) TECHNOLOGY ADVANCEMENT FOR C3 (... (U) SOUTHEASTERN CENTER FOR ELECTRICAL ENGINEERING EDUCATION INC S... 2/2

UNCLASSIFIED D WEINER ET AL. APR 85 RADC-TR-82-286-VOL-6 F/G 17/2 NL

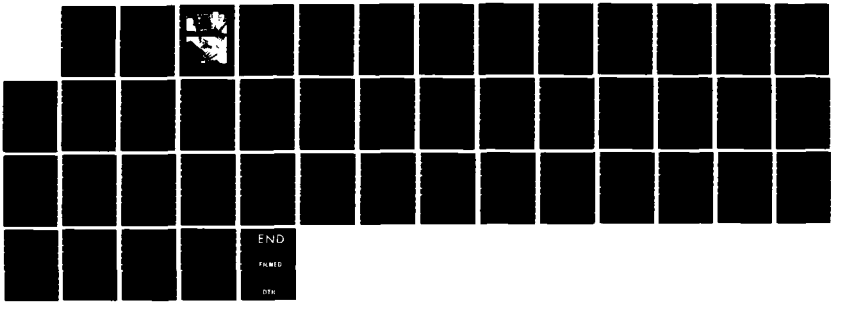

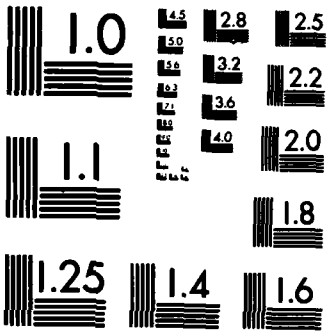

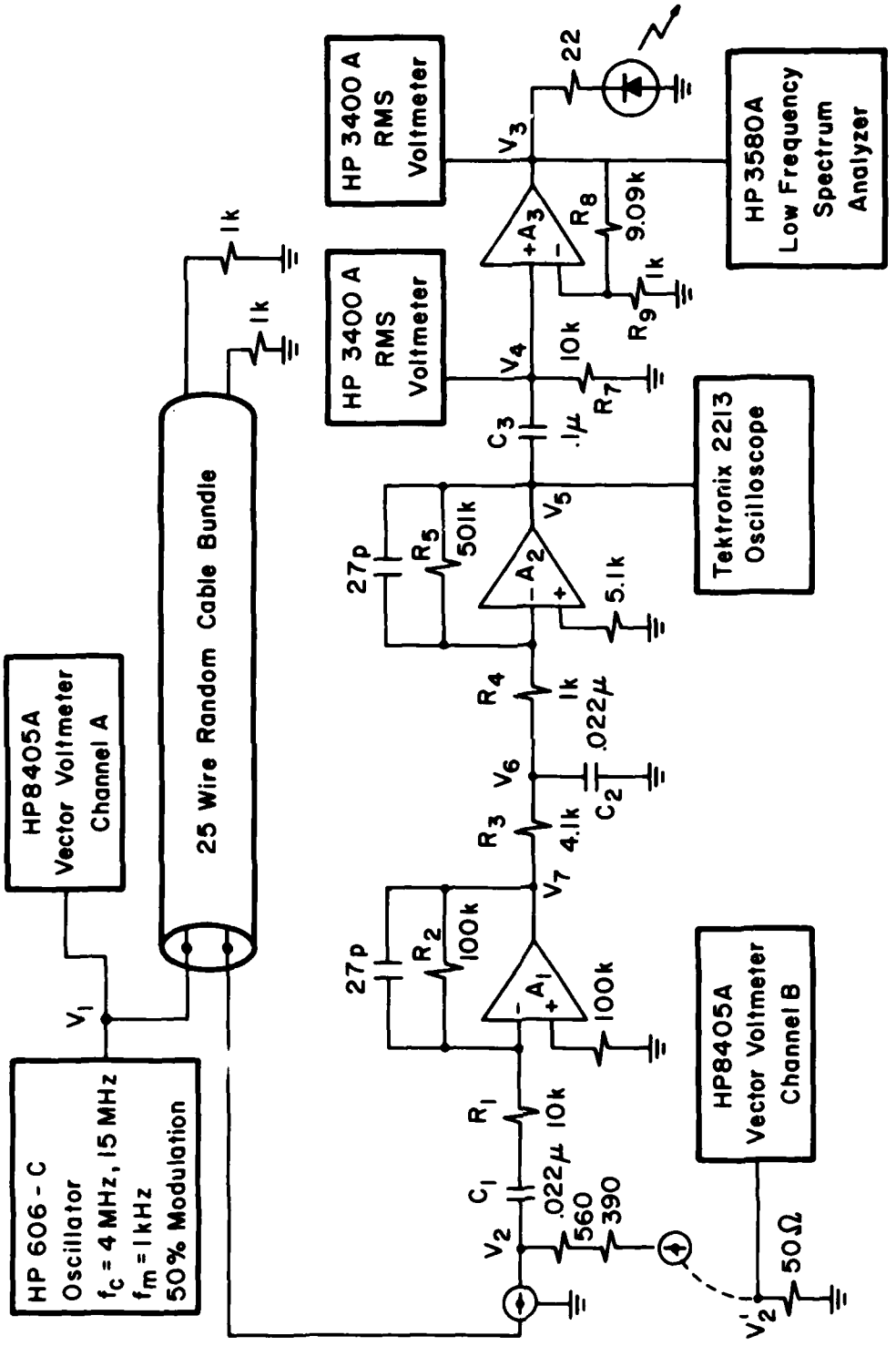

Fig. 5.3-2. Schematic of board.

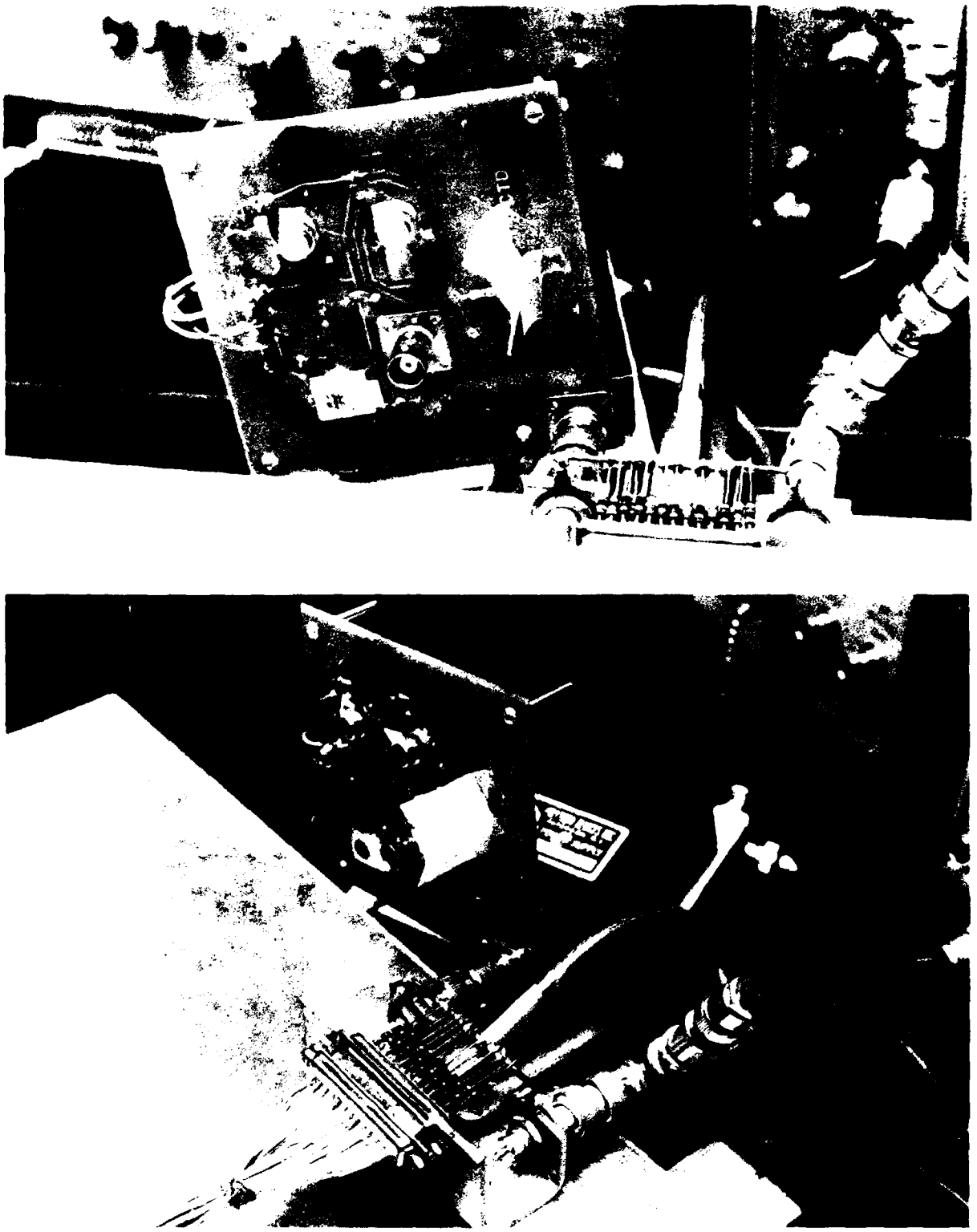

Fig. 5.3-3. The experimental configuration.

$$\frac{R_8 + R_9}{R_9} = 10.1$$

provides the final level to the LED. Thus the overall DC gain is

$$\frac{V_3}{V_2} = \frac{V_3}{V_4} \times \frac{V_4}{V_5} \times \frac{V_5}{V_6} \times \frac{V_6}{V_7} \times \frac{V_7}{V_z}$$

$$= 9898$$

The functioning of the circuit is as follows. The AM modulated signal at V_1 is coupled via crosstalk to the input of the board appearing at V_2. After passage through the first stage, DC, 1 kHz and 2 kHz components appear at the output of that stage at V_7. In addition any AM modulation which may exist is removed by the low pass filter resulting in a baseband signal at V_6. The resulting baseband signal is passed to the second stage which provides amplification. A highpass filter eliminates any DC which may be due to nonlinear rectification or DC offset resulting from the first two stages. During the course of the experiment the DC level at V_5 was monitored to ensure that the second stage was not driven into saturation. Finally, the resulting baseband signal at V_4 is passed through a buffer amplifier (the third stage) to the LED.

A total of 52 741 Op Amps were purchased. Of that total, 24 were National Semiconductor LM741 and 28 were Fairchild μA 741. Two of the Fairchild μA741 units were used in the second and third stages throughout the experiment while the remaining 50 units were used in the first stage.

A Hewlett-Packard 8405A Vector Voltmeter was used to measure the carrier level at V_1 (channel A). (A 10:1 divider was used on the A channel probe to insure that it would not be damaged by voltages greater than 2V.) A voltage divider was constructed on the board at V_2 as shown in Fig. 5.3-2. This consisted of a series combination of 560 + 390 = 950Ω connecting V_2 and the center

pin of a BNC connector mounted on the board. Channel B of the Vector Voltmeter was connected to this point (V_2') through a 50Ω feedthrough resistor. Therefore $V_2' = V_2/20$. (The actual ratio is 19.8675.) Thus the impedance from V_2 to ground was approximately 1 kΩ. (The input impedance of the Vector Voltmeter provided negligible loading across the 50Ω feedthrough.) The load impedance seen by wire 14 at the input to the board was then 1 kΩ in parallel with the impedance seen looking into the first stage. The total input impedance looking into the board was measured with an HP 4815A Vector Impedance Meter. At 4 MHz, the input impedance to the board was found to be $895\angle -12^{\circ}$ Ω, whereas at 15 MHz this impedance was found to be $720\angle -38^{\circ}$ Ω. The output of the second stage at V_5 was monitored with a Tektronix 2213 oscilloscope to ensure that the DC levels were small enough so that A2 was not driven into saturation. In all cases this level was less than one volt. Voltage V_4 was monitored with an HP 3400A RMS Voltmeter. The output level, V_3, was monitored with an HP 3400A RMS Voltmeter and an HP 3580A Low-Frequency Spectrum Analyzer. The reason for using both these instruments to monitor V_3 was that V_3 contained, in addition to 1 kHz, a 2 kHz component. The RMS Voltmeter shows the combination of these two components, whereas the spectrum analyzer clearly separates them. It was found that in all cases the 2 kHz component at V_3 was approximately 16 dB down from the 1 kHz component. It was the 1 kHz component at V_3 which was recorded.

In each case the carrier levels at V_1 required to produce 1 kHz levels at V_3 of .2V, .4V, 1V and sufficient to barely light the LED (normally around 1.25 V) were recorded. The procedure is as follows:

1) Wrap cable bundle.

2) Insert A1 Op Amp after trimming and straightening

leads.

3) Turn on power supply for Op Amps.

4) Turn up modulation to 50%, turn up carrier to get V_3 = .2V.

HP3590A set on linear and .2V/div

HP3400A V_3 set on .3V/div

HP3400A V_4 set on .03V/div

change HP3580A to .1V/div to read 2 kHz.

5) Turn down modulation.

6) Read $V_1/10$ on channel A of vector voltmeter.

7) Read V_2' on channel B of vector voltmeter.

8) Turn up modulation to 50% and set V_3 = .4V

HP3580A set on linear and 1V/div

HP3400A V_3 set on 1V/div

HP3400A V_4 set on .1V/div

change HP3580A to .2V/div to read 2 kHz.

9) Turn down modulation.

10) Read $V_1/10$ on channel A of vector voltmeter.

11) Read V_2' on channel B of vector voltmeter.

12) Turn up modulation to 50% and set V_3 = 1V.

HP3580A set on linear and 2V/div

HP3400A V_3 set on 1V/div

HP3400A V_4 set on .1V/div

change HP3580A to 1V/div to read 2 kHz.

13) Turn down modulation.

14) Read $V_1/10$ on channel A of vector voltmeter.

15) Read V_2' on channel B of vector voltmeter.

16) Turn up modulation to 50% and set V_3 to light (barely) LED

HP3580A set on linear and 2V/div

HP3400A V_3 set on 3V/div

HP3400A V_4 set on .3V/div

change HP3580A to 1V/div to read 2 kHz

17) Turn down modulation.

18) Read $V_1/10$ on channel A of vector voltmeter.

19) Read V_2' on channel B of vector voltmeter.

20) Change carrier frequency to 15 MHz and repeat steps (1) - (19)

21) Rewrap bundle and repeat steps (1) - (20).

Thus there are obtained 50 data points for each carrier frequency and V_3 level. Each data point gives the ratio of the 1 kHz component at V_3 to the (unmodulated) carrier level at V_1 for one bundle wrap and one of the 50 741 Op Amps. It should be observed that, from the data which was recorded, we are able to obtain (1) the cable coupling transfer function:

$$\frac{V_2 \text{ (carrier)}}{V_1 \text{ (carrier)}}$$

as well as (2) the nonlinear transfer function of the board:

$$\frac{V_3 \text{ (1 kHz)}}{V_2 \text{ (carrier)}}$$

The latter transfer function is related to H_2 of the board.

In the next chapter, these data will be analyzed.

VI. Analysis of the Feasibility Experiment Data

The feasibility experiment consisted of three independent investigations. One experiment studied the crosstalk variations in a 25-wire cable bundle caused by unwrapping and rewrapping the bundle. A second experiment examined fluctations in the second-order nonlinear transfer function of operational amplifiers. The third experiment investigated variability in the amplitude of an interfering signal needed to switch on an LED when a cable bundle was rewrapped and an operational amplifier changed each time the experiment was performed. These experiments are discussed in detail in Chapter V. In this chapter some of the experimental data is analyzed.

6.1 Analysis of the Crosstalk Data

The crosstalk within the cable bundle, from V_1 to V_2, was characterized by the linear voltage transfer function, G(f). The probability density function associated with $|G(f)|$ was denoted by $f_G(g)$. The data obtained for $|G(f)|$ is listed in Fig. 5.1-1 as a function of load resistance and frequency. Since the cable input voltage was 1 volt, the cable output voltage equals $|G(f)|$.

For analytical convenience, it is desirable to approximate $f_G(g)$ by a well known distribution. In general, several different distributions may provide acceptable approximations to the experimental data. The procedure for finding suitable distributions consisted of two steps. First, the coefficients of skewness and kurtosis, two measures which contain information relative to the shape of a distribution, were used to make preliminary selections of candidate distributions. The candidates were then tested to see whether any should be rejected on the basis of a significant statistical deviation between

the experimental data and the distribution being tested. Approximations to $f_G(g)$ were then chosen from those distributions which passed the test. However, it was not possible to state whether one distribution which passed the test was a better approximation than another distribution which also passed the test.

The coefficients of skewness and kurtosis are related to the $k^{\underline{th}}$ central moment of a random variable where k is a positive integer. Let the mean of the random variable G be denoted by m_G. The $k^{\underline{th}}$ central moment of G is defined to be

$$\mu_{Gk} = E[(G-m_G)^k] \tag{6.1-1}$$

where E[ ] denotes the statistical operation of expected value. By definition,

$$\alpha_{G3} = \frac{\mu_{G3}}{[\mu_{G2}]^{3/2}} = \text{coefficient of skewness} \tag{6.1-2}$$

and

$$\alpha_{G4} = \frac{\mu_{G4}}{[\mu_{G2}]^2} = \text{coefficient of kurtosis.} \tag{6.1-3}$$

The coefficient of skewness is a measure of the asymmetry of the probability density function. The coefficient of kurtosis is a measure of the "peakedness" or "flatness" of the probability density function in the central part of the distribution.

Because the underlying distribution of G is unknown, it is necessary to use the experimental data to estimate m_G, μ_{G2}, μ_{G3}, and μ_{G4}. Let N_G denote the number of rewrappings of the cable bundle. Also, let g_k denote the measured crosstalk linear transfer function for the k^{th} rewrapping of the

bundle. Unbiased estimates for m_G, μ_{G2}, μ_{G3}, and μ_{G4} are then given by

$$\hat{m}_G = \frac{1}{N_G} \sum_{k=1}^{N_G} g_k, \tag{6.1-4}$$

$$\hat{\mu}_{G2} = \frac{1}{N_G-1} \sum_{k=1}^{N_G} (g_k - \hat{m}_G)^2, \tag{6.1-5}$$

$$\hat{\mu}_{G3} = \frac{N_G}{(N_G-1)(N_G-2)} \sum_{k=1}^{N_G} (g_k-\hat{m}_G)^3, \tag{6.1-6}$$

$$\hat{\mu}_{G4} = \frac{N_G^2}{(N_G-1)(N_G^2-3N_G+3)} \sum_{k=1}^{N_G} (g_k-\hat{m}_G)^4 - \frac{6N_G-9}{N_G^2-3N_G+3} [\hat{\mu}_{G2}]^2. \tag{6.1-7}$$

Using Eqs. (6.1-4) through (6.1-7) in Eqs. (6.1-2) and (6.1-3), estimates of the coefficients of skewness and kurtosis become

$$\hat{\alpha}_{G3} = \frac{\hat{\mu}_{G3}}{[\hat{\mu}_{G2}]^{3/2}} \tag{6.1-8}$$

$$\hat{\alpha}_{G4} = \frac{\hat{\mu}_{G4}}{[\hat{\mu}_{G2}]^2} . \tag{6.1-9}$$

Preliminary selections of some well known distributions for approximating $f_G(g)$ are made by comparing the estimates, $\hat{\alpha}_{G3}$ and $\hat{\alpha}_{G4}$, with the known values, α_{G3} and α_{G4}, of the various distributions under consideration. Those distributions for which a reasonable match exists become candidates for further consideration. In general, the probability density functions of the well known distributions contain two or more numerical parameters for which numerical values must be determined in order for the distribution to be completely specified. These parameters were chosen such that the mean and variance of the distribution equaled, respectively, the sample mean, $\hat{m}_G$, and the sample variance, $(\hat{\sigma}_G)^2 = \hat{\mu}_{G2}$. It can be shown, however, that the

coefficients of skewness and kurtosis are independent of the mean and variance of a distribution.

Having selected a group of possible distributions for approximating $f_G(g)$ on the basis of comparing $\hat{\alpha}_{G3}$ and $\hat{\alpha}_{G4}$ with α_{G3} and α_{G4}, respectively, it is then desirable to perform a "goodness of fit" test on each candidate distribution. This enables a distribution to be rejected when a significant statistical deviation exists between the experimental data and the distribution being tested. Even though a distribution is not rejected by the statistical test, it cannot be accepted with perfect confidence. In addition, if several distributions are not rejected, the goodness of fit test cannot be used to accept one distribution over another. The best that can be said regarding distributions which pass the test is that they were not rejected. The goodness of fit test prevents acceptance of a distribution which is likely to be a poor approximation for $f_G(g)$.

The χ^2 test [16] was used as the goodness of fit test. In applying this test, the range of G was divided into 5 cells such that it was equally probable G would fall into each cell for the distribution under test. Let n_k denote the number of data which fell into the k^{th} cell. The relative frequency of occurrence for the k^{th} cell was defined to be

$$\hat{p}_k = \frac{n_k}{N_G} \; ; \; k = 1,2,\ldots,5. \tag{6.1-10}$$

The χ^2 statistic was then evaluated using the relation

$$\chi^2 = N_G \sum_{k=1}^{5} \frac{(\hat{p}_k - 0.2)^2}{0.2} \; . \tag{6.1-11}$$

The significance level, β_o, is defined to be the conditional probability of rejecting the distribution given that the distribution under test is a

suitable approximation. In applying the χ^2 test, the significance level was chosen to be

$$\beta_o = 0.01 \tag{6.1-12}$$

In addition,

$$N_G = 60 \tag{6.1-13}$$

for the crosstalk data of Fig. 5.1-1. The numerical value obtained for the χ^2 statistic, using Eq.(6.1-11), was then compared to a threshold value tabulated for $\beta_o = 0.01$ and the distribution under test [16]. The distribution under test was accepted as a suitable approximation to $f_G(g)$ provided the computed value of the χ^2 statistic was less than the tabulated threshold.

The data of Fig. 5.1-1 reveal that the 1kΩ resistive load resulted in significant crosstalk variability at all frequencies tested. Consequently, in the feasibility experiment, the 25-wire cable bundle was terminated in approximately a 1kΩ resistive load. The carrier frequency of the AM interference was selected to be 4 MHz and 15 MHz. Therefore, approximate probability density functions for $f_G(g)$ were found only for the data corresponding to

1) $R = 1k\Omega$, $f_c = 4$ MHz

2) $R = 1k\Omega$, $f_c = 15$ MHz.

This data is found in the first and fourth columns of Fig. 5.1-1. The two cases are discussed separately.

Case 1: $R=1k\Omega$, $f_c = 4$ MHz

Using the data from the first column of Fig. 5.1-1, the estimated mean, variance, coefficient of skewness, and coefficient of kurtosis were calculated to be

$$\hat{m}_G = 7.002 \times 10^{-2} \text{ volts}$$

$$(\hat{\sigma}_G)^2 = \hat{\mu}_{G2} = 5.48 \times 10^{-4} \text{ (volts)}^2$$

$$\hat{\alpha}_{G3} = 0.859 \qquad (6.1\text{-}14)$$

$$\hat{\alpha}_{G4} = 3.285$$

Since the coefficients of skewness and kurtosis are independent of mean and variance, normalized distributions with zero mean and unit variance were considered as candidates. These distributions are convenient to work with because only one parameter is needed to characterize them [16]. The selected candidates are listed below along with their coefficients of skewness and kurtosis:

a) Log Normal (C = 1/4), $\alpha_3 = 0.778$, $\alpha_4 = 4.096$

b) Weibull ($\beta = 2$), $\alpha_3 = 0.63$, $\alpha_4 = 3.24$

c) Gamma (a = 7), $\alpha_3 = 0.71$, $\alpha_4 = 3.75$.

Application of the χ^2 test resulted in acceptance of the Log Normal and Gamma distributions but in rejection of the Weibull. Inserting the sample mean and variance from Eqs.(6.1-14), the analytical expressions for the density functions of the Log Normal and Gamma distributions are given by:

Log Normal (C = 1/4)

$$f_G(g) \simeq \begin{cases} 1.596(g + .022)^{-1} \exp\{-8[\ln((11.193)(g+.022))]^2\}, & g \geq -.022 \\ 0, & g < -.022 \end{cases} \qquad (6.1\text{-}15)$$

Gamma (a = 7)

$$f_G(g) \simeq \begin{cases} (9.016 \times 10)^{12}(g-.004)^7 \exp\{-120.831(g-.004)\}, & g \geq .004 \\ 0, & g < .004 \end{cases} \qquad (6.1\text{-}16)$$

The two density functions are plotted in Figs. 6.1-1(a) and (b), respectively. Observe that multiplicative factors are noted along the axes.

Case 2: $R = 1k\Omega$, $f_c = 15$ MHz

Using the data from the fourth column of Fig. 5.1-1, the estimated mean, variance, coefficient of skewness, and coefficient of kurtosis were calculated to be

$$\hat{m}_G = 1.03 \times 10^{-1} \text{ Volts}$$

$$(\hat{\sigma}_G)^2 = \hat{\mu}_{G2} = 4.30 \times 10^{-3} \text{ (Volts)}^2 \qquad (6.1\text{-}17)$$

$$\hat{\alpha}_{G3} = 1.224$$

$$\hat{\alpha}_{G4} = 4.279.$$

The selected candidates are listed below along with their coefficients of skewness and kurtosis:

a) Log Normal (C = 1/4), $\alpha_3 = 0.778$, $\alpha_4 = 4.096$

b) Gamma (a = 3), $\alpha_3 = 1$, $\alpha_4 = 4.5$

c) Gamma (a = 4), $\alpha_3 = 0.89$, $\alpha_4 = 4.2$.

Application of the χ^2 test resulted in acceptance of both Gamma-distributions but in rejection of the Log Normal. Inserting the sample mean and variance from Eqs. (6.1-17), the analytical expressions for the density functions of the Gamma distributions are given by:

Gamma (a = 3)

$$f_G(g) \begin{cases} (1.444 \times 10^5)(g+.028)^3 \exp\{-30.51\ (g+.0281)\}, & g \geq -.028 \\ 0, & g < -.028 \end{cases} \qquad (6.1\text{-}18)$$

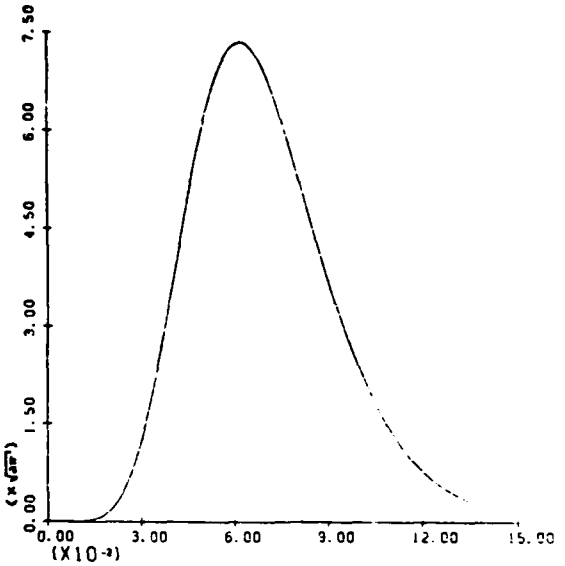

(a)

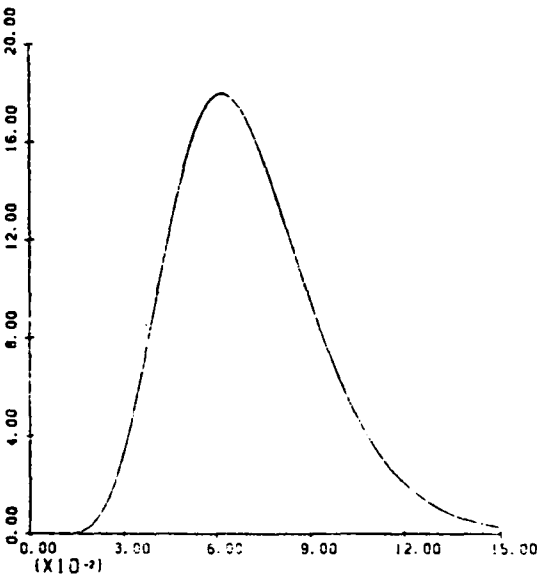

(b)

Fig. 6.1-1. Approximations to $f_G(g)$ at 4MHz. (a) Log Normal (c = 1/4), (b) Gamma (a = 7).

Gamma (a = 4)

$$f_G(g) \cong \begin{cases} (1.924 \times 10^6)(g + 0.44)^4 \exp\{-34.111(g+.044)\}, & g \geq -.044 \\ 0, & g < -.044 \end{cases} \quad (6.1\text{-}19)$$

The two density functions are plotted in Figs. 6.1-2(a) and (b), respectively.

6.2. Analysis of the Second-Order Nonlinear Transfer Function Data.

Demodulation of the AM interference was characterized by $H_2(-f_c,f_c)$, the second-order nonlinear transfer function relating the intefering signal at V_2 to the demodulated 1 kHz tone at V_3. In determining $|H_2(-f_c,f_c)|$, V_3 was measured directly. However, V_2 was measured using a 2:1 voltage divider. If the measurements for V_2 and V_3 are denoted by V_{2m} and V_{3m}, respectively, then

$$\begin{aligned} V_2 &= 2V_{2m} \\ V_3 &= V_{3m}. \end{aligned} \quad (6.2\text{-}1)$$

From Eq. (2.4-2)

$$A_3 = mA_2^2|H_2(-f_c,f_c)|. \quad (6.2\text{-}2)$$

Therefore, the magnitude of the second-order nonlinear transfer function is given by

$$|H_2(-f_c,f_c)| = \frac{A_3}{mA_2^2} \quad (6.2\text{-}3)$$

Recall that A_3 and A_2 refer to peak values. Since the measurements were recorded as rms voltages,

$$\begin{aligned} A_2 &= 2\sqrt{2}\ V_{2m} \\ A_3 &= \sqrt{2}\ V_{3m} \end{aligned} \quad (6.2\text{-}4)$$

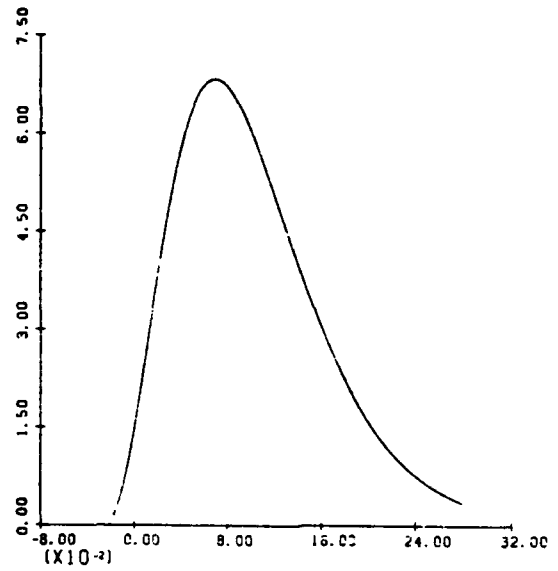

(a)

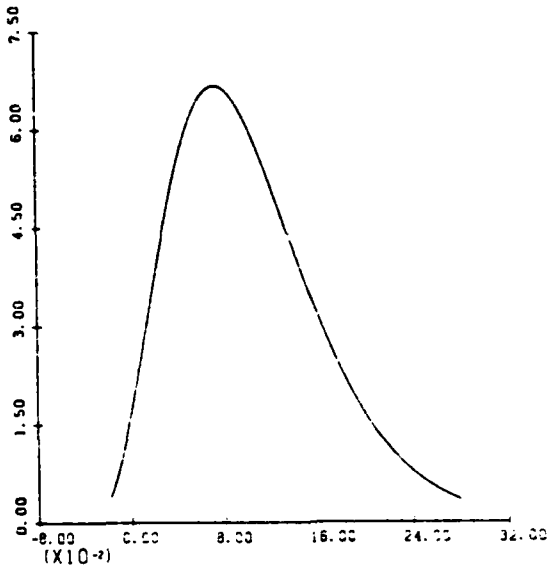

(b)

Fig. 6.1-2. Approximations to $f_G(g)$ at 15 MHz. (a) Gamma (a = 3), (b) Gamma (a = 4).

In the experiment the modulation index was set at

$$m = 0.5. \tag{6.2-5}$$

Consequently, Eq.(6.2-3) can be rewritten as

$$|H_2(-f_c,f_c)| = \frac{\sqrt{2}\ V_{3m}}{(0.5)(2\sqrt{2}\ V_{2m})^2} = 0.354\ \frac{V_{3m}}{(V_{2m})^2}. \tag{6.2-6}$$

Eq. (6.2-6) was used to evaluate $|H_2(-f_c,f_c)|$.

As explained in section 5.2, measurements were taken on both μA 741 and LM 741 operational amplifiers. $|H_2(-f_c,f_c)|$ was found to be significantly smaller at 15 MHz for the LM 741 devices. As a result, it was not possible to light the LED at 15 mHZ when LM 741's were inserted into the first stage of the PCB during the feasibility experiment. Because of this, only the data involving the μA 741 operational amplifiers were analyzed. The data at 4 MHz and 15 MHz are tabulated in Figs. 6.2-1 and 6.2-2, respectively, along with the computed values of $|H_2(-f_c,f_c)|$.

The probability density function associated with $|H_2(-f_c,f_c)|$ was denoted by $f_H(h)$. The procedure used to obtain approximations to $f_H(h)$ was identical to that followed for $f_G(g)$. Let N_H denote the number of operational amplifiers measured. Also, let $\hat{m}_H$ and $\hat{\mu}_{Hk}$ denote estimates of the mean and k^{th} central moment of the random variable H. Finally, let $\hat{\alpha}_{H3}$ and $\hat{\alpha}_{H4}$ denote estimates of the coefficients of skewness and kurtosis for $f_H(h)$. If h_k represents the measured second-order nonlinear transfer function of the k^{th} operational amplifier, then expressions for evaluation of $\hat{m}_H$, $\hat{\mu}_{H2}$, $\hat{\mu}_{H3}$, $\hat{\mu}_{H4}$, $\hat{\alpha}_{H3}$, and $\hat{\alpha}_{H4}$ are identical in form to those given by Eqs. (6.1-4) through (6.1-9).

As was the case for $f_G(g)$, the χ^2 statistic was evaluated using the

Device Number	V_{2m} (Volts)	V_{3m}(Volts)	$\lvert H_2(-f_c,f_c)\rvert$ (Volts^{-1})
1	.0203	0.2	171.6
2	.021	0.2	160.3
3	.0165	0.2	259.7
4	.0185	0.2	206.6
5	.019	0.2	195.9
6	.019	0.2	195.9
7	.0189	0.2	198.0
8	.0212	0.2	157.3
9	.0197	0.2	182.2
10	.0182	0.2	213.5
11	.0204	0.2	169.9
13	.021	0.2	160.3
14	.0222	0.2	143.5
15	.021	0.2	160.3
16	.0222	0.2	143.5
19	.0209	0.2	161.9
41	.0127	0.2	438.4
42	.0135	0.2	388.0
43	.0109	0.2	595.1
44	.013	0.2	418.4
45	.0115	0.2	534.7
46	.0111	0.2	573.9
47	.0109	0.2	595.2
48	.0143	0.2	345.8
51	.0189	0.2	198.0
52	.0204	0.2	169.9
53	.0197	0.2	182.8
54	.0191	0.2	193.8
55	.0205	0.2	168.3
56	.0178	0.2	223.2
57	.0194	0.2	187.9
58	.0291	0.2	83.5
59	.017	0.2	244.7
60	.0223	0.2	142.2

Fig. 6.2-1. Measurements and Calculation of $\lvert H_2(-f_c,f_c)\rvert$ at 4 MHz.

Device Number	V_{2m} (Volts)	V_{3m} (Volts)	$\lvert H_2(-f_c,f_c)\rvert$ (Volts^{-1})
1	.0302	0.2	77.5
2	.0358	0.2	55.2
3	.0238	0.2	124.8
4	.053	0.2	25.2
5	.026	0.2	104.6
6	.0294	0.2	81.8
7	.054	0.2	24.2
8	.0298	0.2	79.6
9	·0337	0.2	62.3
10	.0337	0.2	62.3
11	.0305	0.2	76.0
13	.0365	0.2	53.1
14	.028	0.2	90.2
15	.0332	0.2	64.2
16	.0322	0.2	68.2
19	.0413	0.2	41.5
41	.026	0.2	104.6
42	.034	0.2	61.2
43	.0217	0.2	150.2
44	.024	0.2	122.8
45	.0219	0.2	147.4
46	.023	0.2	133.7
47	.0238	0.2	124.8
48	.0278	0.2	91.5
51	.0265	0.2	100.7
52	.0212	0.2	157.3
53	.0243	0.2	119.8
54	.0224	0.2	140.9
55	.0232	0.2	131.4
56	.0285	0.2	87.1
57	.0278	0.2	91.5
58	.0263	0.2	102.2
59	.0275	0.2	93.5
60	.032	0.2	69.1

Fig. 6.2-2. Measurements and calculation of $\lvert H_2(-f_c,f_c)\rvert$ at 15 MHz.

relation

$$\chi^2 = N_H \sum_{k=1}^{5} \frac{(\hat{p}k - 0.2)^2}{0.2}. \qquad (6.2\text{-}7)$$

For the data of Figs. 6.2-1 and 6.2-2

$$N_H = 34. \qquad (6.2\text{-}8)$$

Once again, the numerical value obtained for the χ^2 statistic was compared to a threshold value tabulated for a significance level given by

$$\beta_o = 0.01 \qquad (6.2\text{-}9)$$

and the distribution under test. The cases for f_c = 4MHz and f_c = 15 MHz are discussed separately.

Case 1: f_c = 4 MHz

Using the data from Fig. 6.2-1, the estimated mean, variance, coefficient of skewness, and coefficient of kurtosis were calculated to be

$$\hat{m}_H = 2.519 \times 10^2 \text{ Volts}^{-1}$$

$$(\hat{\sigma}_H)^2 = \hat{\mu}_{H2} = 2.048 \times 10^4 \text{ Volts}^{-2} \qquad (6.2\text{-}10)$$

$$\hat{\alpha}_{H3} = 1.480$$

$$\hat{\alpha}_{H4} = 3.703$$

The selected candidates for approximating $f_H(h)$ are listed below along with their coefficients of skewness and kurtosis:

a) Gamma (a = 1), $\alpha_3 = 1.41$, $\alpha_4 = 6$

b) Gamma (a = 7), $\alpha_3 = 0.71$, $\alpha_4 = 3.75$

c) Weibull (β= 2), $\alpha_3 = 0.63$, $\alpha_4 = 3.24$

d) Log Normal (c = 1/4), $\alpha_3 = 0.778$, $\alpha_4 = 4.096$

Application of the χ^2 test resulted in rejection of all four distributions.

However, the χ^2 test works best when the number of data points is much greater than 30. Because $N_H = 34$, it was decided to utilize the Kolmogorov - Smirnov test which works well when the number of data points equals 30 or less [16]. As before, the significance level of the test was set at $\beta_c = 0.01$. The Kolmogorov-Smirnov test resulted in the acceptance of all four candidate distributions. Inserting the sample mean and variance from Eqs.(6.2-10), the analytical expressions for the approximations to $f_H(h)$ are given by:

Gamma (a = 1)

$$f_H(h) \cong \begin{cases} (97.65 \times 10^{-6})(h-49.5)\exp\{-(9.882 \times 10^{-3})(h-49.5)\}, & h \geq 49.5 \\ 0, & h < 49.5 \end{cases} \quad (6.2\text{-}11)$$

Gamma (a = 7)

$$f_H(h) \cong \begin{cases} (4.618 \times 10^{-18})(h+152.9)^7\exp\{-(1.976 \times 10^{-2})(h+152.9)\}, & h \geq -152.9 \\ 0, & h < -152.9 \end{cases} \quad (6.2\text{-}12)$$

Weibull (β = 2)

$$f_H(h) \cong \begin{cases} (4.55 \times 10^{-4})(h-193.1)\exp\{-(2.275 \times 10^{-4})(h-193.1)^2\}, & h \geq 193.1 \\ 0, & h < 193.1 \end{cases} \quad (6.2\text{-}13)$$

Log Normal (C = 1/4)

$$f_H(h) \cong \begin{cases} 1.596\ (h-241.7)^{-1} \exp\{-8[\ln((.102)(h-241.7))]^2\}, & h \geq 241.7 \\ 0, & h < 41.7. \end{cases} \quad (6.2\text{-}14)$$

The four density functions are plotted in Figs. 6.2-3(a), (b),(c), and (d), respectively.

Case 2: f_c = 15 MHz

Using the data from Fig. 6.2-2, the estimated mean, variance, coefficient of skewness, and coefficient of kurtosis were calculated to be

$$\hat{m}_H = 9.177 \times 10 \text{ Volts}^{-1}$$

$$(\hat{\sigma}_H)^2 = \hat{\mu}_{H2} = 1.230 \times 10^3 \text{ Volts}^{-2} \quad (6.2\text{-}15)$$

$$\hat{\alpha}_{H3} = 0.048$$

$$\hat{\alpha}_{H4} = 2.217.$$

The selected candidates are listed below along with their coefficients of skewness and kurtosis:

a) Uniform, $\alpha_3 = 0$, $\alpha_4 = 1.8$

b) Triangular, $\alpha_3 = 0$, $\alpha_4 = 2.4$

c) Weibull ($\beta = 3$), $\alpha_3 = 0.16$, $\alpha_4 = 2.73$.

Application of the χ^2 test resulted in acceptance of all three distributions. Inserting the sample mean and variance from Eqs.(6.2-15), the analytical expressions for the three distributions are given by:

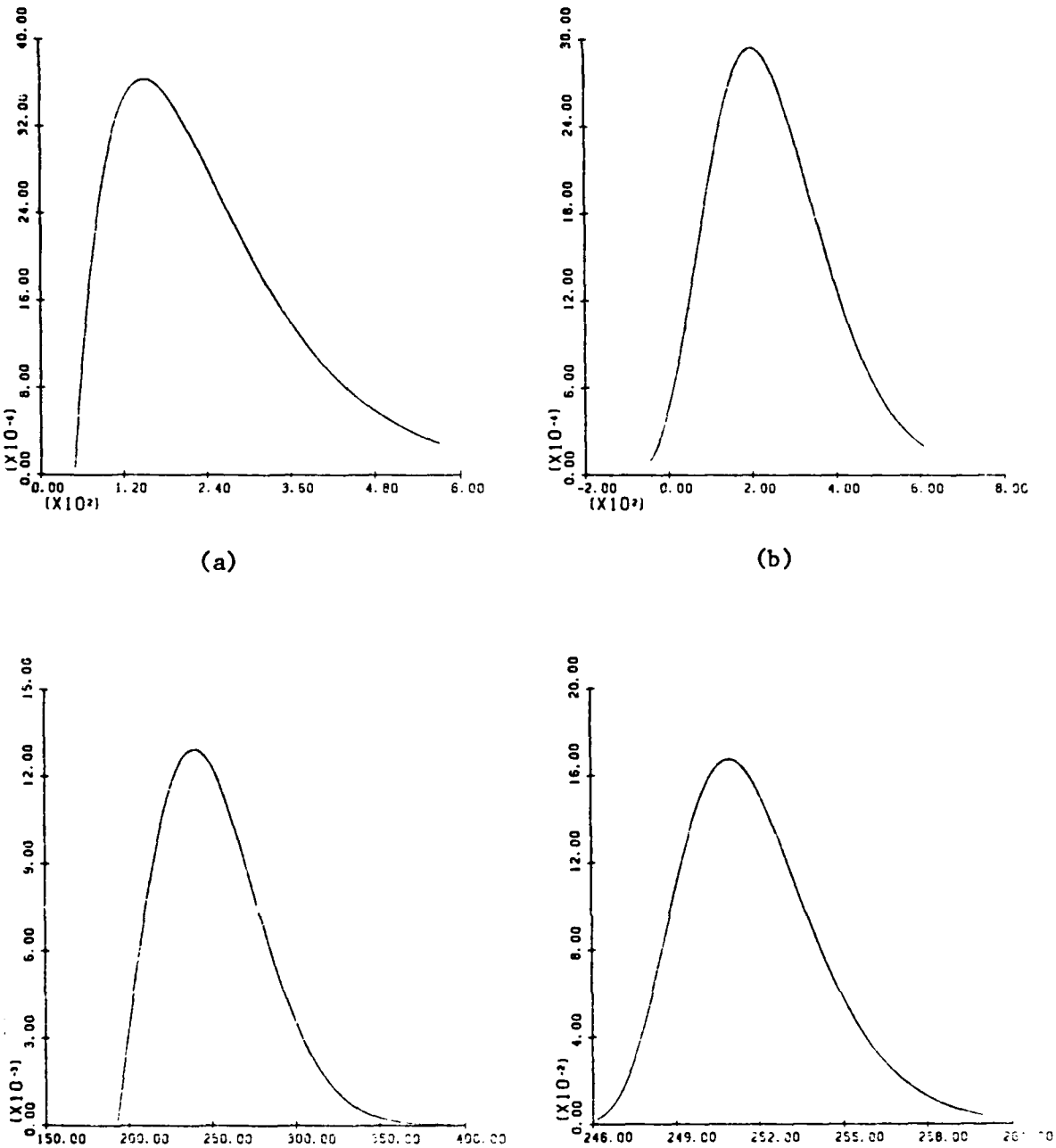

Fig. 6.2-3. Approximations to $f_H(h)$ at 4 MHz. (a) Gamma (a = 1), (b) Gamma (a = 7), (c) Weibull (β = 2), (d) Log Normal (c = 1/4)

Uniform

$$f_H(h) \simeq \begin{cases} 8.2 \times 10^{-3}, & 31.0 \leq h \leq 152.5 \\ 0, & \text{elsewhere} \end{cases} \qquad (6.2\text{-}16)$$

Triangular

$$f_H(h) \cong \begin{cases} (1.36 \times 10^{-4})(h - 5.86), & 5.86 < h \leq 91.8 \\ (1.36 \times 10^{-4})(177.7 - h), & 91.8 < h < 177.7 \\ 0, & \text{elsewhere} \end{cases} \qquad (6.2\text{-}17)$$

Weibull ($\beta = 3$)

$$f_H(h) \cong \begin{cases} (2.039 \times 10^{-3})(h-81.6)^2 \exp\{-(6.8\times10^{-4})(h-81.6)^3\}, & h \geq 81.6 \\ 0 & h < 81.6 \end{cases} \qquad (6.2\text{-}18)$$

The three density functions are plotted in Figs. 6.2-4(a), (b), and (c), repectively.

6.3 Analysis of Data Related to Lighting the LED

The LED was observed to light when the peak voltage of the 1kHz tone at V_3 was approximately equal to 1.5V. With f_c = 4MHz, it was always possible to light the LED. For convenience, the value of the threshold at V_3 was set at

$$A_{3T} = \sqrt{2} = 1.414 \text{ Volts. (4 MHz)} \qquad (6.3\text{-}1)$$

The rms reading at V_3 was then equal to one volt which was a convenient level at which to set the threshold.

At 15 MHz, however, it was not always possible to light the LED. In order to maximize the number of available data points, the value of the

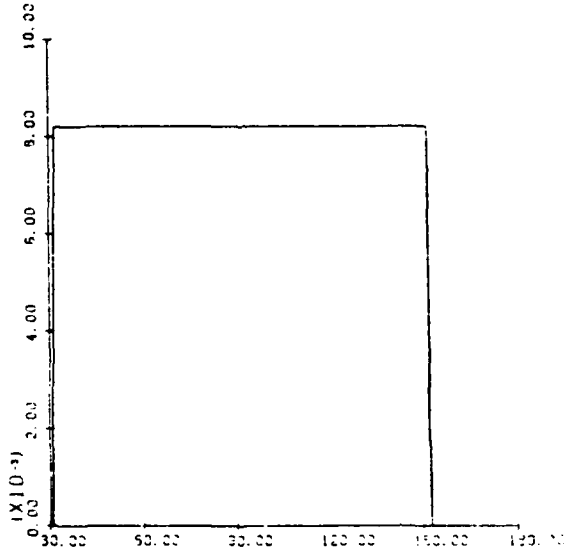

(a)

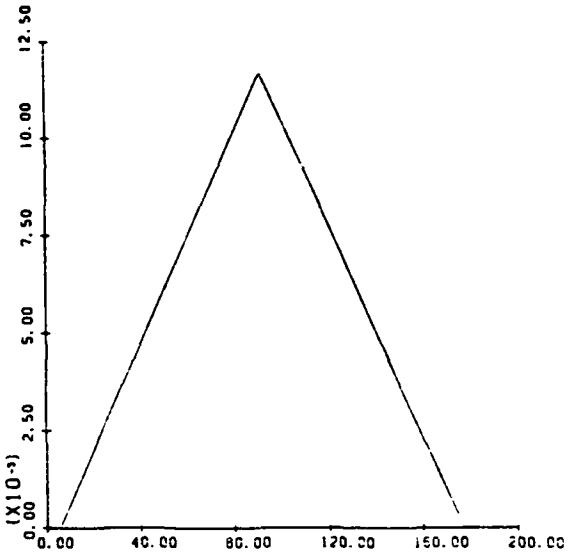

(b)

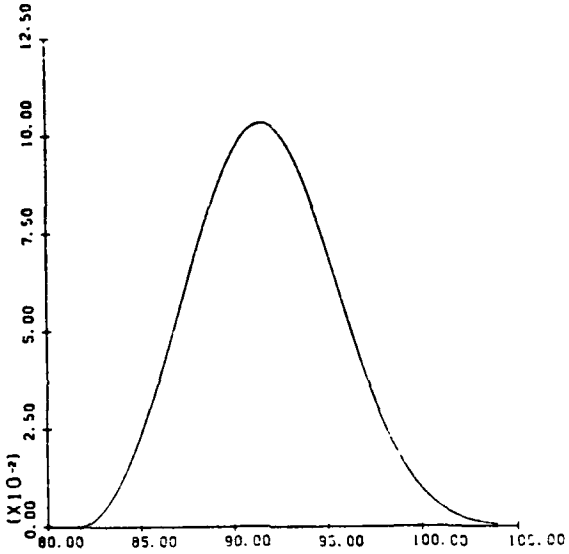

(c)

Fig. 6.2-4. Approximations to $f_H(h)$ at 15 MHz, (a) Uniform, (b) Triangular, (c) Weibull ($\beta = 3$).

threshold at V_3 was set at

$$A_{3T} = 0.2\sqrt{2} = 0.283 \text{ Volts. (15 MHz)} \qquad (6.3\text{-}2)$$

The rms reading at V_3 was then equal to 0.2 Volt which was also a convenient level at which to set the threshold.

The amplitude of the carrier at V_1 which produced the threshold voltage at V_3 was denoted by the random variable, A_{1T}. The data obtained at 4 MHz and 15 MHz are tabulated in ascending order in Figs. 6.3-1 and 6.3-2, respectively. The experiment involving lighting of the LED was carried out at the University of Kentucky while the experiment involving measurement of the second-order nonlinear transfer function was performed at SUNY, Buffalo. The printed circuit boards at both locations were designed to be "identical." To verify whether this was the case, several measurements were repeated at SUNY, Buffalo using several of the operational amplifiers employed at the University of Kentucky. At 4MHz, the readings at SUNY, Buffalo were approximately a factor of 1.46 smaller than those at Kentucky. At 15 MHz, the readings at SUNY, Buffalo were approximately a factor of 1.2 smaller than those at Kentucky. Because the second-order nonlinear transfer functions were measured at SUNY, Buffalo, it was decided to reduce the data in Fig. 6.3-1 by a factor of 1.46 and the data in Fig. 6.3-2 by a factor of 1.2.

The probability density function associated with A_{1T} was denoted by $f_{A_{IT}}(a_{1T})$. The procedure used to obtain approximations to $f_{A_{IT}}(a_{1T})$ was identical to that followed for $f_G(g)$ and $f_H(h)$. As before, the χ^2 statistic was evaluated using the relation.

$$\chi^2 = N_{A_{1T}} \sum_{k=1}^{5} \frac{(\hat{p}_k - 0.2)^2}{0.2} \qquad (6.3\text{-}3)$$

A_{1T} (Volts, peak)	Corrected Data $A_{1T}/1.46$	A_{3T} (Volts, rms)
1.35	0.92	1
1.48	1.01	1
1.50	1.03	1
1.61	1.10	1
1.73	1.18	1
1.82	1.25	1
1.94	1.33	1
2.11	1.45	1
2.16	1.48	1
2.22	1.52	1
2.31	1.58	1
2.32	1.59	1
2.32	1.59	1
2.42	1.66	1
2.56	1.75	1
2.60	1.78	1
2.80	1.92	1
3.22	2.21	1
3.28	2.25	1
3.42	2.34	1
3.76	2.58	1
3.78	2.59	1
3.89	2.66	1
4.19	2.87	1
4.53	3.10	1
5.52	3.78	1

Fig. 6.3-1. Measurement of A_{1T} at 4MHz

A_{1T} (Volts, peak)	Corrected Data $A_{1T}/1.2$	A_{3T} (Volts, Tms)
0.24	0.20	0.2
0.40	0.33	0.2
0.59	0.49	0.2
0.60	0.5	0.2
0.64	0.53	0.2
0.64	0.53	0.2
0.69	0.58	0.2
0.74	0.62	0.2
0.92	0.77	0.2
0.93	0.78	0.2
1.17	0.98	0.2
1.23	1.03	0.2
1.40	1.17	0.2
1.50	1.25	0.2
1.58	1.32	0.2
1.68	1.40	0.2
1.75	1.46	0.2
1.90	1.58	0.2
2.16	1.80	0.2
2.18	1.82	0.2
2.62	2.18	0.2
2.63	2.19	0.2
3.08	2.57	0.2
3.20	2.67	0.2
4.10	3.42	0.2
6.07	5.06	0.2

Fig. 6.3-2. Measurements of A_{1T} at 15 MHz.

where $N_{A_{1T}}$ denotes the number of measurements for A_{1T}. For the data of Fig. 6.3-1 and 6.3-2

$$N_{A_{1T}} = 26. \tag{6.3-4}$$

Once again, the numerical value obtained for the χ^2 statistic was compared to a threshold value tabulated for a significant level given by

$$\beta_o = 0.01 \tag{6.3-5}$$

and the distribution under test. The cases for f_c = 4MHz and f_c = 15 MHz are discussed separately.

Case 1: f_c = 4 MHz

Using the data from Fig. 6.3-1 divided by the factor of 1.46, the estimated mean, variance, coefficient of skewness, and coefficient of kurtosis were calculated to be

$$\begin{aligned} \hat{m}_A &= 1.866 \text{ Volts} \\ (\sigma_A)^2 = \hat{\mu}_{A2} &= 0.524 \text{ (Volts)}^2 \\ \hat{\alpha}_{A3} &= 0.899 \\ \hat{\alpha}_{A4} &= 3.089. \end{aligned} \tag{6.3-6}$$

The selected candidates for approximating $f_{A_{1T}}(a_{1T})$ are listed below along with their coefficients of skewness and kurtosis:

a) Log Normal (c = 1/4), $\alpha_3 = 0.778$, $\alpha_4 = 4.096$

b) Weibull ($\beta = 2$), $\alpha_3 = 0.63$, $\alpha_4 = 3.24$

c) Gamma (a = 4), $\alpha_3 = 0.89$, $\alpha_4 = 4.2$.

Application of the χ^2 test resulted in acceptance of all three distributions. Inserting the sample mean and variance from Eqs.(6.3-6), the analytical expressions for the three distributions are given by:

Log Normal (C = 1/4)

$$f_{A_{1T}}(a_{1T}) \cong \begin{cases} 1.596\ (a_{1T} + 3.5)^{-1} \exp\{-8[\ln((.192)\ (a_{1T} + 3.5))]^2\}, & a_{1T} \geq -3.5 \\ 0, & a_{1T} < -3.5 \end{cases} \tag{6.3-7}$$

Weibull (β = 2)

$$f_{A_{1T}}(a_{1T}) \cong \begin{cases} 17.78\ (a_{1T}-1.6)\exp\{-8.889\ (a_{1T}-1.6)^2\}, & a_T \geq 1.6 \\ 0, & a_{1T} < 1.6 \end{cases} \tag{6.3-8}$$

Gamma (a = 4)

$$f_{A_{1T}}(a_{1T}) \cong \begin{cases} 11.71\ (a_{1T} - .25)^4 \exp\{-3.088\ (a_{1T} - .25)\}, & a_{1T} \geq .25 \\ 0, & a_{1T} < .25 \end{cases} \tag{6.3-9}$$

The three density functions are plotted in Figs. 6.3-3 (a), (b), and (c), respectively.

Case 2: f_c = 15 MHz

Using the data from Fig. 6.3-2 divided by the factor of 1.2, the estimated mean, variance, coefficient of skewness, and coefficient of kurtosis were calculated to be

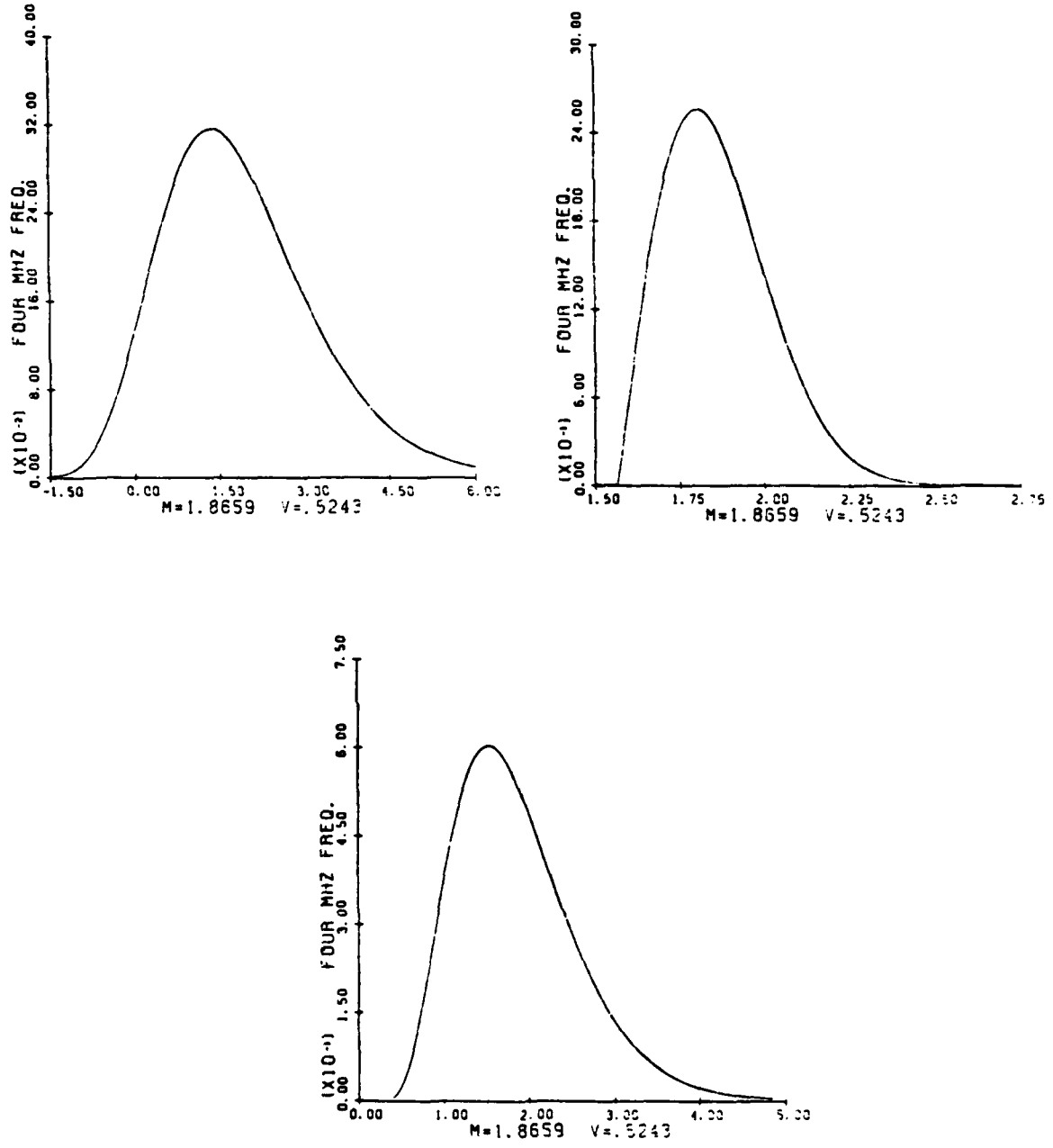

Fig. 6.3-3. Approximations to $f_{A_{1T}}(a_{1T})$ at 4 MHz (corrected data)
(a) Log Normal (c = 1/4), (b) Weibull (β = 2),
(c) Gamma (a = 4).

$$\hat{m}_A = 1.432 \text{ Volts}$$

$$(\hat{\sigma}_A)^2 = \hat{\mu}_{A2} = 1.21 \text{ (Volts)}^2 \qquad (6.3\text{-}10)$$

$$\hat{\alpha}_{A3} = 1.681$$

$$\hat{\alpha}_{A4} = 5.931$$

The selected candidates for approximating $f_{A_{1T}}(a_{1T})$ are listed below along with their coefficients of skewness and kurtosis:

a) Log Normal ($c = 1/2$), $\alpha_3 = 1.75$, $\alpha_4 = 8.898$

b) Weibull ($\beta = 1$), $\alpha_3 = 2$, $\alpha_4 = 9$

c) Gamma ($a = 1$), $\alpha_3 = 1.41$, $\alpha_4 = 6.$

Application of the χ^2 test resulted in acceptance of all three distributions. Inserting the sample mean and variance from Eqs. (6.3-10), the analytical expressions for the three distributions are given by:

Log Normal ($c = 1/2$)

$$f_{A_{1T}}(a_{1T}) \cong \begin{cases} .798\ (a_{1T} + 1.1)^{-1} \exp\{-2[\ell n((.549)(a_{1T}+1.1))]^2\}, & a_{1T} \geq -1.1 \\ 0, & a_{1T} < -1.1 \end{cases} \qquad (6.3\text{-}11)$$

Weibull ($\beta = 1$)

$$f_{A_{1T}} \begin{cases} .909 \exp\{-(.909)(a_{1T} - .33)\}, & a_{1T} \geq .33 \\ 0, & a_{1T} < .33 \end{cases} \qquad (6.3\text{-}12)$$

Gamma (a = 1)

$$f_{A_{1T}}(a_{1T}) \cong \begin{cases} 1.15(a_{1T} + .12)\exp\{-(1.071)(a_{1T} + .12)\}, & a_{1T} \geq -.12 \\ 0, & a_{1T} < -.12 \end{cases} \quad (6.3\text{-}13)$$

The three density functions are plotted in Figs. 6.3-4 (a), (b), and (c), respectively.

Figs. 6.3-3 and 6.3-4 illustrate approximations to $f_{A_{1T}}(a_{1T})$ which were obtained directly from the experimental data. Eq.(2.4-11) was also used to predict the form of $f_{A_{1T}}(a_{1T})$ based upon approximations to $f_G(g)$ and $f_H(h)$. The cases for f_c = 4MHz and f_c = 15 MHz are discussed separately.

Case 1: f_c = 4 MHz

At 4 MHz two approximations were obtained for $f_G(g)$ while four approximations were found for $f_H(h)$. The eight possible combinations are listed below:

Combination	$f_G(g)$	$f_H(h)$
1	Log Normal (c = 1/4)	Gamma (a = 1)
2	Log Normal (c = 1/4)	Gamma (a = 7)
3	Log Normal (c = 1/4)	Weibull (β = 2)
4	Log Normal (c = 1/4)	Log Normal (c = 1/4)
5	Gamma (a = 7)	Gamma (a = 1)
6	Gamma (a = 7)	Gamma (a = 7)
7	Gamma (a = 7)	Weibull (β = 2)
8	Gamma (a = 7)	Log Normal (c = 1/4)

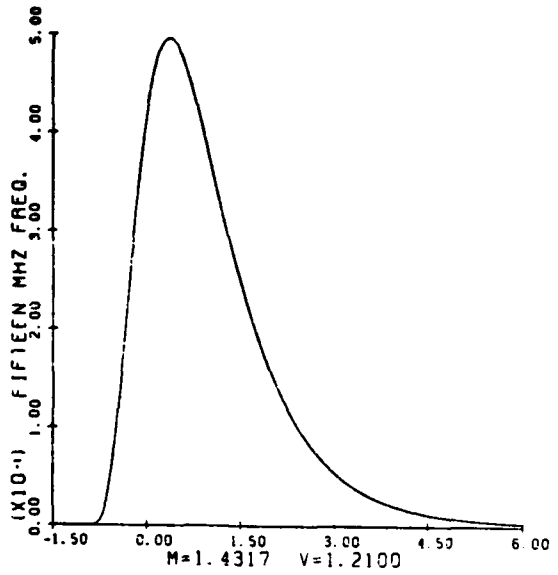

(a)

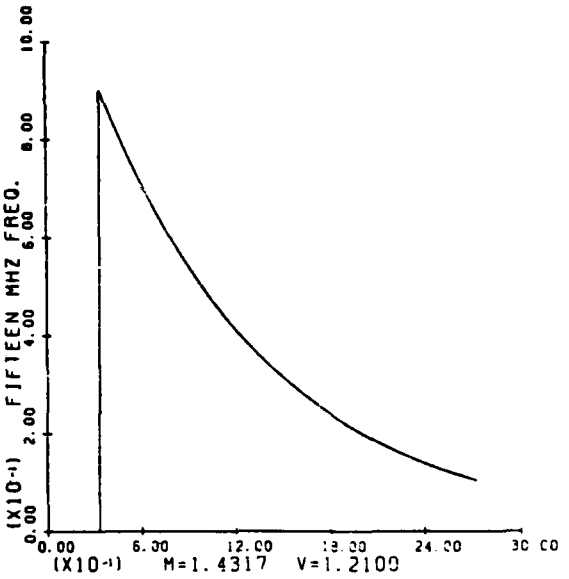

(b)

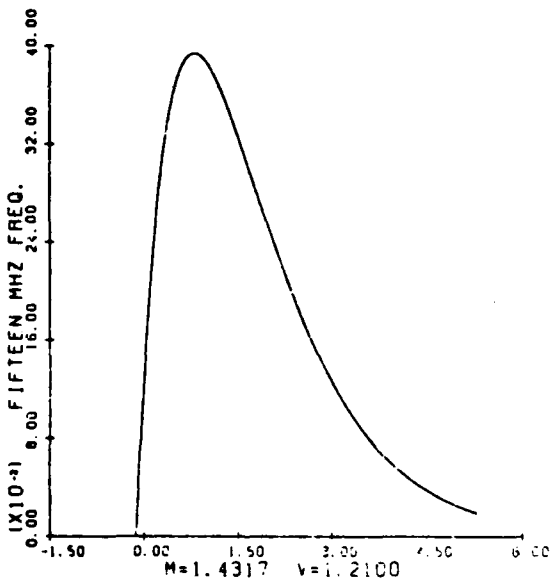

(c)

Fig. 6.3-4. Approximations to $f_{A_{1T}}(a_{1T})$ at 15 MHz (corrected data).
(a) Log Normal (c = 1/2), (b) Weibull (β = 1),
(c) Gamma (a = 1)

Each of these combinations was used in Eq. (2.4-11) to predict approximations to $f_{A_{1T}}(a_{1T})$. The integral was evaluated numerically and the results are plotted in Figs. 6.3-5 and 6.3-6. The sharp peaks resulted because the step size used in the integration was chosen to be too large.

A χ^2 test was then applied to each of the eight approximations for $f_{A_{1T}}(a_{1T})$ to determine whether the corrected data from Fig. 6.3-1 and the approximations in Figs. 6.3-5 and 6.3-6 were statistically consistent. In every case the a_{1T} - axis was subdivided into 5 cells such that the area under the approximation for each cell was approximately equal to 0.2.

Let the area for the $k^{\underline{th}}$ cell be denoted by p_k. Also, let n_k denote the number of corrected data which fell into the $k^{\underline{th}}$ cell. Since there are 26 data points, the relative frequency of occurrence for the $k^{\underline{th}}$ cell was defined to be

$$\hat{p}_k = \frac{n_k}{26} \quad ; \; k = 1, 2, \ldots, 5. \tag{6.3-14}$$

The χ^2 statistic was then evaluated using the relation

$$\chi^2 = 26 \sum_{k=1}^{5} \frac{(\hat{p}_k - p_k)^2}{p_k}. \tag{6.3-15}$$

As was done earlier, the numerical value obtained for the χ^2 statistic was compared to a threshold value tabulated for a significance level given by $\beta_o = 0.01$.

Application of the χ^2 test resulted in all eight approximations being accepted.

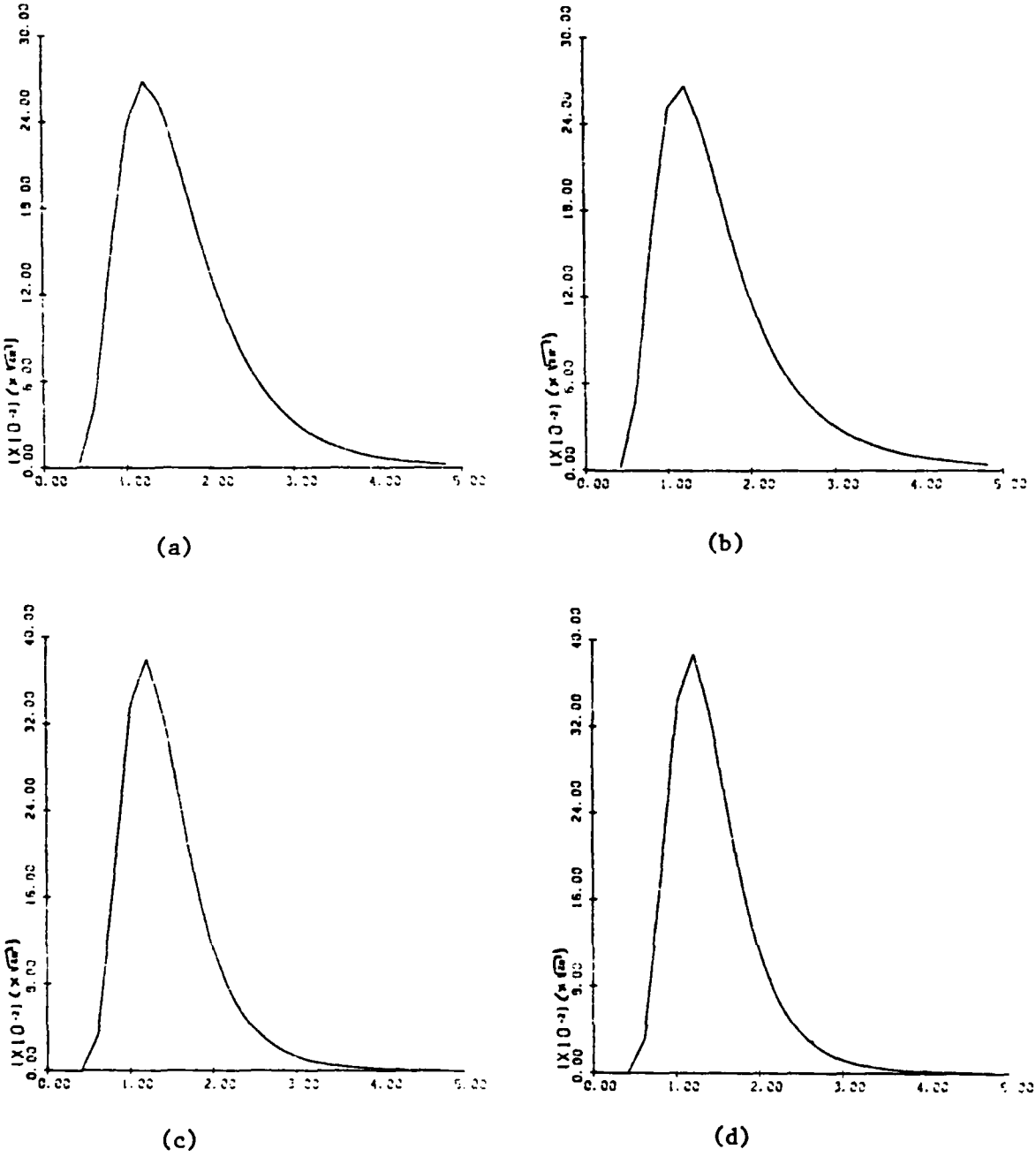

Fig. 6.3-5. Approximations to $f_{A_{1T}}(a_{1T})$ at 4 MHz obtained by evaluating Eq. (2.4-11) with $f_G(g)$ approximated by Log Normal (c = 1/4) and $f_H(h)$ approximated by (a) Gamma (a = 1), (b) Gamma (a = 7), (c) Weibull (β = 2), (d) Log Normal (c = 1/4).

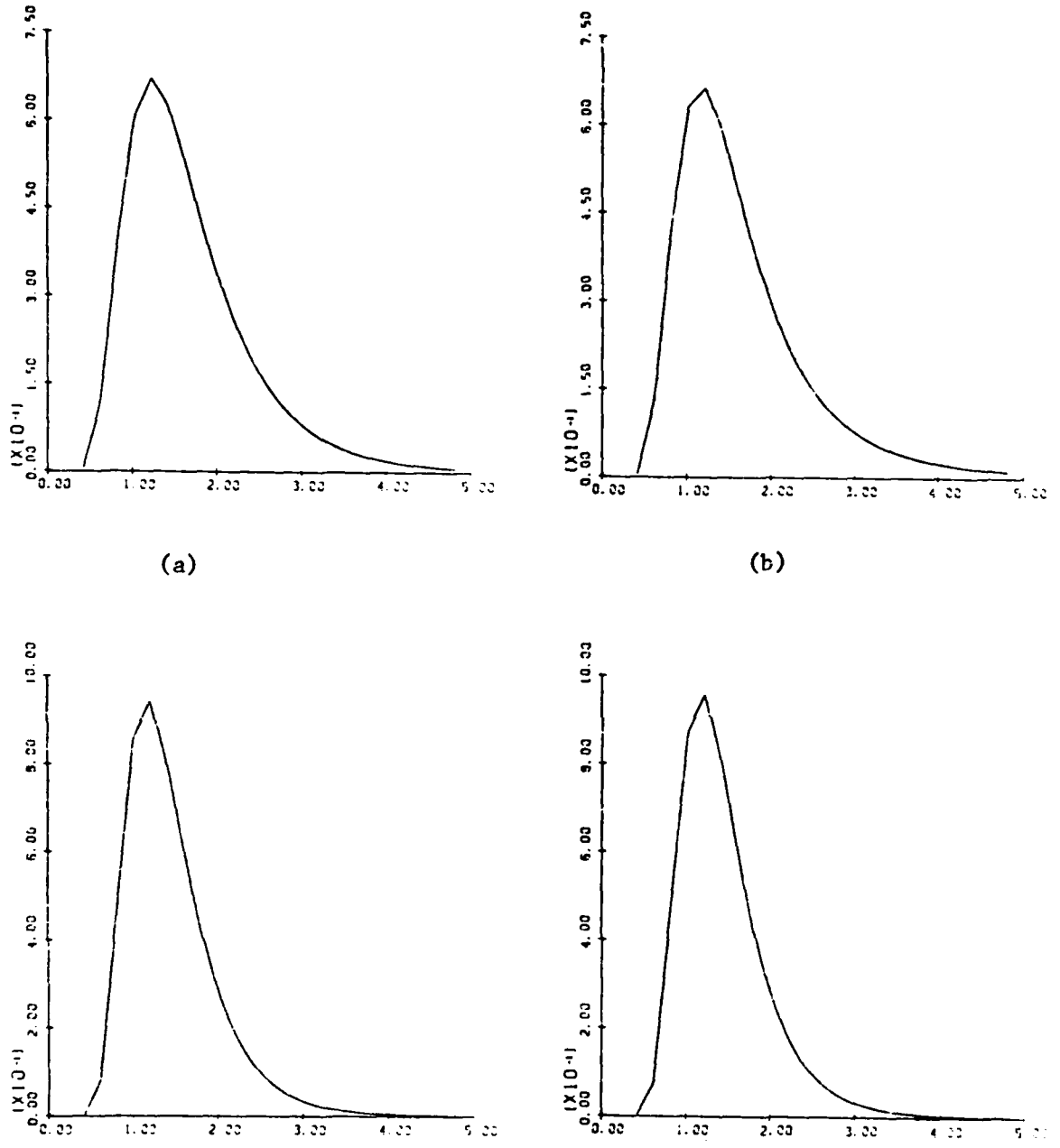

Fig. 6.3-6. Approximations to $f_{A_{1T}}(a_{1T})$ at 4 MHz obtained by evaluating Eq. (2.4-11) with $f_G(g)$ approximated by Gamma (a = 7) and $f_H(h)$ approximated by (a) Gamma (a = 1), (b) Gamma (a = 7), (c) Weibull (β= 2), (d) Log Normal (c = 1/4)

Case 2: f_c = 15 MHz

At 15 MHz two approximations were obtained for $f_G(g)$ while three approximations were found for $f_H(h)$. The six possible combinations are listed below:

Combination	$f_G(g)$	$f_H(h)$
1	Gamma (a = 3)	Uniform
2	Gamma (a = 3)	Triangular
3	Gamma (a = 3)	Weibull (β = 3)
4	Gamma (a = 4)	Uniform
5	Gamma (a = 4)	Triangular
6	Gamma (a = 4)	Weibull (β = 3)

Each of these combinations was used in Eq. (2.4-11) to predict approximations to $f_{A_{1T}}(a_{1T})$. The integral was evaluated numerically and the results are plotted in Figs. 6.3-7 and 6.3-8. As before, sharp peaks resulted because the step size chosen for the integration was too large.

A χ^2 test was then applied to each of the six approximations for $f_{A_{1T}}(a_{1T})$ to determine whether the corrected data from Fig. 6.3-2 and the approximations in Figs. 6.3-7 and 6.3-8 were statistically consistent. The a_{1T}-axis was again subdivided into 5 cells for every case such that the area under the approximation for each cell was approximately equal to 0.2. The χ^2 statistic was evaluated using Eq.(6.3-15).

For a significance level given by β_c = 0.01, the χ^2 test resulted in all six approximations being accepted.

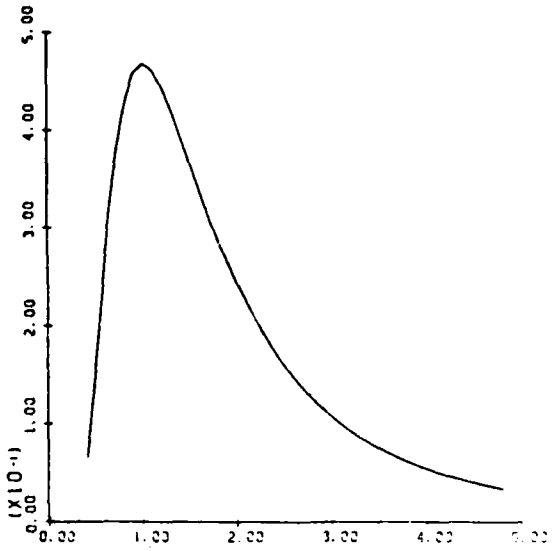

(a)

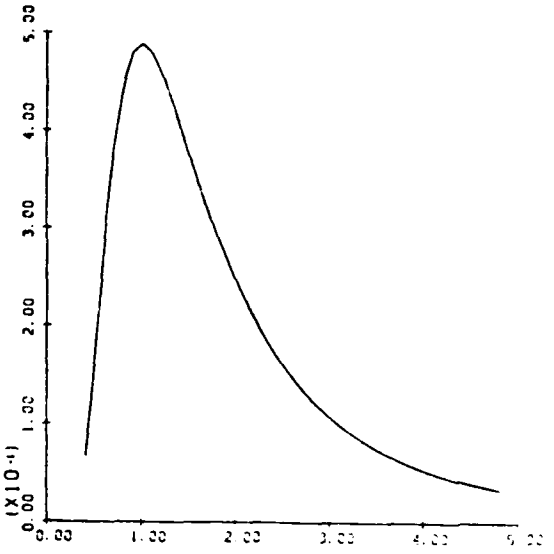

(b)

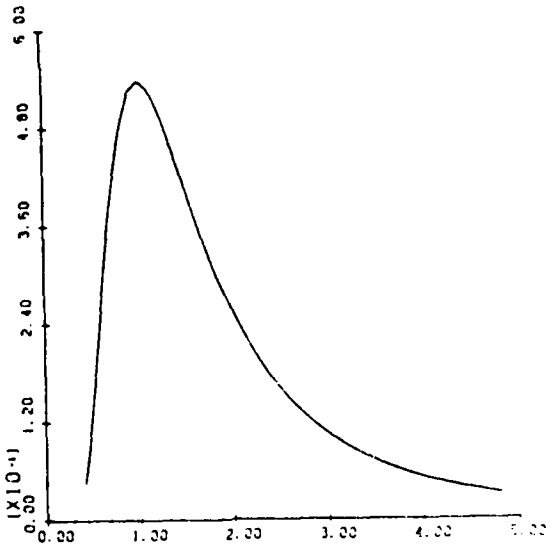

(c)

Fig. 6.3-7. Approximations to $f_{A_{1T}}(a_{1T})$ at 15 MHz obtained evaluating Eq. (2.4-11) with $f_G(g)$ approximated by Gamma (a=3) and $f_H(h)$ approximated by (a) Uniform, (b) Triangular, (c) Weibull (β= 3).

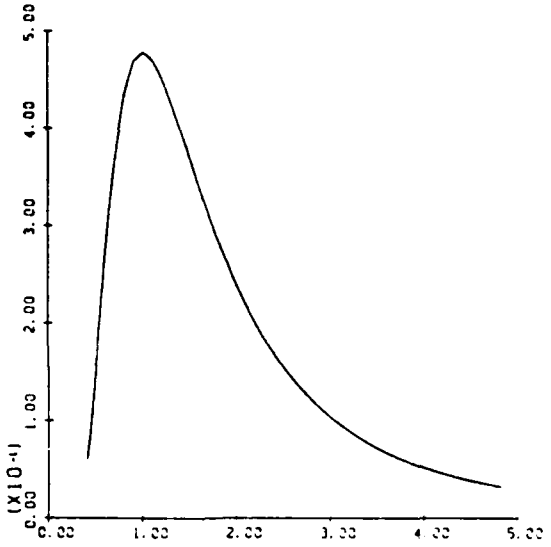

(a)

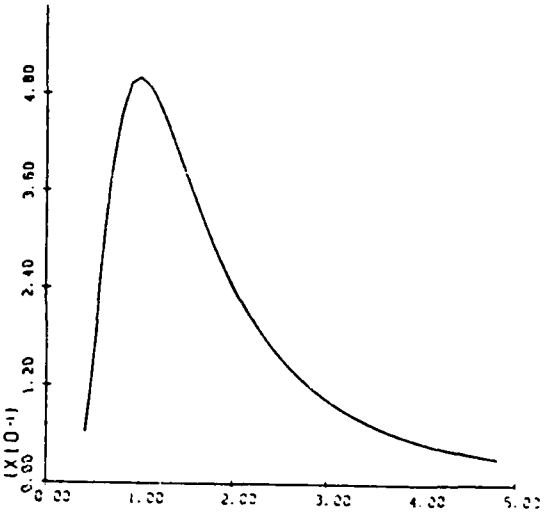

(b)

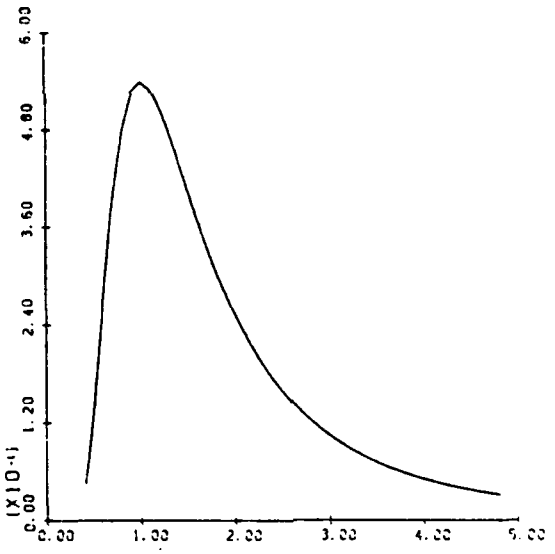

(c)

Fig. 6.3-8. Approximations to $f_{A_{1T}}(a_{1T})$ at 15 MHz obtained by evaluating Eq. (2.4-11) with $f_G(g)$ approximated by Gamma (a=4) and $f_H(h)$ approximated by (a) Uniform, (b)Triangular, (c) Weibull (β = 3).

VII. Conclusions

The LED experiment served to demonstrate the following results:

1) Crosstalk in random cable bundles can lead to serious degradation of system performance.

2) Weak nonlinearities which exist in the amplification region of operational amplifiers are capable of generating significant in-band interference by demodulating out-of-band amplitude modulated signals.

3) The linear transfer function which characterizes crosstalk in random cable bundles, the second-order nonlinear transfer function which characterizes the weak nonlinearities in the amplification region of operational amplifiers, and the susceptibility level of the three-stage amplifier all display random behavior.

4) Well-known probability density functions can be used to approximate the crosstalk linear transfer function, the second-order nonlinear transfer function of operational amplifiers, and the susceptibility level of the three-stage amplifier.

5) Given probability density functions for the crosstalk linear transfer function and the second-order nonlinear transfer function of operational amplifiers, it is possible to predict the probability density function for the susceptibility level of the three-stage amplifier.

6) The predicted probability density function for the susceptibility level of the three-stage amplifier can be approximated by well-known probability density functions that are statistically consistent with experimental data. Although not included in this report, these approximations are useful for determining the probability of EMI and/or compatibility.

VIII. References

1. Chen, G. and Whalen, J., "Basic EMC Technology Advancement for C^3 Systems," Volume IA, RADC-TR-82-286, December 1983, AD-A141369.

2. Sutu, Y. and Whalen, J., "Basic EMC Technology Advancement for C^3 Systems," Volume IB, RADC-TR-82-286, December 1984.

3. Bowers, J., "Basic EMC Technology Advancement for C^3 Systems," Volume IIA, RADC-TR-82-286, April 1983, AD-A133661.

4. Bowers, J. and Vogelsong, R., "Basic EMC Technology Advancement for C^3 Systems, "Volume II B, RADC-TR-82-286, April 1984, AD-A146333.

5. Ephrath, A. and Weiner, D., "Basic EMC Technology Advancement for C^3 Systems, "Volume III A, RADC-TR-82-286, August 1984.

6. Chair, Z., Dave, T., Ouibrahim, H. and Weiner D., "Basic EMC Technology Advancement for C^3 Systems," Volume III B, RADC-TR-82-286, December 1984.

7. Abraham, R. and Paul, C., "Basic EMC Technology Advancement for C^3 Systems," Volume IV A, RADC-TR-82-286, November 1982, AD-A124861.

8. Paul, C., "Basic EMC Technology Advancement for C^3 Systems," Volume IV B, RADC-TR-82-286, November 1982, AD-A124 862.

9. Jolly, M. and Paul, C., "Basic EMC Technology Advancement for C^3 Systems," Volume IVC, RADC-TR-82-286, November 1982, AD-A124863.

10. Koopman, D. and Paul, C., "Basic EMC Technology Advancement for C^3 Systems," Volume IV D, RADC-TR-82-286, August 1984.

11. Everett, W., and Paul, C., "Basic EMC Technology Advancement for C^3 Systems," Volume IV E, RADC-TR-82-286, August 1984.

11a. Beech, W. and Paul, C., "Basic EMC Technology Advancement for C^3 Systems," Volume IV F, RADC-TR-82-286, December 1984.

12. Paul, C., "Basic EMC Technology Advancement for C^3 Systems," Volume V, RADC-TR-82-286, October 1984.

13. Paul, C., Weiner, D., and Whalen, J., "Basic EMC Technology Advancement for C^3 Systems, Volume VI, RADC-TR-82-286, December 1984.

14. Capraro, G., "The Intrasystem EMC Problem and Future Directions," Proceedings of the 4th Symposium and Technical Exhibition on EMC, Zurich, March 10-12, 1981.

15. Bossart, R., Shekleton, J., and Lessard, B., "EMC in Microelectronics: A Methodology," Proceedings of the 1981 IEEE International Symposium on EMC, Boulder, Colorado, August 18-20, 1981, pp. 79-84.

16. Ephrath, A. and Weiner, D., "EMC Modeling and Analysis - A Probabilisitic Approach," RADC-TR-83-102, April, 1983.

VIII References (Continued)

17. Weiner, D. and Spina, J., Sinusoidal Analysis and Modeling of Weakly Nonlinear Circuits, New York, Van Nostrand Reinhold Company, 1980.

18. Papoulis, A., Probability, Random Variables, and Stochastic Processes, New York, McGraw-Hill Book Company, 1965.

19. Paul, C., "Applications of Multiconductor Transmission Line Theory to the Prediction of Cable Coupling," Volumes I-VIII, RADC-TR-76-101, April 1976 - August 1980.

20. Capraro, G. and Paul, C., "A Probabilistic Approach to Wire Coupling Interference Prediction," Proceedings of the 1981 IEEE International Symposium on EMC, Zurich March 10-12, 1981.

21. Bogdanor, J. et. al., "Intrasystem Electromagnetic Compatibility Analysis Program," Volumes I-III, RADC-TR-74-342, December 1974.

22. Fang, T. and Whalen, J., "Nonlinear System Analysis in Bipolar Integrated Circuits," RADC-TR-79-245, January 1980.

23. Goldblood, J., Riemens, K., and Stienstra, A., "Increasing the RFI Immunity of Amplifiers with Negative Feedback," Proceedings of the 5th Symposium and Technical Exhibition on EMC, pp. 471-476, Zurich, March 8-10, 1983.

MISSION
of
Rome Air Development Center

RADC plans and executes research, development, test and selected acquisition programs in support of Command, Control Communications and Intelligence (C^3I) activities. Technical and engineering support within areas of technical competence is provided to ESD Program Offices (POs) and other ESD elements. The principal technical mission areas are communications, electromagnetic guidance and control, surveillance of ground and aerospace objects, intelligence data collection and handling, information system technology, ionospheric propagation, solid state sciences, microwave physics and electronic reliability, maintainability and compatibility.

END

FILMED

9-85

DTIC